Title

Linear Stability of a Wake Vortex and its Transient Growth: Numerical Analysis in Light of Critical-Layer Eigenmodes and Spectra

Author

Lee, Sangjoon

Publication Date

2024

Linear Stability of a Wake Vortex and its Transient Growth: Numerical Analysis in Light of Critical-Layer Eigenmodes and Spectra

by

Sangjoon Lee

A dissertation submitted in partial satisfaction of the

requirements for the degree of

Doctor of Philosophy

in

Engineering - Mechanical Engineering

and the Designated Emphasis

in

Computational and Data Science and Engineering

in the

Graduate Division

of the

University of California, Berkeley

Committee in charge:

Professor Philip S. Marcus, Chair
Professor Ömer Savaş
Professor Jon A. Wilkening
Associate Professor Simo A. Mäkiharju

Summer 2024

Linear Stability of a Wake Vortex and its Transient Growth: Numerical Analysis in Light of Critical-Layer Eigenmodes and Spectra

Abstract

Linear Stability of a Wake Vortex and its Transient Growth: Numerical Analysis in Light of Critical-Layer Eigenmodes and Spectra

by

Sangjoon Lee

Doctor of Philosophy in Engineering - Mechanical Engineering

and the Designated Emphasis in

Computational and Data Science and Engineering

University of California, Berkeley

Professor Philip S. Marcus, Chair

The early-time growth of an individual vortex in a wake vortex pair is explored, focusing on its linear stability and transient growth, which are meaningful for understanding the lifespan of vortices and mitigating hazards from wake turbulence. This study synthesises two parts: linear stability analysis and transient growth analysis. The linear stability of wake vortices is examined in both inviscid and viscous contexts, using the Batchelor or Lamb-Oseen vortex as a base vortex model. Linear stability analysis determines the growth rates of infinitesimal perturbations in the vortex flow by linearising the incompressible Navier-Stokes or Euler equations around the base vortex, leading to an eigenvalue problem that discloses the vortex's stability properties. Inviscid analysis, with zero viscosity, successfully reveals a continuous spectrum associated with critical-layer singularities, causing discontinuity in perturbation velocity in the inviscid limit and requiring careful numerical parameter tuning to avoid under-resolved, or so-called spurious, solutions. Non-zero viscosity alters both the discrete and continuous spectra, necessitating numerical resolution conforming to the Reynolds number to the one-third power scaling law to resolve the newly discovered viscous critical-layer eigenmode family. The transient growth phenomenon is then explored through non-modal analysis to understand how initial perturbations, as combinations of numerous eigenmodes, can experience significant transient growth even in linearly stable vortices. The transient growth formalism is applied to the linearised Navier-Stokes equations. Optimal perturbations that maximise energy amplification over finite time intervals are found, to which the viscous critical-layer eigenmode family serves as the main contributor. Numerical simulations quantify the growth of perturbations considering nonlinearity, showing that while nonlinearity may slightly alter transient dynamics, overall trends align with formalism predictions. Lastly, motivated by contrails around wake vortices, the research investigates particle-initiated transient growth, where perturbations evolve through particle-vortex interactions. Two-way coupled particle-vortex simulations demonstrate continual perturbation development, presenting primary growth patterns as captured in the transient growth formalism. This investigation implies the practicability of the transient growth phenomenon.

To my family, who give me unconditional support and love

Contents

List of Figures

List of Tables

Acknowledgements

Like many other doctoral students, my journey to a doctorate has been fraught with numerous challenges, frustrations due to failures, and difficult decisions with hardly predictable consequences. Just seven months after I joined Berkeley, the campus, along with much of the world, nearly shut down due to the global coronavirus pandemic, whose aftermath lasted almost three years. Working from home became the new norm, and online communication via headset, webcam, and monitor largely replaced face-to-face meetings. Unfortunately, I was not someone who could easily adapt to these new trends, which slowed my research progress and from time to time led to feelings of anxiety and diffidence. Up until finishing this dissertation, there was a continual *miracle* that enabled me to overcome difficulties and eagerly push my research forward. The completion of this dissertation would not have been feasible without this miracle – that is, the firm support of my advisor, degree committee members, lab colleagues, friends, family, and everyone else who inspired me along the way, as well as the graduate research support fellowships from the Ilju Academy and Culture Foundation and UC Berkeley. I owe my accomplishment to all of them.

Particularly, first and foremost, I express my earnest gratitude to Dr. Philip S. Marcus, my research advisor, degree committee chair, and esteemed teacher, for consistently providing clear and insightful advice throughout my graduate years. Without his advising, I would not even have found the longevity of vortices intriguing and thus would not have been able to develop this research to its current stage. I have learned a lot from his passion and confidence towards research, which I will bear in mind in the pursuit of new discoveries.

Furthermore, I extend my warm thanks to all the other members of my degree committee, Dr. Ömer Savaş, Dr. Jon A. Wilkening, and Dr. Simo A. Mäkiharju, for investing substantial time in guiding me through coursework, a qualifying exam, and several meetings. The knowledge and lessons they shared with me have formed a strong foundation for my graduate research.

I would like to give immense credit to all my colleagues who studied and worked with me at the UC Berkeley CFD laboratory: Dr. Chiyu “Max” Jiang, Dr. Haris M. Sheikh, Aidi Zhang, Jinge Wang, Haley Y. Wohlever, and Sungkyu Kim. Max, despite our short overlap, showed me the ideal figure of a superb graduate student. Haris, who explored the crossing of fluid dynamics and machine-learning optimisation, kept me motivated with his novel ideas that I might not have thought of. Aidi has been the symbol of diligence in the lab; his unwavering focus on the longevity of Jupiter’s Great Red Spot always amazed me and I bet he will soon make more of his studies appear in world-class research journals. Jinge has indisputably been my perfect research collaborator; I have no doubt that his ongoing wake vortex instability study will end up being a great piece of work paired with my current research. Haley, who joined the lab almost at the same time, has been an inspirational student and researcher and I will never forget her warmhearted encouragement brought to me and others. Sungkyu, who joined most recently, has already become a close friend of mine thanks to his mindful and kind personality; I see his ardent passion that will undoubtedly lead to great accomplishments in the future. In addition, I want to give significant credit to Dr. Joseph A. Barranco, formerly a graduate student at the CFD lab, who shared valuable resources and insights with me through several meetings during my graduate years.

Also, I show my appreciation to the many friends who helped me avoid homesickness and live well in the San Francisco Bay Area, around 9,000 km apart from my hometown, Seoul. Among all of them worthy of my deep appreciation, I especially want to thank Hotae Lee and Jason J. Choi, long-time friends from high school and college, who also joined Berkeley at the same time and lived as my housemates for nearly five years without conflict. I know this enduring friendship has been possible because of their consideration and understanding, which I hope will remain strong in the future.

Last but not least, my efforts towards a doctorate would not have been meaningful without the continuous support and care of my family. I reaffirm my everlasting love and gratitude to my father, Kwang-Heon Lee, my mother, Soonran Kim, and my sister, Hwajeong “Hazell” Lee. Finally, I sincerely thank my beloved partner, Sooyeon Hwangbo, for securing our long-distance relationship with strong trust.

Introduction

Chapter 1

Introduction

1.1 Overview of wake vortices

With the progressive growth of commercial air traffic over the past decades, it has become increasingly common to spot and track fixed-wing aircraft flying in the sky. According to the Federal Aviation Administration (FAA), there were over 5,400 flights en route every minute during peak operational times on one day in 2023 in United States airspace (Matsunaga, 2024). As the statistics only took into account flights under instrumental flight rules (IFR), the actual number of flights, considering those under visual flight rules (VFR), should be higher. In the vicinity of busy airports on a clear day, it is not difficult to detect multiple airplanes flying through different routes at the same time, often leaving long visible traces along their pathways.

Among general aviation aircraft, the vast majority are classified as fixed-wing, and their long traces are necessary by-products of the lift force generated by the wings to counterbalance the aircraft's weight. Under typical flight conditions with high flow speeds, inertial effects generally dominate over viscous effects. Accordingly, if we put aside boundary layer effects, it can be said that wing lift is attributed to the circulation added to the potential flow region around the wing, which causes a pressure difference between the two sides of the wing that results in an upward net force. This wing-bound circulation must be shed downstream at every wing section according to Helmholtz's theorems, leading to a thin vortex sheet across the two ends of the wing (i.e., wingtips). The vortex sheet typically undergoes a roll-up process, where the vorticity concentrates into two discrete counter-rotating wake vortices in the extended downstream. Ultimately, this pair of wake vortices is the true nature of the long trace behind aircraft, extending far away from the originating aircraft.

The visibility of wake vortices, however, is not intrinsic. The disturbing motion caused by wake vortices is fundamentally invisible but we can observe its visible trace due to surrounding ice crystals from water vapor condensation around the vortices. The water vapor in the air and the aircraft jet exhaust condenses into ice crystals under proper temperature and humidity conditions, with ambient or jet exhaust soot particles aiding nucleation (see

Figure 1.1: Early-stage wake vortices behind cruising aircraft (see left) represented by a pair of long straight-line vortices. The structures are visible far downstream due to surrounding ice crystals from nearby water vapor condensation, also known as contrails. The scale bar in this photo is solely to offer a general sense of the wake vortices' length scale and is not based on precise quantification.

Kärcher, 2018). A considerable portion of these ice crystals may interact with the wake vortices and rotate around them. As a result, as far as these condensation trails (or contrails) are discernible, we can indirectly recognise the wake vortex structures (see figure 1.1). As one might already be aware, the important lesson behind here is that the actual streamwise span of wake vortices can remain much longer than the visible part. As a matter of fact, wake vortices are strongly persistent beyond their visible region, which can cause several practical problems in aircraft traffic control and airport runway operation, referred to as the wake vortex hazard (see Matalanis, 2007; Breitsamter, 2011).

Nonetheless, under certain atmospheric conditions where contrails do not quickly vanish, the later stages of wake vortices, after they lose their original straight-line shapes, can be observed. In figure 1.2, a structural change of two counter-rotating vortices through sinusoidal perturbation growth into a series of vortex rings is shown. This is one possible case representing the later wake vortex development undergoing destabilisation excited by surrounding factors, such as atmospheric turbulence. This instability mechanism was first identified by Crow (1970), who analyzed long-wavelength linear instabilities of the inviscid counter-rotating line vortex pair system. Subsequent researchers named this phenomenon the Crow instability. Crow (1970) described the "long" wavelength scale of excitatory perturbations in comparison to the separation distance between the vortex lines. Later, Moore and Saffman (1975) and Tsai and Widnall (1976) described "short" wavelength linear instabilities where the wavelength scale is comparable to the vortex core size. In this context, an individual vortex filament of non-zero (i.e., non-singular) core radius is considered, while the influence of the other vortex is interpreted as an external elliptic strain field. Long-wavelength and short-wavelength instabilities may occur simultaneously (see Leweke *et al.*, 2016), although the latter is not easily captured in real trailing vortices due to their existence at high altitude, as exemplified in figure 1.2.

In other cases, the wake vortex pair does not show clear signs of destabilisation and

Figure 1.2: Representative example of wake vortex destabilisation caused by the long-wavelength instability mechanism found by Crow (1970) under the inviscid counter-rotating line vortex pair configuration, which forms a series of vortex rings (see right) as a result of perturbation growth. The scale bar in this photo is solely to offer a general sense of the wake vortices' length scale and is not based on precise quantification.

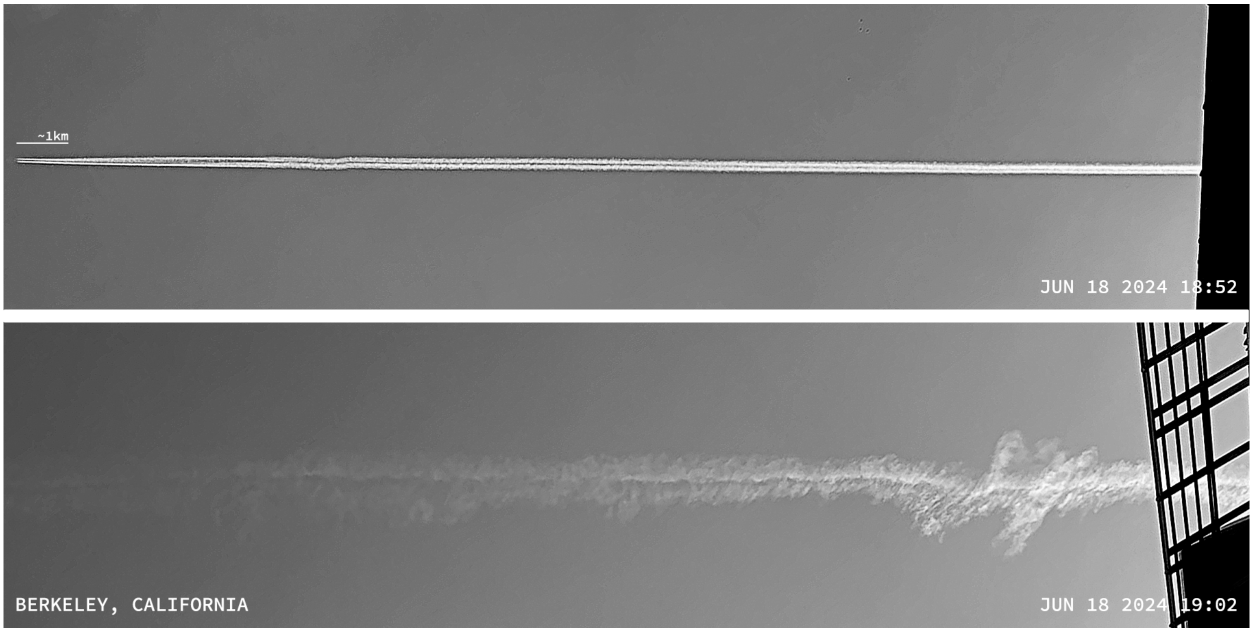

Figure 1.3: (Top) young persistent contrails under proper temperature and humidity atmospheric conditions. These aircraft-induced clouds, forming two parallel lines along the interacting wake vortices with no clear indication of destabilisation, remained visible for a long while, gradually diffusing to (bottom) spreading contrails with extended sky coverage. The scale bar in this photo is solely to offer a general sense of the wake vortices' length scale and is not based on precise quantification.

gradually spreads through viscous diffusion. An illustrative case is given in figure 1.3. This natural decay process is relatively slow but inevitable, as viscosity dissipates energy over time. The enlarged vortices exhibit slower velocities, thus posing reduced risks. However, for those who are interested in reducing the wake vortex hazard, relying upon viscous spreading would be impractical due to its excessively slow pace. Despite the fundamental question regarding the validity of assuming a steady base vortex when it comes to non-zero viscosity (see Mayer & Powell, 1992, pp. 105-106), several previous studies dealing with early-time linear instabilities of wake vortices, even at finite Reynolds numbers, neglected the viscous diffusion that expands the vortex core over time, yet obtained physically meaningful results for linear instabilities (e.g., Lessen *et al.*, 1974; Fabre & Jacquin, 2004; Lacaze *et al.*, 2007). This implies the marginal role of viscous diffusion in early-time vortex growth; nevertheless, one should not underestimate the importance of viscosity itself in vortex studies, as it is necessary to address singularities that are physically impossible to interpret, potentially disclosing new flow characteristics concealed in the inviscid limit.

For wake vortex alleviation, several strategies have been considered, including the excitation of vortex destabilisation. Some proposed passive means utilising time-independent wing modifications, while others suggested active means relying on time-dependent forcing actions (see Matalanis, 2007, pp. 7-17). On the other hand, Breitsamter (2011), by revisiting Gerz *et al.* (2002), described another categorisation based on essential design objectives. In one category, the objective is a low vorticity vortex (LVV) design, aiming to generate more dispersed vorticity over space right after roll-up. In the other category, a quickly decaying vortex (QDV) is primarily desired. Under this categorisation, the destabilisation approach aligns more closely with the latter as it attempts to understand and apply the most susceptible form of perturbation to invoke instabilities.

The stability or longevity of wake vortices (or any generic columnar vortices with or without axial momentum) has been a fascinating subject of research for a long time, garnering increasing attention since the late 20th century in the context of alleviating aircraft wake vortices (e.g., Dunham, 1977). Despite extensive research, this subject still holds many interesting riddles, both fundamentally and practically. There are numerous in-depth published studies worth exploring, which will be referenced throughout the main body of this study. The current research is built upon the foundation of their discoveries. For readers particularly interested in a more extensive overview of wake vortices, the review papers by Spalart (1998) and Widnall (1975) are recommended. Additionally, the relatively recent work by Hallock and Holzäpfel (2018) is suggested for those who view wake vortex problems from a slightly more practical perspective of air traffic issues.

1.2 Scope of research

We tackle the following questions. The persistence of wake vortices observable in the real world naturally raises the following fundamental questions:

- *Why can wake vortices last so long?*

- *Under what conditions can wake vortices be destabilised?*

These are questions worth considering, not only mathematically intriguing but also physically expandable, as the longevity of vortices is a general phenomenon occurring at various scales, from hurricanes on a meteorological scale to Jupiter's Great Red Spot on an extraterrestrial planetary scale. On the other hand, there is an additional question worth addressing from a practical point of view:

- *By what means can we initiate (or control) the destabilisation of wake vortices?*

This question aligns with the consideration of effective surrounding factors, devices, or strategies to promote rapid wake vortex destabilisation.

The primary inspiration for the current research comes from the fundamental aspects of vortex stability. Among the many theoretical configurations historically chosen for analyzing wake vortices, including single line vortices, vortex pairs, and multiple vortex pairs, we focus on the instabilities of a single vortex with different initial perturbations to explore the early-time growth of an individual vortex in a pair of wake vortices. Revisiting several previous findings, we search for an important but missing piece of information and attempt to unearth it. Specifically, what the current research aims to overcome are the limitations in computational approaches when it comes to dealing with singularities. Handling mathematical singularities via regularisation, usually referred to as critical layers in the context of this study, will be a recurrently emphasised concept over the study in efforts to distinguish physically meaningful outcomes from computational artifacts.

In the first part of the study (Part I), we go through a spectral method using associated Legendre functions with algebraic mapping for linear stability analysis of wake vortices. We then see that the developed computational approach successfully resolves critical-layer eigenmodes associated with the continuous spectrum in the inviscid limit, minimising false solutions that fail to properly resolve the singularities and potentially lead to incorrect conclusions on vortex instabilities. With viscosity, the analysis reveals newly discovered continuous curves in the spectra, termed the viscous critical-layer spectrum, which previous numerical studies might have been unable to spot within the larger continuum of the spectra.

In the second part of the study (Part II), we pay attention to the transient dynamics of a wake vortex. We confirm that the primary contribution to initial perturbations leading to optimal transient growth comes from the viscous critical-layer eigenmodes. The results obtained from the linearised analyses considered so far are validated in nonlinear simulations where perturbation energy is no longer restricted to a specific set of axial and azimuthal wavenumbers. Also, we investigate the initiation process of transient growth, considering the influence of weakly inertial particles on vortex dynamics. This exploration may reflect the interaction of contrails with wake vortices in real-world scenarios. Two-way coupled vortex-particle simulations are conducted, demonstrating the possibility of particle-initiated transient growth despite the system's linearly stable nature.

It is noted that this doctoral dissertation is essentially composed in a compilation style, meaning that the two parts (Parts I and II) presented hereafter may be considered as separate works. Readers may choose to refer to each part individually based on their specific needs. Nonetheless, these parts are closely interrelated and they may be read as a sequential series. For readers who decide to explore the entire study from beginning to end like a monograph style, this work will provide comprehensive information on early-time wake vortex growth, equipped with appropriate computational analyses and approaches.

Part I

Linear Stability Analysis

Chapter 2

Linear stability of a wake vortex

Nota bene
The majority of this part of study has been previously published as an open-access article in the *Journal of Fluid Mechanics* (see S. Lee & Marcus, 2023). It is primarily remarked that this previously published material is incorporated into this dissertation with reformatting in order to contribute to the larger, overarching theme: the early-time growth of a wake vortex.

2.1 Background

After the introduction of heavy commercial aircraft in the late 1960s, wake vortex motion has been a major subject of flow research, which has been reviewed in several studies (Widnall, 1975; Spalart, 1998; Breitsamter, 2011). The focus has often been on the destabilisation of wake vortices to alleviate wake hazards (see Hallock & Holzäpfel, 2018). The demise of wake vortices typically starts with vortex distortion, which causes either long-wavelength instability, well known as the Crow instability (Crow, 1970; Crow & Bate, 1976), or short-wavelength instability, known as the elliptical instability (Moore & Saffman, 1975; Tsai & Widnall, 1976). Both mechanisms are affected by vortex perturbation induced by the strain from the other vortex. The internal deformation of vortex cores, often interpreted as a combination of linear perturbation modes, plays a key role in the unstable vortex evolution process (Leweke *et al.*, 2016).

Since Lord Kelvin (1880) studied the linear perturbation modes of an isolated vortex using the Rankine vortex, analyses have been extended to other models that better describe a realistic vortex and account for viscosity with continual vorticity in space. The Lamb-Oseen vortex model can be considered as an exact solution to the Navier-Stokes equations, while assuming no axial current in vortex motion. Batchelor (1964), however, claimed the necessity of significant axial currents near and inside the vortex core for wake vortices and deduced vortex solutions with axial flows that are asymptotically accurate in the far field. The intermediate region between the vortex roll-up and the far field may be better described by the model proposed by Moore and Saffman (1973), where Feys and Maslowe (2014) performed a linear stability study. However, the Batchelor model has frequently been taken as a base flow for linear instability studies (Mayer & Powell, 1992; Fabre & Jacquin, 2004; Le Dizès & Lacaze, 2005; Heaton, 2007a; Qiu *et al.*, 2021), with the support of experimental observations (Leibovich, 1978; Maxworthy *et al.*, 1985). As for the Lamb-Oseen vortex, an exhaustive study on its linear perturbation was performed by Fabre *et al.* (2006). Bölle *et al.* (2021) conducted comprehensive linear analyses of all these vortex models and concluded that linear vortex dynamics is insensitive to changes in the base flow for singular modes.

In the numerical literature, a study by Lessen *et al.* (1974) used a shooting method to find eigensolutions of swirling flows, where the eigenmode represents the spatial profile of the linear perturbation, and the eigenvalue corresponds to its complex growth rate in time. Mayer and Powell (1992), on the other hand, utilised a spectral collocation method with Chebyshev polynomials to generate a global matrix eigenvalue problem in the generalised form ($\mathbf{A}\boldsymbol{x} = \lambda \mathbf{B}\boldsymbol{x}$). Although a shooting method may be accurate and less likely to yield spurious modes due to numerical discretisation (Boyd, 2001, pp. 139-142), a spectral collocation method should be preferred, especially when there is no initial guess, and the overall comprehension of the whole eigenmodes and eigenvalues is required. Heaton (2007a, pp. 335-339) compared these two numerical methods while investigating the asymptotic behaviour of inviscid unstable modes due to the presence of a core axial flow. Several recent studies (Fabre *et al.*, 2006; Mao & Sherwin, 2011) reported the use of spectral collocation methods to obtain a bulk of the eigensolutions at once to investigate and classify their common properties.

Given no viscosity ($\nu \equiv 0$), there are regular eigenmodes (Kelvin modes) in association with discretely distributed eigenvalues, and non-regular eigenmodes with critical layer singularities (critical-layer eigenmodes), which occur at radial locations where the perturbation phase velocity is equal to the advection of the base flow (Ash & Khorrami, 1995; Drazin & Reid, 2004), or equivalently, where the coefficients of the highest derivatives of the governing equations go to zero (Marcus *et al.*, 2015). The critical-layer eigenmodes arise from the non-normality of the governing equations (i.e., non-commutativity with the Hermitian adjoint) and are associated with continuously distributed eigenvalues in the complex plane, which are known to be significant in transient growth (Mao & Sherwin, 2011; Mao & Sherwin, 2012; Bölle *et al.*, 2021). Throughout this part, we refer to the region where critical-layer eigenvalues exist as a non-normal region. Note that this is in line with the quantitative definition of non-normality using the resolvent formalism by Bölle *et al.* (2021), who referred to non-normality as the region where the resolvent norm of the operator representing the governing equations does not meet its lower bound. The inviscid critical-layer eigenvalues are distributed on the imaginary axis, exhibiting their neutral stability pertaining to the time symmetry in the problem (see Gallay & Smets, 2020).

However, adding even a small amount of viscosity ($\nu \to 0^+$) breaks this symmetry and leads to the viscous damping of eigenmodes in time (Khorrami, 1991). Spatially, non-zero viscosity regularises the critical-layer singularities but simultaneously triggers new singularities at radial infinity as a result of the total spatial order increase of the governing equations (see Fabre *et al.*, 2006, p. 268). The impact of viscosity on the formation of viscous eigenmodes is an active research area, especially in the non-normal region. As viscosity is close to zero, the discrete spectrum becomes less prevalent in the complex plane while the non-normal region expands (see Bölle *et al.*, 2021, p. 11).

2.2 Research goals

Our primary goal is to develop an efficient numerical method for linear stability analysis of a wake vortex using eigenmode-eigenvalue theory (or spectral theory). We carefully investigate the mathematical foundation of the method to ensure accurate and correct resolving of eigenmodes and eigenvalues. We then apply our numerical method to linear stability analysis of the Lamb-Oseen or Batchelor vortex model to classify eigenmodes in terms of physical relevance, which is an additional goal for the rest of this part. Our work demonstrates the numerical efficiency of our method, which is essential as we plan to extend the application of the method to handle hundreds of eigenmodes for the examination of triad-resonant interactions among the eigenmodes in a follow-up paper, and encompasses the linear stability analyses under either inviscid or viscous conditions.

Our numerical work is based on a spectral collocation method. It follows the typical global eigenvalue problem-solving procedure like that of Boyd (2001, pp. 127-133) and Fabre *et al.* (2006, p. 241). However, our method is distinguished because of its use of algebraically mapped associated Legendre functions as Galerkin basis functions, which were introduced by Matsushima and Marcus (1997) and utilised in several vortex stability studies (Bristol *et al.*, 2004; Feys & Maslowe, 2016). These functions are defined as

$$P_{L_n}^m(r) \equiv P_n^m(\zeta(r,L)) = P_n^m\left(\frac{r^2-L^2}{r^2+L^2}\right) \quad (L>0), \tag{2.2.1}$$

where P_n^m is the associated Legendre function with order m and degree n (see Press *et al.*, 2007, pp. 292-295), ζ is a variable in the interval $-1 \le \zeta < 1$ to which the radial coordinate r is mapped by the map parameter L. Note that $\left\{P_{L_n}^m(r) \;\middle|\; n=|m|,\ |m|+1,\cdots\right\}$ is a complete Galerkin basis set, and a regular function approximated by their truncated sum converges exponentially with respect to the truncated degree $n_{\max}$.

Radial domain truncation is not required in our numerical method as it is designed for an unbounded radial domain. Other methods that require a radially bounded domain typically use a large truncation point to mimic unboundedness and impose arbitrary boundary conditions (Khorrami, 1991; Mayer & Powell, 1992; Mao & Sherwin, 2011; Bölle *et al.*, 2021). Moreover, our use of Galerkin basis functions eliminates the need for such explicit boundary conditions, reducing numerical error and eliminating further treatments for boundary conditions (see Zebib, 1987; McFadden *et al.*, 1990; Hagan & Priede, 2013). The distribution of numerical eigenvalues (numerical spectra) is necessarily discrete due to numerical discretisation, even if the analytic spectra are partially continuous. To deal with this seeming paradox, we investigate how the numerical spectra change with respect to the numerical parameters, including the map parameter L, the number of radial basis elements M, and the number of radial collocation points N. To complement the numerical spectra's inability to portray analytically continuous regions, we also briefly consider pseudospectral analysis (see Trefethen & Embree, 2005).

We are particularly focused on eigenmodes with a critical layer that has received little attention in previous numerical studies due to the difficulty of resolving them. Under the inviscid condition, the critical layers are mathematical point singularities. The critical-layer eigenmodes are associated with a continuous spectrum on the imaginary axis in the non-normal region. However, numerical discretisation often produces incorrect eigenvalues that appear as symmetric pairs around the imaginary axis (see Mayer & Powell, 1992). We show that our spectral collocation method can correct these results by properly adjusting the numerical parameters to reveal the inviscid critical-layer spectrum. With non-zero viscosity, there are areal spectra that emerge in the non-normal region (see Mao & Sherwin, 2011). These spectra have yet to be fully explained and may contain an unforeseen continuous spectrum. We demonstrate that our method is capable of resolving the eigenmodes associated with this unexplored spectrum, which results from the regularisation of critical layers, from the other eigenmodes in the non-normal region.

2.3 Preliminary remarks

To classify our numerically computed eigenmodes and eigenvalues, we frequently use the following terms in the rest of the paper. Note that some of our definitions may deviate from those used by other authors.

1. By "*physical*," we mean that a "*spatially resolved*" eigenmode (as defined below) is a non-singular solution to the linearised governing equations in an unbounded domain when computed with non-zero viscosity. An eigenmode computed with zero viscosity (i.e., with $\nu \equiv 0$) is not the target of consideration but may have physical significance if the eigenmode and eigenvalue correspond clearly to a "*physical*" eigenmode and eigenvalue computed with small but finite viscosity (i.e., in the limit of $\nu \to 0^+$). This condition is important because we are ultimately concerned with eigenmodes that can exist in the real world, such as those that would destabilise an aircraft wake vortex. Viscous eigenmodes are generally non-singular because viscosity can regularise them; numerically computed inviscid eigenmodes that would otherwise be singular are regularised by numerical discretisation. Our numerical method aims to resolve small-scale radial structures (e.g., the viscous remnants of inviscid critical layer singularities) purely resulting from physical (not numerical) regularisation, and we are interested in identifying such "*physical*" eigenmodes.

2. By "*non-physical*," we mean that a "*spatially resolved*" eigenmode does not meet the conditions described above for being considered "*physical*." Any numerically computed eigenmode must first be "*spatially resolved*" to be considered "*physical*." In addition, the eigenmode must satisfy the following requirements. First, if the eigenmode is

numerically computed in a truncated computational domain with a finite but large radius r_∞, there must be no bound at $r = r_\infty$ to ensure unboundedness. Second, the eigenmode's velocity and vorticity must approach zero at radial infinity, as we are interested in eigenmodes that develop in finite time from a wake vortex with vorticity localised in radius and not extending to infinity. Accordingly, eigenmodes that other authors have classified as part of the *freestream* family (Mao & Sherwin, 2011) are not in the scope of this part.

3. By "*spatially resolved*," we mean that the numerically computed eigenmode contains at least two collocation points in its smallest spatial structure (i.e., the radial width of the smallest wiggle). Additionally, the computed eigenvalue must either agree with its known value or converge to a fixed point. For an eigenvalue that belongs to the *discrete* spectrum, its eigenvalue must approach a fixed point as the number of radial basis elements M increases, and its corresponding eigenmode must converge to a fixed functional form. However, when dealing with an eigenvalue that belongs to the analytically continuous spectrum (where the spectrum lies along a curve, e.g., *critical-layer* spectrum; or where the spectrum fills an area in the complex plane, e.g., *potential* spectrum), there is ambiguity in numerically identifying a fixed point. This is because a finite matrix has only discrete eigenmodes. As M increases, the number of computed eigenmodes typically increases, and it is unclear whether a specific eigenvalue/eigenmode computed with M basis elements will correspond to *any* eigenvalue/eigenmode computed with $M+1$ basis elements. This is because the eigenvalues and eigenvectors of a matrix can be sensitive to the distances between the locations of the collocation points (which depend on M) and the radial structures of the eigenmodes. For discrete spectra, this sensitivity generally does not prevent us from tracking the evolution of as specific eigenvalue/eigenmode as M increases, but for continuous spectra, it does because eigenvalues are infinitesimally close to their neighbors. Therefore, in such cases, we determine whether the eigenvalue can be found within the expected range based on analytic results or reliable literature. In particular, for an inviscid eigenmode with a critical-layer singularity, its numerical solution will often suffer from the slow decay of spectral coefficients or the Gibbs phenomenon, especially around the singularity. Nonetheless, since our interest lies in identifying "*physical*" eigenmodes, we do not present a numerical method that exactly handles singularities. Our objective in analysing inviscid critical-layer eigenmodes is only to resolve their spatial characteristics outside the singularity neighbourhood by using a sufficiently large value of M.

4. By "*spurious*," we mean that a numerically computed eigenmode is not "*spatially resolved*," regardless of the value of M used in the computation. This definition of "*spurious*" originates from its historical usage (cf. Mayer & Powell, 1992). We can confirm that an eigenmode is "*non-spurious*" by increasing M until it becomes evident that the eigenmode is "*spatially resolved*." However, in practice, we cannot prove that

> an eigenmode is "*spurious*." It is always possible that, after increasing M to a large value and observing no evidence that the solution is approaching a fixed point, we abandon the increase in M due to computational budget constraints, and the solution would have converged with a further increase in M. Therefore, if we discuss whether some viscous eigenmode families are "*spurious*," the discussion will be suggestive rather than definitive.

The remainder of this part of study, from §3 to §8, is structured as follows. In §3, the governing equations for wake vortex motion are formulated and linearised . In §4, the spectral collocation method using mapped Legendre functions is presented. In §5, the Lamb-Oseen and Batchelor vortex eigenmode spectra and pseudospectra are described. In §6, the eigenmodes and eigenvalues of the inviscid problems are compared to the analytic results. In §7, the eigenmodes and eigenvalues in consideration of viscosity are presented, including a new family of eigenmodes in the continuous spectra that evolved from the family of critical-layer eigenmodes associated with the inviscid continuous spectrum. In §8, our findings are summarised.

Chapter 3

Problem formulation

3.1 Governing equations

In this research, we investigate the linear perturbation eigenmodes and eigenvalues of a swirling flow in an unbounded domain $\mathbb{R}^3$. We express the velocity and pressure eigenmodes in cylindrical coordinates (r, ϕ, z), as

$$\boldsymbol{u}' = \tilde{\boldsymbol{u}}(r; m, \kappa)e^{\mathrm{i}(m\phi+\kappa z)+\sigma t}, \quad p' = \tilde{p}(r; m, \kappa)e^{\mathrm{i}(m\phi+\kappa z)+\sigma t}, \tag{3.1.1}$$

where m and κ represent the azimuthal and axial wavenumbers of the eigenmode, respectively, and σ denotes the complex growth (or decay) rate of the eigenmode. Here, $m \in \mathbb{Z}$ since the fields must be periodic in ϕ with a period of 2π, while $\kappa \in \mathbb{R} \setminus 0$ since there are no restrictions on the axial wavelength $2\pi/\kappa$. The real part of σ represents the growth/decay rate, while the imaginary part represents its wave frequency in time. Although Khorrami *et al.* (1989) formulated a more general problem, we employ a more specialised form of the steady, equilibrium, swirling flow $\overline{\boldsymbol{U}}$, i.e.,

$$\overline{\boldsymbol{U}}(r) = \overline{U}_\phi(r)\hat{\boldsymbol{e}}_\phi + \overline{U}_z(r)\hat{\boldsymbol{e}}_z, \tag{3.1.2}$$

which is only r-dependent and has no radial velocity component $\overline{U}_r$. The unperturbed base flow profile we consider for a wake vortex model is Batchelor's similarity solution adapted by Lessen *et al.* (1974) with

$$\frac{\overline{U}_\phi}{U_0} = \frac{1 - e^{-r^2/R_0^2}}{r/R_0}, \qquad \frac{\overline{U}_z}{U_0} = \frac{1}{q}e^{-r^2/R_0^2}, \tag{3.1.3}$$

where R_0 and U_0 are the length and velocity scales defined in Lessen *et al.* (1974, p. 755), and $q \neq 0$ is a dimensionless swirl parameter. This flow is often called the q-vortex, which is steady, axisymmetric, and analytically tractable as the far-field asymptotic solution under the viscous light-loading condition (see Saffman, 1993, pp. 257-260). When the axial flow component vanishes, i.e., $1/q \to 0$, this flow is equivalent to the Lamb-Oseen vortex. A

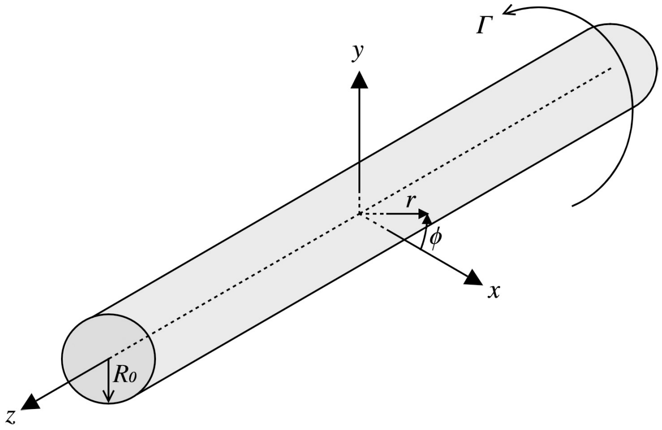

Figure 3.1: Vortex with circulation Γ of length scale R_0 and coordinate systems.

schematic of the geometry is shown in figure 3.1. The unperturbed vortex is oriented along the z-direction with a circulation over the entire plane $\Gamma \equiv 2\pi R_0 U_0$. R_0 is referred to as the characteristic radius of the vortex. As for the vortex profile, we consider the azimuthal velocity $\overline{U}_\phi$, which is maximised at $r = 1.122R_0$ (Lessen *et al.*, 1974).

To establish governing equations, we assume the fluid has constant density ρ and constant kinematic viscosity ν. The total velocity $\boldsymbol{u} \equiv u_r\hat{\boldsymbol{e}}_r + u_\phi\hat{\boldsymbol{e}}_\phi + u_z\hat{\boldsymbol{e}}_z$ obeys

$$\boldsymbol{\nabla} \cdot \boldsymbol{u} = 0, \tag{3.1.4}$$

$$\frac{\partial \boldsymbol{u}}{\partial t} = -\left(\boldsymbol{u} \cdot \boldsymbol{\nabla}\right)\boldsymbol{u} - \frac{1}{\rho}\boldsymbol{\nabla} p + \nu\nabla^2\boldsymbol{u} = -\boldsymbol{\nabla}\varphi + \boldsymbol{u} \times \boldsymbol{\omega} + \nu\nabla^2\boldsymbol{u}, \tag{3.1.5}$$

where the total pressure is p, the vorticity is $\boldsymbol{\omega} \equiv \boldsymbol{\nabla} \times \boldsymbol{u}$ and the total specific energy is $\varphi \equiv u^2/2 + p/\rho$ where $u^2 \equiv \boldsymbol{u} \cdot \boldsymbol{u}$. We non-dimensionalise the equations using R_0 as the unit of length and R_0/U_0 as the unit of time. After non-dimensionalising and linearising (3.1.4)–(3.1.5) about the unperturbed flow (indicated with overbars $\overline{*}$), we obtain the following equation for the perturbations (indicated with primes $*'$):

$$\boldsymbol{\nabla} \cdot \boldsymbol{u}' = 0, \tag{3.1.6}$$

$$\frac{\partial \boldsymbol{u}'}{\partial t} = -\boldsymbol{\nabla}\varphi' + \overline{\boldsymbol{U}}(r) \times \boldsymbol{\omega}' - \overline{\boldsymbol{\omega}}(r) \times \boldsymbol{u}' + \frac{1}{Re}\nabla^2\boldsymbol{u}', \tag{3.1.7}$$

where the Reynolds number, denoted Re, is defined to be U_0R_0/ν. Note that the non-dimensionalised q-vortex is

$$\overline{\boldsymbol{U}}(r) = \left(\frac{1 - e^{-r^2}}{r}\right)\hat{\boldsymbol{e}}_\phi + \left(\frac{1}{q}e^{-r^2}\right)\hat{\boldsymbol{e}}_z. \tag{3.1.8}$$

The established governing equations are essentially the incompressible, linearised Navier-Stokes equations, which, in combination with the q-vortex, were also used in recent vortex stability analyses, such as Qiu *et al.* (2021). By putting (3.1.1) to (3.1.6)–(3.1.7), we obtain the equations that govern the perturbations:

$$\boldsymbol{\nabla}_{m\kappa} \cdot \tilde{\boldsymbol{u}} = 0, \tag{3.1.9}$$

$$\sigma \tilde{\boldsymbol{u}} = -\boldsymbol{\nabla}_{m\kappa} \tilde{\varphi} + \overline{\boldsymbol{U}} \times \tilde{\boldsymbol{\omega}} - \overline{\boldsymbol{\omega}} \times \tilde{\boldsymbol{u}} + \frac{1}{Re} \nabla^2_{m\kappa} \tilde{\boldsymbol{u}}, \tag{3.1.10}$$

where σ is a function of m and κ (i.e., it obeys the dispersion relationship), $\tilde{\boldsymbol{\omega}} \equiv \boldsymbol{\nabla}_{m\kappa} \times \tilde{\boldsymbol{u}}$, and $\tilde{\varphi} \equiv \overline{\boldsymbol{U}} \cdot \tilde{\boldsymbol{u}} + \tilde{p}$. In the equations above, the subscript $(*)_{m\kappa}$ attached to the operators means that they act on modes of fixed azimuthal and axial wavenumbers m and κ. Therefore, the differential operators $\partial/\partial\phi$ and $\partial/\partial z$ inside these operators are replaced with the simple multiplication operators $\mathrm{i}m$ and $\mathrm{i}\kappa$, respectively (see Appendix A).

3.2 Boundary and analyticity conditions

We require both the velocity and pressure fields to be analytic at $r = 0$ and to decay rapidly to 0 as $r \to \infty$. The conversion of these conditions to numerical boundary conditions can be found in previous works such as Batchelor and Gill (1962), Mayer and Powell (1992), and Ash and Khorrami (1995). In this section, we briefly discuss these conditions and how they will be treated in our method, where functions are treated as a truncated sum of the mapped Legendre functions.

The analyticity at the origin is equivalent to the pole condition that correctly removes the coordinate singularity (see Canuto *et al.*, 1988; Matsushima & Marcus, 1995; Lopez *et al.*, 2002). The pole condition for a scalar function $f(r, \phi, z)$ to be analytic at $r = 0$ is that it asymptotically behaves as a polynomial in r, with the degree dependent on the azimuthal wavenumber m (see Matsushima & Marcus, 1997, p. 323), that is,

$$f(r, \phi, z) = \sum_{m=-\infty}^{\infty} e^{\mathrm{i}m\phi} r^{|m|} \left(\sum_{n=0}^{\infty} C_n(z; m) r^{2n} \right) \quad \text{as } r \to 0, \tag{3.2.1}$$

for some set of functions, analytic in z, $C_n(z; m)$. Although the pole condition for velocity fields in polar or cylindrical coordinates is rather complicated because of the velocity coupling of r and ϕ at the origin (see Matsushima & Marcus, 1997, pp. 328-330), we use toroidal and poloidal streamfunctions, given in (3.3.1), instead of the primitive velocity components so that the analyticity can be determined by making these streamfunctions obey the requirements of scalars (see Appendix B).

On the other hand, the rapid decay condition as $r \to \infty$ is relevant to the feasibility of linear perturbations. Since a perturbation lasting even at radial infinity would require infinite kinetic energy, decay should be necessary to consider it physical (see our definition in §2.3). The simplest description is $\tilde{\boldsymbol{u}}$, $\tilde{p} \to 0$ as $r \to \infty$ (Batchelor & Gill, 1962). Several numerical methods that require the domain truncation at large r mimic this condition by imposing the homogeneous Dirichlet boundary condition for $\tilde{\boldsymbol{u}}$ and $\tilde{p}$ at the outer boundary of the radially truncated domain $r = r_\infty$. In other words, $\tilde{u}_r = \tilde{u}_\phi = \tilde{u}_z = \tilde{p} = 0$ at $r = r_\infty$ (see Khorrami *et al.*, 1989; Khorrami, 1991). However, this approach involves two problems. First, it cannot preclude non-physical eigenmode solutions that do not decay properly but incidentally end up being zero at $r = r_\infty$ (i.e., wall-bounded modes). Such non-physical solutions may also appear with non-zero viscosity, triggering non-normalisable singularities at radial infinity, where more information can be found in Fabre *et al.* (2006, p. 268) or Mao and Sherwin (2011, pp. 17-21). Second, it does not explicitly take into account how rapidly the perturbation decays. Considering the velocity field, it must decay faster than algebraic decay rates of $O(r^{-1})$ for kinetic energy to be finite as $r \to \infty$ (cf. Bölle *et al.*, 2021). Mathematically, the restriction is even more strict, requiring exponential or super-exponential decay rates (Ash & Khorrami, 1995). Our method is free from domain truncation and explicitly forces solutions to decay harmonically, i.e., $O(r^{-|m|}e^{im\phi})$ as $r \to \infty$, due to the decaying nature of the basis functions.

By utilising the current method, it can be ensured that any scalar functions, represented by the sum of mapped Legendre functions that serve as Galerkin basis functions, comply with the aforementioned conditions. This is precisely how each basis function behaves as the radial distance approaches zero and approaches infinity. Therefore, an advantage of employing the mapped associated Legendre functions is that there is no need for additional treatment for numerical boundary conditions. For further information regarding the properties of the mapped Legendre functions, please refer to §4.

3.3 Poloidal-toroidal decomposition

The governing equations (3.1.9) - (3.1.10), along with the correct boundary conditions and given values of m and κ, formally constitute a set of four equations that make up a generalised eigenvalue problem in terms of $\tilde{p}$ (or $\tilde{\varphi}$) and the three components of $\tilde{\boldsymbol{u}} \equiv \tilde{u}_r \hat{\boldsymbol{e}}_r + \tilde{u}_\phi \hat{\boldsymbol{e}}_\phi + \tilde{u}_z \hat{\boldsymbol{e}}_z$, which are often referred to as primitive variables, with σ as the eigenvalue. The formal expression of the eigenvalue problem can be found in Bölle *et al.* (2021, p. 7). Some previous studies have taken additional steps to eliminate $\tilde{p}$ from the momentum equations or even reduce the problem in terms of, for example, only $\tilde{u}_\phi$ and $\tilde{u}_z$, resulting in the generalised eigenvalue problem form $\mathbf{A}\boldsymbol{x} = \lambda \mathbf{B}\boldsymbol{x}$ (Mayer & Powell, 1992; Heaton & Peake, 2007; Mao & Sherwin, 2011). However, such variable reduction inevitably increases the spatial order of the system and, consequently, requires a higher resolution for computation, which undermines the advantage of having a smaller number of state variables (Mayer & Powell, 1992). To avoid this issue, we use a poloidal-toroidal decomposition of the velocity field to formulate the matrix eigenvalue problem while preserving the spatial order of the governing equations. Moreover, the use of the poloidal and toroidal streamfunctions is advantageous because the formulation results in the standard eigenvalue problem of the form $\mathbf{A}\boldsymbol{x} = \lambda\boldsymbol{x}$.

To begin with, we apply the poloidal-toroidal decomposition to the governing equations of wake vortices that are linearised about the q-vortex. The basic formulation was performed by Matsushima and Marcus (1997, p. 339), and we provide more details of its mathematical foundation in this section. Although the poloidal-toroidal decomposition of solenoidal vector fields is mainly discussed in spherical geometry (Chandrasekhar, 1981, pp. 622-626), it can be employed in the cylindrical coordinate system while preserving some essential properties of the decomposition (Ivers, 1989). When we select the unit vector in the z-direction $\hat{\boldsymbol{e}}_{\boldsymbol{z}}$ as a reference vector, a solenoidal vector field $\boldsymbol{V}(r,\phi,z) = V_r(r,\phi,z)\hat{\boldsymbol{e}}_{\boldsymbol{r}} + V_\phi(r,\phi,z)\hat{\boldsymbol{e}}_{\boldsymbol{\phi}} + V_z(r,\phi,z)\hat{\boldsymbol{e}}_{\boldsymbol{z}}$ can be expressed as

$$\boldsymbol{V} = \boldsymbol{\nabla} \times \left\{\psi(r,\phi,z)\hat{\boldsymbol{e}}_{\boldsymbol{z}}\right\} + \boldsymbol{\nabla} \times \Big[\boldsymbol{\nabla} \times \left\{\chi(r,\phi,z)\hat{\boldsymbol{e}}_{\boldsymbol{z}}\right\}\Big], \tag{3.3.1}$$

where ψ and χ are the toroidal and poloidal streamfunctions of $\boldsymbol{V}$. Such a decomposition is feasible if $\boldsymbol{V}$ has zero spatial mean components in the radial and azimuthal directions over an infinite disk for all z (cf. Jones, 2008). This zero-mean condition is satisfied in our study because our velocity fields are spatially periodic perturbations of the base flow. Ivers (1989) concluded that the toroidal and poloidal fields are orthogonal over an infinite slab $a < z < b$ if ψ and χ decay sufficiently rapidly as $r \to \infty$. The decay condition of ψ and χ requires $\boldsymbol{V}$ to decay sufficiently rapidly to zero for large r.

In what follows, we find more rigorous statement for the decay condition of $\boldsymbol{V}$ as $r \to \infty$ where ψ and χ are well-defined. The z-component of (3.3.1) is

$$\frac{1}{r}\frac{\partial}{\partial r}\left(r\frac{\partial \chi}{\partial r}\right) + \frac{1}{r^2}\frac{\partial^2 \chi}{\partial \phi^2} = -V_z. \tag{3.3.2}$$

Taking the curl of (3.3.1), we obtain

$$\boldsymbol{\nabla} \times \boldsymbol{V} = \boldsymbol{\nabla} \times \left\{(-\nabla^2\chi)\hat{\boldsymbol{e}}_{\boldsymbol{z}}\right\} + \boldsymbol{\nabla} \times \left\{\boldsymbol{\nabla} \times (\psi\hat{\boldsymbol{e}}_{\boldsymbol{z}})\right\}, \tag{3.3.3}$$

with its z-component equal to

$$\frac{1}{r}\frac{\partial}{\partial r}\left(r\frac{\partial \psi}{\partial r}\right) + \frac{1}{r^2}\frac{\partial^2 \psi}{\partial \phi^2} = -\left(\boldsymbol{\nabla} \times \boldsymbol{V}\right)_z. \tag{3.3.4}$$

Solving (3.3.2) and (3.3.4), which are the two-dimensional Poisson equations, can yield the solution to ψ and χ. By ignoring the gauge freedom with respect to z, we can determine the solution using two-dimensional convolution as follows:

$$\psi = -\left(\boldsymbol{\nabla} \times \boldsymbol{V}\right)_z * \Phi, \tag{3.3.5}$$

$$\chi = -V_z * \Phi, \tag{3.3.6}$$

where Φ is Green's function for the entire plane $\mathbb{R}^2$ equivalent to

$$\Phi(r,\phi) = \frac{1}{2\pi}\ln r. \tag{3.3.7}$$

In order for the convolutions in (3.3.5) and (3.3.6) to be meaningful everywhere, there exist $p_1 > 0$, $p_2 > 0$ and $p_3 > 0$ such that

$$\begin{cases} V_r \sim O\left(r^{-1-p_1}\right) \\ V_\phi \sim O\left(r^{-1-p_2}\right) \\ V_z \sim O\left(r^{-2-p_3}\right) \end{cases} \qquad \text{as } r \to \infty, \tag{3.3.8}$$

given that $\boldsymbol{V}$ decays algebraically. Otherwise, $\boldsymbol{V}$ may decay exponentially or superexponentially. If $\boldsymbol{V}$ is referred to as a velocity field, it has finite total kinetic energy over the entire space since all components decay faster than $O(r^{-1})$ as $r \to \infty$. The finite kinetic energy condition is physically reasonable, especially when dealing with velocity fields representing small perturbations (cf. Bölle *et al.*, 2021). On the other hand, Matsushima and Marcus (1997) considered the case where ψ and χ could be unbounded by including additional logarithmic terms in ψ and χ, providing a more comprehensive extension of the poloidal-toroidal decomposition to more general vector fields, including the mean axial components. However, in the present study, we choose $\boldsymbol{V}$ as a linear perturbation of no bulk movement, and therefore the logarithmic terms do not need to be considered.

Suppressing the gauge freedom by adding restrictions that are independent of z to ψ and χ , e.g.,

$$\lim_{r\to\infty} \psi(r,\phi,z) = \lim_{r\to\infty} \chi(r,\phi,z) = 0, \tag{3.3.9}$$

we can define the following linear and invertible operator $\mathbb{P} : \mathcal{U} \to \mathcal{P}$ as

$$\mathbb{P}(\boldsymbol{V}) \equiv \begin{pmatrix} \psi(r,\phi,z) \\ \chi(r,\phi,z) \end{pmatrix}, \tag{3.3.10}$$

where $\mathcal{U}$ is the set of sufficiently rapidly decaying solenoidal vector fields from $\mathbb{R}^3$ to $\mathbb{R}^3$ ($\mathbb{C}^3$) that satisfy (3.3.8) and $\mathcal{P}$ is the set of functions from $\mathbb{R}^3$ to $\mathbb{R}^2$ ($\mathbb{C}^2$) that satisfy (3.3.9). Using Helmholtz's theorem, we may extensively define $\mathbb{P}$ on more generalised vector fields which are not solenoidal but their solenoidal portion can be decomposed toroidally and poloidally. If we expand the domain of $\mathbb{P}$, however, it should be kept in mind that the operator is no longer injective because for any $\boldsymbol{V} \in \mathcal{U}$, $\mathbb{P}(\boldsymbol{V}) = \mathbb{P}(\boldsymbol{V} + \boldsymbol{\nabla} v)$ where v is an arbitrary scalar potential for a non-zero irrotational vector field. On the other hand, it is noted that $\mathbb{P}(\nabla^2 \boldsymbol{V}) = \nabla^2 \mathbb{P}(\boldsymbol{V}) \equiv (\nabla^2\psi, \nabla^2\chi)$ for $\boldsymbol{V} \in \mathcal{U}$ because

$$\begin{aligned} &\nabla^2\Big[\boldsymbol{\nabla}\times\left\{\psi(r,\phi,z)\hat{\boldsymbol{e}}_{\boldsymbol{z}}\right\} + \boldsymbol{\nabla}\times\Big[\boldsymbol{\nabla}\times\left\{\chi(r,\phi,z)\hat{\boldsymbol{e}}_{\boldsymbol{z}}\right\}\Big]\Big] \\ &= \boldsymbol{\nabla}\times\left\{\nabla^2\psi(r,\phi,z)\hat{\boldsymbol{e}}_{\boldsymbol{z}}\right\} + \boldsymbol{\nabla}\times\Big[\boldsymbol{\nabla}\times\left\{\nabla^2\chi(r,\phi,z)\hat{\boldsymbol{e}}_{\boldsymbol{z}}\right\}\Big]. \end{aligned} \tag{3.3.11}$$

Applying the operator $\mathbb{P}$ to both sides of (3.1.7), we obtain

$$\frac{\partial \mathbb{P}(\boldsymbol{u}')}{\partial t} = \mathbb{P}\left(\overline{\boldsymbol{U}}(r)\times\boldsymbol{\omega}'\right) - \mathbb{P}\left(\overline{\boldsymbol{\varpi}}(r)\times\boldsymbol{u}'\right) + \frac{1}{Re}\nabla^2\mathbb{P}(\boldsymbol{u}'), \tag{3.3.12}$$

because $\mathbb{P}(\boldsymbol{\nabla}\varphi) = \mathbb{P}(\mathbf{0} + \boldsymbol{\nabla}\varphi) = \mathbb{P}(\mathbf{0}) = \mathbf{0}$. Assuming $\boldsymbol{u}'$ to be solenoidal, $\boldsymbol{u}'$ automatically satisfies the continuity equation and can be determined from $\mathbb{P}(\boldsymbol{u}')$ by taking the inverse of it using (3.3.1).

Since we are interested in the perturbation velocity field as in (3.1.1), we define two r-dependent scalar functions $\tilde{\psi}(r; m, \kappa)$ and $\tilde{\chi}(r; m, \kappa)$ such that

$$\mathbb{P}\left(\tilde{\boldsymbol{u}}(r; m, \kappa) e^{\mathrm{i}(m\phi + \kappa z) + \sigma t}\right) = \begin{pmatrix} \tilde{\psi}(r; m, \kappa) e^{\mathrm{i}(m\phi + \kappa z) + \sigma t} \\ \tilde{\chi}(r; m, \kappa) e^{\mathrm{i}(m\phi + \kappa z) + \sigma t} \end{pmatrix}. \tag{3.3.13}$$

The fact that the poloidal and toroidal components in (3.3.13) preserve the exponential part can be verified by substituting the perturbation velocity field formula into $\boldsymbol{V}$ in (3.3.2) and (3.3.4). For convenience, we simplify the expression in (3.3.13) to

$$\mathbb{P}_{m\kappa}(\tilde{\boldsymbol{u}}(r; m, \kappa)) \equiv \begin{pmatrix} \tilde{\psi}(r; m, \kappa) \\ \tilde{\chi}(r; m, \kappa) \end{pmatrix}. \tag{3.3.14}$$

Finally, putting (3.1.1) into (3.3.12) leads to the standard eigenvalue problem form in terms of $\mathbb{P}_{m\kappa}(\tilde{\boldsymbol{u}}(r; m, \kappa))$:

$$\sigma\big[\mathbb{P}_{m\kappa}(\tilde{\boldsymbol{u}}(r; m, \kappa))\big] = \mathcal{L}^{\nu}_{m\kappa}\big[\mathbb{P}_{m\kappa}(\tilde{\boldsymbol{u}}(r; m, \kappa))\big], \tag{3.3.15}$$

where the linear operator $\mathcal{L}^{\nu}_{m\kappa}$ is defined as

$$\mathcal{L}^{\nu}_{m\kappa}\big[\mathbb{P}_{m\kappa}(\tilde{\boldsymbol{u}})\big] \equiv \mathbb{P}_{m\kappa}\left(\overline{\boldsymbol{U}}(r) \times \tilde{\boldsymbol{\omega}}\right) - \mathbb{P}_{m\kappa}\left(\overline{\boldsymbol{\omega}}(r) \times \tilde{\boldsymbol{u}}\right) + \frac{1}{Re}\nabla^2_{m\kappa}\mathbb{P}_{m\kappa}(\tilde{\boldsymbol{u}}). \tag{3.3.16}$$

Excluding the viscous diffusion term, we additionally define the inviscid operator $\mathcal{L}^{0}_{m\kappa}$ as

$$\mathcal{L}^{0}_{m\kappa}\big[\mathbb{P}_{m\kappa}(\tilde{\boldsymbol{u}})\big] \equiv \mathbb{P}_{m\kappa}\left(\overline{\boldsymbol{U}}(r) \times \tilde{\boldsymbol{\omega}}\right) - \mathbb{P}_{m\kappa}\left(\overline{\boldsymbol{\omega}}(r) \times \tilde{\boldsymbol{u}}\right), \tag{3.3.17}$$

for the inviscid linear analysis solving

$$\sigma\big[\mathbb{P}_{m\kappa}(\tilde{\boldsymbol{u}}(r; m, \kappa))\big] = \mathcal{L}^{0}_{m\kappa}\big[\mathbb{P}_{m\kappa}(\tilde{\boldsymbol{u}}(r; m, \kappa))\big]. \tag{3.3.18}$$

Chapter 4

Numerical method

4.1 Mapped Legendre functions

Associated Legendre functions with algebraic mapping are used as basis functions to expand an arbitrary function over $0 \leq r < \infty$, ultimately discretising the eigenvalue problems to be solved numerically. The expansion was first introduced by Matsushima and Marcus (1997) and applied to three-dimensional vortex instability studies by Bristol *et al.* (2004) and Feys and Maslowe (2016). The algebraically mapped associated Legendre functions $P_{L_n}^m(r)$, or simply mapped Legendre functions, are equivalent to the mapping of the associate Legendre functions $P_n^m(\zeta)$ with order m and degree n defined on $-1 \leq \zeta < 1$ where

$$\zeta \equiv \frac{r^2 - L^2}{r^2 + L^2} \iff r = L\sqrt{\frac{1+\zeta}{1-\zeta}}. \tag{4.1.1}$$

An additional parameter $L > 0$ is the map parameter, which can be arbitrarily set. However, when it is used for a spectral collocation method, change in L affects the spatial resolution of discretisation and the value should be carefully chosen to achieve fast convergence or eliminate spurious results. Matsushima and Marcus (1997) showed that $P_{L_n}^m(r) \sim O(r^{|m|})$ as $r \to 0$ and $P_{L_n}^m(r) \sim O(r^{-|m|})$ as $r \to \infty$, which leads to the fact that any polar function $P_{L_n}^m(r)e^{\mathrm{i}m\phi}$ behaves analytically at the origin (see Eisen *et al.*, 1991, pp. 243-244) and decays harmonically to zero at radial infinity. These asymptotic properties are suitable to apply the correct boundary conditions for the present problem.

Next, we prove that a set of some mapped Legendre functions can constitute a complete orthogonal basis of spectral space. Since the associate Legendre functions $P_n^m(\zeta)$ are the solutions to the associate Legendre equation

$$\frac{d}{d\zeta}\left[\left(1-\zeta^2\right)\frac{dP_n^m}{d\zeta}\right] + \left[n(n+1) - \frac{m^2}{1-\zeta^2}\right]P_n^m(\zeta) = 0, \tag{4.1.2}$$

the mapped Legendre functions satisfy the following second-order differential equation

$$\frac{d}{dr}\left[r\frac{dP_{L_n}^m}{dr}\right] - \frac{m^2}{r}P_{L_n}^m(r) + \frac{4n(n+1)L^2 r}{(L^2+r^2)^2}P_{L_n}^m(r) = 0. \tag{4.1.3}$$

As (4.1.3) is the Sturm-Liouville equation with the weight function

$$w(r) \equiv \frac{4L^2 r}{(L^2 + r^2)^2}, \tag{4.1.4}$$

the mapped Legendre functions $P^m_{L_{|m|}}(r)$, $P^m_{L_{|m|+1}}(r)$, $P^m_{L_{|m|+2}}(r)$, $\cdots$ form an orthogonal basis of the Hilbert space $L^2\left(\mathbb{R}^+, w(r)dr\right)$. Thus, for two integers n and k larger than or equal to $|m|$,

$$\begin{aligned} \left\langle P^m_{L_n}, P^m_{L_k} \right\rangle &= \int_0^\infty P^m_{L_n}(r) P^m_{L_k}(r) w(r) dr \\ &= \int_{-1}^1 P^m_n(\zeta) P^m_k(\zeta) d\zeta = \frac{2(n+|m|)!}{(2n+1)(n-|m|)!}\delta_{nk}, \end{aligned} \tag{4.1.5}$$

where δ_{nk} denotes the Kronecker delta with respect to n and k.

Considering a polar function $f_m(r)e^{\mathrm{i}m\phi}$ where $f_m \in L^2\left(\mathbb{R}^+, w(r)dr\right)$, it can be expanded by the mapped Legendre functions as

$$f_m(r)e^{\mathrm{i}m\phi} = \sum_{n=|m|}^{\infty} f^m_n P^m_{L_n}(r) e^{\mathrm{i}m\phi}, \tag{4.1.6}$$

and the coefficient f^m_n can be calculated based on the orthogonality of the basis functions:

$$\begin{aligned} f^m_n = \frac{\left\langle f_m, P^m_{L_n} \right\rangle}{\left\langle P^m_{L_n}, P^m_{L_n} \right\rangle} &= \frac{(2n+1)(n-|m|)!}{2(n+|m|)!} \int_0^\infty f_m(r) P^m_{L_n}(r) w(r) dr \\ &= \frac{(2n+1)(n-|m|)!}{2(n+|m|)!} \int_{-1}^1 f_m\left(L\sqrt{\frac{1+\zeta}{1-\zeta}}\right) P^m_n(\zeta) d\zeta. \end{aligned} \tag{4.1.7}$$

When we expand an analytic function on $0 \leq r < \infty$ that vanishes at infinity, the expansion in (4.1.6) is especially suitable because they are able to serve as Galerkin basis functions. Even if we use the truncated series of (4.1.6), analyticity at the origin and vanishing behaviour at infinity remain valid.

4.2 Mapped Legendre spectral collocation method

In order to discretise the problem, we use a spectral collocation method using the mapped Legendre functions as basis functions. Given the azimuthal and axial wavenumbers m and κ, we take a truncated basis set of first M elements $\{P^m_{L_{|m|}}, \cdots, P^m_{L_{|m|+M-1}}\}$ and expand $f_m(r)e^{\mathrm{i}(m\phi+\kappa z)}$ as

$$f_m(r)e^{\mathrm{i}(m\phi+\kappa z)} = \sum_{n=|m|}^{|m|+M-1} f^m_n P^m_{L_n}(r) e^{\mathrm{i}(m\phi+\kappa z)}, \tag{4.2.1}$$

so that the function is represented by M discretised coefficients $(f^m_{|m|}, \cdots, f^m_{|m|+M-1})$. The coefficients are numerically obtained by applying the Gauss-Legendre quadrature rule to (4.1.7). Let ζ_j and ϖ_j be the jth root of the Legendre polynomial P_N of degree N in $(-1, 1)$ with its quadrature weight defined as

$$\varpi_j = 2(1-\zeta_j^2)^{-1}\left[\left.\frac{dP_N}{d\zeta}\right|_{\zeta=\zeta_j}\right]^{-2}, \quad j = 1, \cdots, N, \tag{4.2.2}$$

and with radial collocation points r_j determined from (4.1.1) as

$$r_j \equiv L\sqrt{\frac{1+\zeta_j}{1-\zeta_j}}, \quad j = 1, \cdots, N, \tag{4.2.3}$$

which means that half of the collocation points are distributed in the inner high-resolution region $0 \leq r < L$ whereas the other half are posed in the outer low-resolution region $r \geq L$ (Matsushima & Marcus, 1997). In order to describe spatial resolution, we define the characteristic resolution parameter Δ as

$$\Delta(N, L) \equiv \frac{2L}{N}, \tag{4.2.4}$$

which represents the mean spacing between the collocation points in $0 \leq r < L$.

A quadrature algorithm presented by Press *et al.* (2007, pp. 179-194) is implemented and all abscissas and weights are computed with an absolute precision error less than 10^{-15}. The quadrature converts the integration formula to the weighted sum of the function values evaluated at the collocation points and consequently the integral of (4.1.7) finally becomes the discretised formula

$$f^m_n \simeq \frac{(2n+1)(n-|m|)!}{2(n+|m|)!}\sum_{j=1}^{N}\varpi_j f_m(r_j)P^m_n(\zeta_j). \tag{4.2.5}$$

It is convenient in practice to conceal the factorial coefficient term by defining the normalised mapped Legendre functions and coefficients as follows:

$$\hat{P}^m_{L_n}(r) \equiv P^m_{L_n}(r)\sqrt{\frac{(2n+1)(n-|m|)!}{2(n+|m|)!}}, \qquad \hat{f}^m_n \equiv f^m_n\sqrt{\frac{2(n+|m|)!}{(2n+1)(n-|m|)!}}. \tag{4.2.6}$$

Using these normalised terms, (4.2.5) can be expressed as

$$\hat{f}^m_n \simeq \sum_{j=1}^{N}\varpi_i f_m(r_j)\hat{P}^m_n(\zeta_j), \tag{4.2.7}$$

and, moreover, (4.2.1) at $r = r_j$ maintains the identical form

$$f_m(r_j)e^{\mathrm{i}(m\phi+\kappa z)} = \sum_{n=|m|}^{|m|+M-1} \hat{f}_n^m \hat{P}_{L_n}^m(r_j)e^{\mathrm{i}(m\phi+\kappa z)}. \tag{4.2.8}$$

As a preliminary step of the mapped Legendre spectral collocation method, we need to compute (1) the Gauss-Legendre abscissas ζ_i, (2) weights ϖ_i, (3) radial collocation points r_i and (4) normalised mapped Legendre functions evaluated at the collocation points $\hat{P}_{L_n}^m(r_i)$. The normalisation procedure may require temporary multiple-precision arithmetic to handle large function values and factorials if one uses N larger than about 170. There have been several multi-precision arithmetic libraries available recently and we consider using the FM multiple-precision package (Smith, 2003). All essential computations ahead, however, can be performed under typical double-precision arithmetic.

It is noted that the number of the abscissas (or collocation points) N must be equal to or larger than the number of the basis elements M for the sake of proper transform between physical space $(f_m(r_1), \cdots, f_m(r_N))$ and spectral space $(\hat{f}_{|m|}^m, \cdots, \hat{f}_{|m|+M-1}^m)$. On the other hand, due to the even and odd parity of the associate Legendre functions, taking even N and M can reduce the work by half in the transform procedure (Matsushima & Marcus, 1997). Consequently, we set both N and M to be even and $N = M + 2$ in further analyses unless otherwise specified.

Finally, we discuss how to apply the mapped Legendre spectral collocation method to the present problem. Recalling (3.3.14) where $\mathbb{P}_{m\kappa}(\tilde{\boldsymbol{u}}) = (\tilde{\psi}, \tilde{\chi})$, we write

$$\tilde{\psi}(r; m, \kappa)e^{\mathrm{i}(m\phi+\kappa z)} = \sum_{n=|m|}^{|m|+M-1} \tilde{\psi}_n^{m\kappa} \hat{P}_{L_n}^m(r)e^{\mathrm{i}(m\phi+\kappa z)}, \tag{4.2.9}$$

$$\tilde{\chi}(r; m, \kappa)e^{\mathrm{i}(m\phi+\kappa z)} = \sum_{n=|m|}^{|m|+M-1} \tilde{\chi}_n^{m\kappa} \hat{P}_{L_n}^m(r)e^{\mathrm{i}(m\phi+\kappa z)}. \tag{4.2.10}$$

We point out that when $\tilde{\psi}$ is expressed in the partial sums above, it obeys the boundary conditions of an analytic scalar at the origin, i.e., as $r \to 0$,

$$\tilde{\psi}(r; m, \kappa) \to r^{|m|} \sum_{i=0}^{\infty} a_i^{m\kappa} r^{2i}, \tag{4.2.11}$$

where $a_0^{m\kappa}$, $a_1^{m\kappa}$, $\cdots$ are constants (see Eisen *et al.*, 1991; Matsushima & Marcus, 1995). Similar analyticity conditions are obeyed by $\tilde{\chi}(r; m, \kappa)$, and therefore the perturbation velocity field $\tilde{\boldsymbol{u}}(r)e^{\mathrm{i}(m\phi+\kappa z)}$ is also analytic at the origin (see Appendix B). Due to the properties of the mapped Legendre functions, the perturbation vorticity also decays as $r \to \infty$ (Matsushima & Marcus, 1997). As a consequence, $\mathbb{P}_{m\kappa}(\tilde{\boldsymbol{u}})$ can be uniquely represented by $2M$ spectral coefficients of $\tilde{\psi}_{|m|}^{m\kappa}$, $\cdots$, $\tilde{\psi}_{|m|+M-1}^{m\kappa}$ and $\tilde{\chi}_{|m|}^{m\kappa}$, $\cdots$, $\tilde{\chi}_{|m|+M-1}^{m\kappa}$. We may discretise the eigenvalue problem for viscous cases in (3.3.15) as

$$\sigma \begin{pmatrix} \tilde{\psi}_{|m|}^{m\kappa} \\ \vdots \\ \tilde{\psi}_{|m|+M-1}^{m\kappa} \\ \tilde{\chi}_{|m|}^{m\kappa} \\ \vdots \\ \tilde{\chi}_{|m|+M-1}^{m\kappa} \end{pmatrix} = \mathbf{L}_{m\kappa}^{\nu} \begin{pmatrix} \tilde{\psi}_{|m|}^{m\kappa} \\ \vdots \\ \tilde{\psi}_{|m|+M-1}^{m\kappa} \\ \tilde{\chi}_{|m|}^{m\kappa} \\ \vdots \\ \tilde{\chi}_{|m|+M-1}^{m\kappa} \end{pmatrix}, \tag{4.2.12}$$

where $\mathbf{L}_{m\kappa}^{\nu}$ is a $2M \times 2M$ complex matrix representing the linear operator $\mathcal{L}_{m\kappa}^{\nu}$. In a similar sense, we can define $\mathbf{L}_{m\kappa}^{0}$ representing $\mathcal{L}_{m\kappa}^{0}$ for the inviscid analysis and

$$\mathbf{L}_{m\kappa}^{\nu} = \mathbf{L}_{m\kappa}^{0} + Re^{-1}\mathbf{H}. \tag{4.2.13}$$

$\mathbf{H}$ is a matrix representation of the Laplacian $\nabla_{m\kappa}^2$ acting on the spectral coefficients $\tilde{\psi}_{|m|}^{m\kappa}$, $\cdots$, $\tilde{\psi}_{|m|+M-1}^{m\kappa}$ and $\tilde{\chi}_{|m|}^{m\kappa}$, $\cdots$, $\tilde{\chi}_{|m|+M-1}^{m\kappa}$, respectively. For a scalar function expanded by the mapped Legendre functions $a(r) = \sum_{n\geq|m|} a_n^m P_{L_n}^m(r)$, if we expand its Laplacian as $\nabla_{m\kappa}^2 a(r) = \sum_{n\geq|m|} b_n^m P_{L_n}^m(r)$, then the coefficients a_n^m and b_n^m constitute the following relationship for all $n \geq |m|$

$$\begin{aligned} b_n^m = &-\left[\frac{(n-|m|-1)(n-|m|)(n-2)(n-1)}{(2n-3)(2n-1)L^2}\right] a_{n-2}^m \\ &+\left[\frac{2n(n-|m|)(n-1)}{(2n-1)L^2}\right] a_{n-1}^m \\ &-\left[\frac{2n(n+1)(3n^2+3n-m^2-2)}{(2n-1)(2n+3)L^2} + \kappa^2\right] a_n^m \\ &+\left[\frac{2(n+1)(n+|m|+1)(n+2)}{(2n+3)L^2}\right] a_{n+1}^m \\ &-\left[\frac{(n+|m|+1)(n+|m|+2)(n+2)(n+3)}{(2n+3)(2n+5)L^2}\right] a_{n+2}^m, \end{aligned} \tag{4.2.14}$$

under the assumption that $a_n^m \equiv 0$ if n is less than $|m|$ (Matsushima & Marcus, 1997, p. 344). $\mathbf{H}$ can be formulated by (4.2.14).

The formulation of $\mathbf{L}_{m\kappa}^{0}$ involves the vector products in physical space and is conducted using a pseudospectral approach based on the Gauss-Legendre quadrature rule. Reconstructing $\tilde{\boldsymbol{u}}$ from $\mathbb{P}_{m\kappa}(\tilde{\boldsymbol{u}})$ via (3.3.1), we evaluate the vector products $\overline{\boldsymbol{U}} \times \tilde{\boldsymbol{\omega}}$ and $\overline{\boldsymbol{\omega}} \times \tilde{\boldsymbol{u}}$ at N radial collocation points and apply $\mathbb{P}_{m\kappa}$ again. As for the detailed algorithm including the numerical implementation of $\mathbb{P}_{m\kappa}$ as well as its inverse, refer to (69) and (70) in Matsushima and Marcus (1997), providing the spectral coefficients of $\mathbb{P}_{m\kappa}(\overline{\boldsymbol{U}} \times \tilde{\boldsymbol{\omega}})$ and $\mathbb{P}_{m\kappa}(\overline{\boldsymbol{\omega}} \times \tilde{\boldsymbol{u}})$. Integration in these equations can be performed numerically by the Gauss-Legendre quadrature rule, as given in (4.2.7). Following this procedure, we can compute the ith column vector of $\mathbf{L}^0_{m\kappa}$ by substituting the ith standard unit vector $\hat{\boldsymbol{e}}_i \in \mathbb{R}^{2M}$ for $(\tilde{\psi}^{m\kappa}_{|m|}, \cdots, \tilde{\psi}^{m\kappa}_{|m|+M-1}, \tilde{\chi}^{m\kappa}_{|m|}, \cdots, \tilde{\chi}^{m\kappa}_{|m|+M-1})$.

A global eigenvalue problem solver with the QR algorithm for non-Hermitian matrices, based on the LAPACK routine named ZGEEV, is used to solve the discretised eigenvalue problem. The procedure of constructing a global matrix and finding all eigenvalues has been established in previous studies, such as Fabre *et al.* (2006, p. 241). However, as shown in (4.2.12), our formulation directly results in the standard eigenvalue problem rather than the generalised form. Thus, it is sufficient to construct only one matrix of dimension $2M \times 2M$, with a reduction in the number of state variables from 4 to 2.

4.3 Numerical parameters and their effects

The mapped Legendre spectral collocation method comprises of three adjustable numerical parameters: M, N, and L. The first two parameters are commonly used in most spectral collocation methods, while the last parameter is unique to our method. This section elaborates on the impact of each parameter on the numerical method's performance and provides guidelines on their selection.

4.3.1 Number of spectral basis elements M

As shown in (4.2.1), M determines the number of basis elements in use and is the most important parameter for the numerical method's convergence. The larger the value of M, the closer the mapped Legendre series is to its ground-truth, as the full basis set assuming $M \to \infty$ is complete. If the function of interest is analytic and decays properly, the convergence is exponential with increasing M. Even if the function contains any singularity in the interior, the convergence must occur at infinite M, albeit slowly, as long as the function belongs to the Hilbert space $L^2(\mathbb{R}^+, w(r)dr)$.

For achieving better accuracy, it is always preferable to select a larger value of M. However, a too large value of M may cause the resulting matrix eigenvalue problem to be excessively large, leading to an increase in the time complexity in $(2M)^3$. In practice, the availability of computing resources should limit the maximum value of M.

4.3.2 Number of radial collocation points N

N, the number of the radial collocation points defined as (4.2.3), depends on M because $N \geq M$ needs to be satisfied. Increasing N nominally enhances the spatial resolution in physical space, thereby reducing numerical errors in the evaluation of vector products. However, this effect is rather marginal, as most of the major computations and errors occur in spectral space. Moreover, if an increase in N does not accompany an increase in M by the same or nearly the same amount, it may have no benefit at all. One may consider the extreme case where $N \to \infty$ while M is kept constant at unity. Regardless of how perfect the radial resolution is, none of the functions can be handled except for a scalar multiple of the first basis element $P^m_{L_{|m|}}(r)$.

Therefore, it is better to consider N dependent on M, and any change in N should only be followed by a change in M. This justifies why we use $N = M + 2$. Similarly, an improvement in the spatial resolution by N should imply the use of a larger M. Henceforth, N is usually omitted when we state the numerical parameters, and M implicitly specifies N as $M+2$. In this case, we note that the resolution parameter Δ in (4.2.4) equals $2L/(M+2)$.

4.3.3 Map parameter for Legendre functions L

The map parameter L provides an additional level of computational freedom that distinguishes the present numerical method from others. We highlight three significant roles of this parameter, two of which are related to spatial resolution in physical space and the other to basis change in spectral space.

In physical space, when M (and N) is fixed, a change in L results in two anticomplementary effects with respect to spatial resolution, as shown in figure 4.1. When L increases, the high-resolution region $0 \leq r < L$, where half of the collocation points are clustered, expands, which has a positive effect. However, it negatively impacts the resolution, especially in the high-resolution region, where Δ increases with L. Increasing $N = M + 2$ may compensate for the loss in resolution. However, if M is already at a practical limit due to the computing budget, expanding the high-resolution region by increasing L should stop when Δ remains satisfactorily small. The requirement for satisfaction should be specific to the eigenmodes to be resolved, which will be discussed in each analysis section later. Similar discussions can be made in the opposite direction when decreasing L.

In spectral space, changing L entirely replaces the complete basis function set. For instance, when $L = A$ and $L = B$, the spectral method can be constructed on either of two different complete basis sets, i.e., $\{P^m_{A_{|m|}},\ P^m_{A_{|m|+1}}\ \cdots\}$ or $\{P^m_{B_{|m|}},\ P^m_{B_{|m|+1}},\ \cdots\}$. Since orthogonality among the basis functions does not necessarily hold across the basis sets, an eigenmode found with $L = A$ can differ from that found with $L = B$. If B differs from A by an infinitesimal amount, our method makes it possible to find eigenmodes that continuously vary if they exist. This was thought to be hardly achievable via classic eigenvalue solvers due to discretisation (cf. Mao & Sherwin, 2011, p. 11). Once the numerical method's convergence is secured by sufficiently large M and N, we explore such non-normal eigenmodes that vary continuously by fine-tuning L.

4.4 Validation

To confirm the numerical validity of our method, we compared some eigenvalues from the discrete branch of the spectra with those previously calculated by Mayer and Powell (1992). They also used a spectral collocation method but with Chebyshev polynomials as radial basis

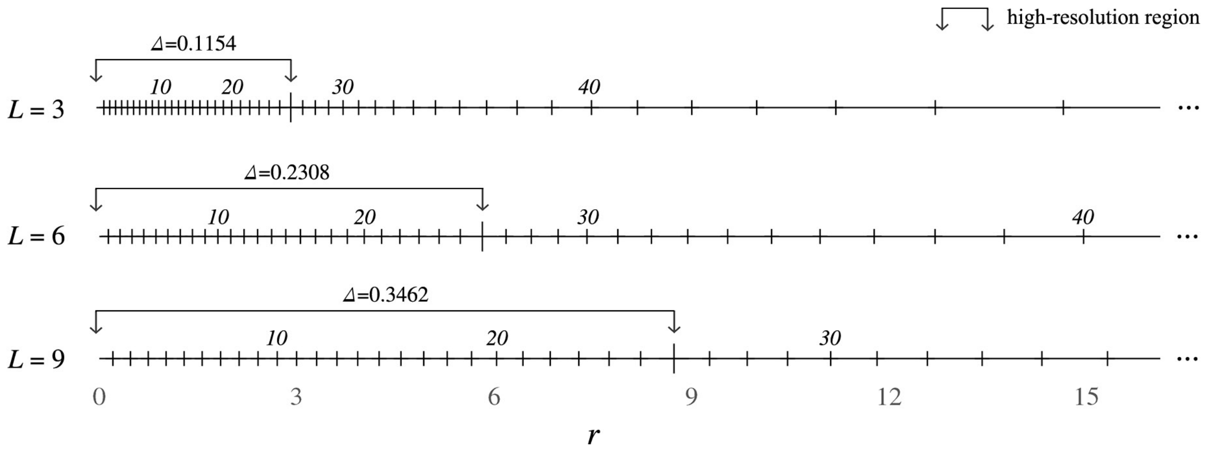

Figure 4.1: Changes in distribution of the collocation points with respect to L given $N = 52$. Some collocation points at large radii are omitted. The high-resolution region is $0 \leq r < L$, where half of the collocation points are clustered around the origin. As L increases, the high-resolution region is expanded. However, the mean spacing Δ grows simultaneously. L should be chosen carefully to balance these anti-complementary effects.

functions over an artificially truncated radial domain, rather than the mapped Legendre basis functions over an unbounded radial domain we use. For comparison, we linearly scaled the eigenvalues reported in Mayer and Powell (1992) to match the q-vortex model used in our study because the azimuthal velocity component is scaled by q in their study, whereas we adjust the axial velocity component.

We compared the most unstable eigenvalue calculations for the inviscid case $m = 1$, $\kappa = 0.5$, $q = -0.5$ (or equivalently $m = 1$, $\kappa = -0.5$, $q = 0.5$) and the viscous case $m = 0$, $\kappa = 0.5$, $q = 1$, $Re = 10^4$ in table 4.1. We conducted the calculations using three different numbers of basis elements M (20, 40, and 80) and three different map parameters L (8, 4, and 2). Our results show that the trend towards convergence is apparent as M increases and L decreases. As we discuss in terms of the characteristic resolution parameter Δ defined in (4.2.4), both parameters influence the numerical resolution. Increasing M leads to an increase in the number of radial collocation points N, while decreasing L improves spatial resolution by filling the inner high-resolution region ($0 \leq r < L$) with more collocation points (see figure 4.1). However, this comes at the expense of reducing the range of the high-resolution region and effectively shrinking the radial domain by placing the collocation point with the largest radius at $r_N = L\sqrt{(1 + \zeta_N)/(1 - \zeta_N)}$, which can lead to inaccuracies if any significant portion of the solution exists either in the outer low-resolution region or outside the effective limit. The convergence test of $\sigma^{\dagger}_{\text{viscous}}$ with $M = 20$ in table 4.1 partially demonstrates this concern. When we compare the eigenvalues computed with $L = 4$ and $L = 2$, the latter shows no clear improvement in convergence compared to the former, despite having a smaller L. Even small L causes the eigenvalue's real part to move further away from the reference value of Mayer and Powell (1992). Therefore, we must keep in mind that blindly pursuing small L does not guarantee better convergence, although using large M is

	M	L	$\sigma^{\dagger}_{\text{inviscid}}$	$\sigma^{\dagger}_{\text{viscous}}$
Present study	20	8	0.37755989 + 0.112913723i	0.00011969 + 0.01679606i
	20	4	0.40527381 + 0.099406043i	0.00018939 + 0.01658207i
	20	2	0.40525621 + 0.099437298i	0.00014902 + 0.01656308i
	40	8	0.40522876 + 0.099370546i	0.00017892 + 0.01632424i
	40	4	0.40525620 + 0.099437300i	0.00018406 + 0.01640824i
	40	2	0.40525620 + 0.099437300i	0.00018463 + 0.01640723i
	80	8	0.40525620 + 0.099437300i	0.00018478 + 0.01640740i
	80	4	0.40525620 + 0.099437300i	0.00018469 + 0.01640717i
	80	2	0.40525620 + 0.099437300i	0.00018469 + 0.01640717i
M & P (1992)	–	–	0.40525620 + 0.099437300i	0.00018469 + 0.01640717i

Table 4.1: Comparison of the eigenvalues associated with the most unstable mode (indicated with a superscript †) for the inviscid case with $m = 1$, $\kappa = 0.5$, $q = -0.5$ and for the viscous case with $m = 0$, $\kappa = 0.5$, $q = 1$, $Re = 10^4$. The table illustrates how the values change when we alter the map parameter L and the number of radial mapped Legendre basis functions M. The last row displays the values obtained by Mayer and Powell (1992), who employed up to 200 radial Chebyshev basis functions. Their published eigenvalues were appropriately rescaled to fit the q-vortex model employed in our study. Our numerically computed eigenvalues tend towards a fixed point as we increase M beyond 40. It should be noted that the size of the matrix eigenvalue problem system is $2M$ for our method and $3M$ for that of Mayer and Powell (1992). Thus, even when using the same M, our method is expected to require $(2/3)^3$ less work than theirs.

always favoured for numerical convergence.

The high-resolution range of the present method, represented by L, should not match the domain truncation radius in the method of Mayer and Powell (1992). Adjusting the high-resolution range through L has no impact on the unbounded nature of the domain and can be customised essentially. However, altering the domain truncation radius fundamentally harms the unbounded nature of the domain and must be set to its maximum computing limit. On the other hand, we achieve the same accuracy as Mayer and Powell (1992) with roughly three times smaller M, which supports the numerical efficiency of our method. Presumably, our method is around ten times more computationally efficient in solving matrix eigenvalue problems that scale as $O(M^3)$. We believe this is mainly because their simple algebraic mapping of Chebyshev collocation points (see Ash & Khorrami, 1995, p. 357) clusters approximately one-third of the collocation points near the artificial outer radial boundary, where vortex motion is near zero and not important by assumption. Such collocation points do not significantly contribute to solving the problem, resulting in an inefficient use of numerical resources.

Note that the eigenmodes shown here are regular and have no singularities, as depicted in figure 4.2. Such regular eigenmodes are expanded by a finite number of radial basis elements that are already regular, and as shown in table 4.1, their numerical results converge expo-

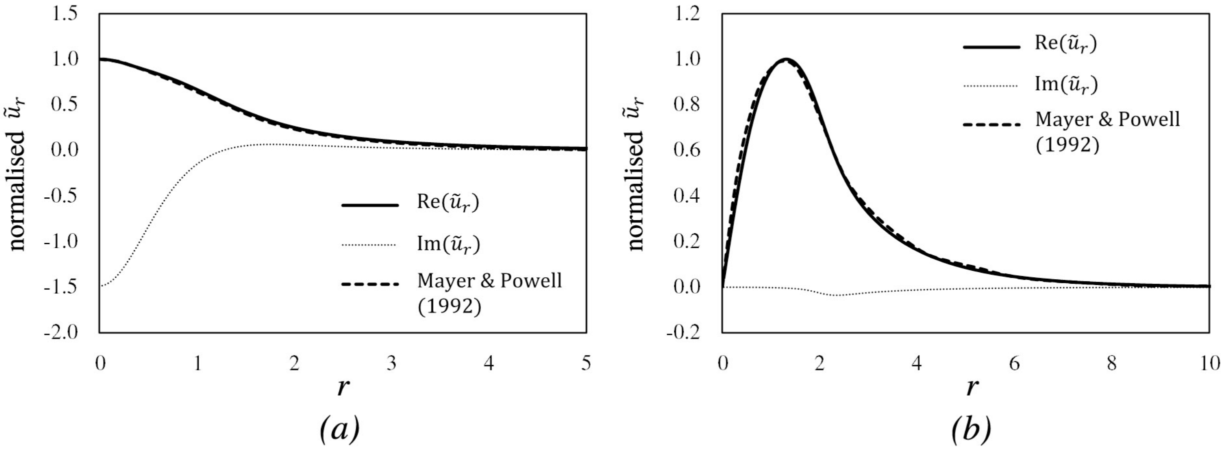

Figure 4.2: A comparison of our numerical calculation with that of Mayer and Powell (1992). Shown is the radial velocity component of the most unstable eigenmode for the validation cases (*a*) $(m, \kappa, q, Re) = (1, 0.5, -0.5, \infty)$ and (*b*) $(m, \kappa, q, Re) = (0, 0.5, 1, 10^4)$, where the maximum of $\mathrm{Re}(\tilde{u}_r)$ is normalised to unity. Numerical parameters are $M = 80$ and $L = 2$. Note that Mayer and Powell (1992) only plotted the real parts of the eigenmodes.

nentially with increasing M. However, singular eigenmodes can only be expressed exactly when an infinite sum of mapped Legendre functions is taken (see Gottlieb & Orszag, 1977). Nonetheless, as stated in the preliminary remarks, we are essentially interested in physical eigenmodes, i.e., those without singularities and computed numerically with small spectral residual error. The current validation is strong enough to underpin this objective. Later in this research (see §7.1.4), we present some eigenmodes that have convincing signatures of viscous remnants after regularising the inviscid critical-layer singularities. These singularities become regularised but still nearly singular regions of local rapid oscillations. We can find the value of M at which these eigenmodes are spatially resolved, even if it typically goes beyond 80. Also note that in this respect, we only peripherally examine their inviscid counterparts with the critical-layer singularities using our numerical method (see §6.1.2).

Chapter 5

Spectrum

Solving an eigenvalue problem $\lambda \boldsymbol{x} = \boldsymbol{\mathcal{L}} \boldsymbol{x}$ is often equivalent to finding the spectrum of the linear operator $\boldsymbol{\mathcal{L}}$, denoted $\sigma(\boldsymbol{\mathcal{L}})$. A number of previous studies that investigated a linearised version of the Navier-Stokes equations, epitomised by the Orr-Sommerfeld equation, have already adopted the term "spectra" (Grosch & Salwen, 1978; Jacobs & Durbin, 1998) to account for eigenmodes of the linearised equations. In our study, we also employ this concept to characterise eigenmode families found in the linear analysis of the q-vortex. We first state the definition of the spectrum for the reader's convenience.

Definition 1 *Given that a bounded linear operator $\boldsymbol{\mathcal{L}}$ operates on a Banach space $\mathcal{X}$ over $\mathbb{C}$, $\sigma(\boldsymbol{\mathcal{L}})$ consists of all scalars $\lambda \in \mathbb{C}$ such that the operator $(\boldsymbol{\mathcal{L}} - \lambda)$ is not bijective and thus $(\boldsymbol{\mathcal{L}} - \lambda)^{-1}$ is not well-defined.*

If a complex scalar λ is an eigenvalue of $\boldsymbol{\mathcal{L}}$, then it belongs to $\sigma(\boldsymbol{\mathcal{L}})$; however, the inverse statement is generally not true. This is because, by definition, the spectrum of $\boldsymbol{\mathcal{L}}$ includes not only a type of λ that makes $(\boldsymbol{\mathcal{L}} - \lambda)$ non-injective but also another type of λ by which $(\boldsymbol{\mathcal{L}} - \lambda)$ is injective but not surjective. The former ensures the presence of a non-trivial eigenmode in $\mathcal{X}$, which therefore comprises the set of ordinary eigenvalues, while the latter does not. However, if $(\boldsymbol{\mathcal{L}} - \lambda)$ has a dense range, λ can be an *approximate* eigenvalue in the sense that there exists an infinite sequence $(\boldsymbol{e}_j \in \mathcal{X} \setminus \{\boldsymbol{0}\})$ for which

$$\lim_{j \to \infty} \| \boldsymbol{\mathcal{L}} \boldsymbol{e}_j - \lambda \boldsymbol{e}_j \| = 0. \tag{5.1}$$

In our method, $\boldsymbol{e}_j$ and $\mathcal{X}$ can be taken as a mapped Legendre series of the first j basis elements in (4.2.1) and the Hilbert space, respectively. Even if the sequence limit $\boldsymbol{e}_\infty$ does not belong to $\mathcal{X}$, it can still be regarded as an eigenmode solution in a *rigged* manner, by permitting discontinuities, singular derivatives, or non-normalisabilities (i.e., rigged Hilbert space). In the literature related to fluid dynamics, both ordinary and approximate cases are considered as eigenvalues. They are classified either as discrete in the complex σ-plane, or as continuous in association with the eigenmodes possessing singularities. Despite their singular behaviour, understanding eigenmodes associated with continuous spectra may be important

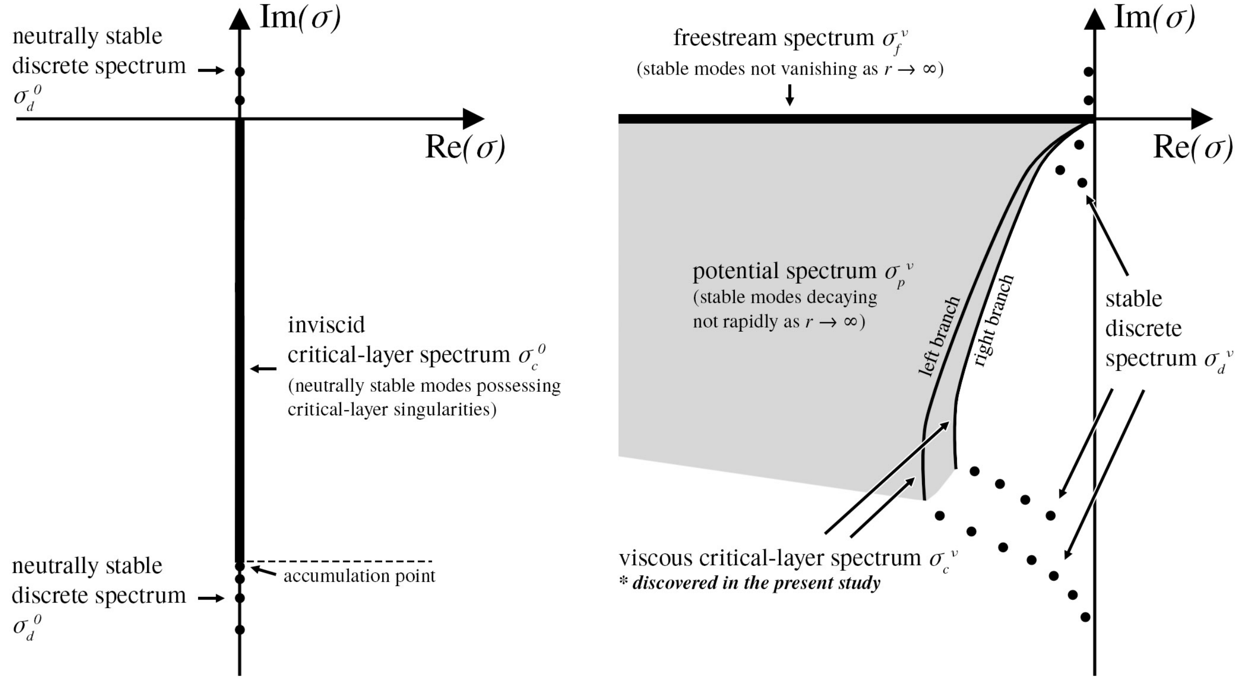

(a) Inviscid spectra *(b)* Viscous spectra

Figure 5.1: Schematic diagrams of the spectra of the eigenvalues of a q-vortex of (a) $\mathcal{L}^0_{m\kappa}$ for inviscid problems where $\nu \equiv 0$ (see Mayer & Powell, 1992; Heaton, 2007a; Gallay & Smets, 2020) and (b) $\mathcal{L}^\nu_{m\kappa}$ for viscous problems with finite Re, including $\nu \to 0^+$ (see Fabre *et al.*, 2006; Mao & Sherwin, 2011). Each schematic exhibits a set of eigenvalues where m and κ are fixed. The cases illustrated here assume $m > 0$. These spectra are shown here because they are representative, but they do not embrace all of the different families of spectra. The labels attached here are used throughout the main body of the text. Note that figures of the true numerical spectra computed by us, rather than schematics, follow in §6 and §7, and that the viscous critical-layer spectrum, consisting of *two* distinct curves in (b), were discovered via the present numerical analysis and were not previously identified.

because they contribute to a complete basis for expressing an arbitrary perturbation (Case, 1960; Fabre *et al.*, 2006; Roy & Subramanian, 2014).

In figure 5.1, schematic diagrams of the spectra in relation to the q-vortices are presented. These illustrations assume that m is positive. The exact spectra differ depending on the values of m, κ, q, Re, and the symmetries which are explained next. Some families of the spectra are not displayed because they are not within the main scope of this study. For instance, in the inviscid spectra, the unstable discrete spectrum and its symmetric stable counterpart frequently appear for some m, κ, and q. However, they vanish as q becomes sufficiently large (e.g., $|q| > 2.31$) (see Heaton, 2007a). For the Lamb-Oseen vortex where $q \to \infty$, it was analytically proven that all of the eigenvalues are located on the imaginary axis, irrespective of m and κ, indicating that all eigenmodes must be neutrally stable (see Gallay & Smets, 2020).

There are three notable space-time symmetries in this eigenvalue problem. First, because the linearised equations admit real solutions for the velocity/pressure eigenmodes, regardless of the values of q and the viscosity (including the case $\nu \equiv 0$), if $(\tilde{u}_r, \tilde{u}_\phi, \tilde{u}_z, \tilde{p})$ and σ are an eigenmode and eigenvalue with wavenumbers (m, κ), then $(\tilde{u}_r^*, \tilde{u}_\phi^*, \tilde{u}_z^*, \tilde{p}^*)$ is also an eigenmode with eigenvalue σ^* and with $(-m, -\kappa)$. Next, for the inviscid case, with any value of q, the linearised equations are time-reversible, and as a consequence if $(\tilde{u}_r, \tilde{u}_\phi, \tilde{u}_z, \tilde{p})$ and σ are a velocity/pressure eigenmode and eigenvalue with wavenumbers (m, κ), then $(\tilde{u}_r^*, -\tilde{u}_\phi^*, -\tilde{u}_z^*, -\tilde{p}^*)$ is also an eigenmode with eigenvalue $-\sigma^*$ and with the same (m, κ). This symmetry makes the spectra symmetric about the imaginary axis in the left panel of figure 5.1 but not in the right panel. Third, for the inviscid case with any value of q, we could combine the two symmetries above and obtain the fact that if $(\tilde{u}_r, \tilde{u}_\phi, \tilde{u}_z, \tilde{p})$ and σ are a velocity/pressure eigenmode and eigenvalue with wavenumber (m, κ), then $(\tilde{u}_r, -\tilde{u}_\phi, -\tilde{u}_z, -\tilde{p})$ is also an eigenmode with eigenvalue $-\sigma$ with wavenumbers $(-m, -\kappa)$.

In particular, for the inviscid case with $q \to \infty$ (i.e., with $\bar{U}_z = 0$), the linearised equations are also invariant under $z \to -z$. In this case, if $(\tilde{u}_r, \tilde{u}_\phi, \tilde{u}_z, \tilde{p})$ and σ are a velocity/pressure eigenmode and eigenvalue with wavenumbers (m, κ), then $(\tilde{u}_r, \tilde{u}_\phi, -\tilde{u}_z, \tilde{p})$ is also an eigenmode with eigenvalue σ and with wavenumbers $(m, -\kappa)$. This symmetry can be combined with either or both of the two earlier listed symmetries to produce additional, but not independent symmetries; for example, if $(\tilde{u}_r, \tilde{u}_\phi, \tilde{u}_z, \tilde{p})$ and σ are a velocity/pressure eigenmode and eigenvalue with wavenumbers (m, κ), then $(\tilde{u}_r^*, -\tilde{u}_\phi^*, \tilde{u}_z^*, -\tilde{p}^*)$ is also an eigenmode with eigenvalue $-\sigma^*$ and with $(m, -\kappa)$.

Based on the two-dimensional Orr-Sommerfeld equation, Lin (1961) argued that the spectra of eigenmodes of viscous flows are discrete. However, for unbounded viscous flows, Drazin and Reid (2004, pp. 156-157) stated that this is incorrect, and there is a continuous spectrum associated with eigenmodes that vary sinusoidally in the far field instead of vanishing. The presence of continuous spectra associated with the q-vortices due to spatial unboundedness was also discussed by Fabre *et al.* (2006) and Mao and Sherwin (2011). One example of the continuous spectrum is the viscous *freestream* spectrum, named by Mao and Sherwin (2011) and denoted σ_f^ν here, which is located on the left half of the real axis in the complex σ-plane in figure 5.1(b). However, the eigenmodes in this spectrum persist rather than go to zero as $r \to \infty$. As stated in §2.3, we are only interested in eigenmodes that we classify as physical. We have defined eigenmodes in which the velocity and vorticity do not decay harmonically at radial infinity as non-physical. Since our numerical method was specifically designed not to deal with such non-physical eigenmodes, we do not discuss them further in this research and clarify that our method is not the tool for those who wish to investigate σ_f^ν. We remark that Bölle *et al.* (2021) argued that the viscous freestream spectrum is rather an "artefact" of the mathematical model of an unbounded domain. With the exception of the viscous *freestream* eigenmodes, our numerical method is capable of computing the families of eigenvalues and eigenmodes indicated in figure 5.1.

For the inviscid and viscous discrete spectra, denoted σ_d^0 and σ_d^ν, respectively, the unstable eigenmodes of the q-vortices with finite q have been extensively studied (Leibovich & Stewartson, 1983; Mayer & Powell, 1992), particularly for small q (Lessen *et al.*, 1974; Heaton, 2007a). However, it is unclear whether these instabilities would be significant for aeronautical applications that are known to have large q (≈ 4) (see Fabre & Jacquin, 2004, pp. 258-259). As the discrete spectra and related instabilities, which have been well-studied, are not the main focus of the present study, the unstable branches in σ_d^0 and σ_d^ν, which may be detectable for small q and large Re, are omitted in figure 5.1.

Instead, we pay attention to the eigenmodes associated with the inviscid critical-layer spectrum, denoted σ_c^0, which has been known to be related to further transient growth of wake vortices (Heaton & Peake, 2007; Mao & Sherwin, 2012). For the inviscid q-vortex σ_c^0 is determined as a subset of $\sigma(\mathcal{L}_{m\kappa}^0)$, which is

$$\sigma_c^0 = \left\{ \sigma_c \in \mathrm{i}\mathbb{R} \;\middle|\; \exists r_c \in (0,\infty) \quad -\mathrm{i}\sigma_c + \frac{m(1-e^{-r_c^2})}{r_c^2} + \frac{\kappa e^{-r_c^2}}{q} = 0 \right\} \subset \sigma\left(\mathcal{L}_{m\kappa}^0\right). \tag{5.2}$$

When $q \to \infty$, (5.2) reduces to the expression given in Gallay and Smets (2020), which applies to the Lamb-Oseen vortex case. Considering the fact that σ_c^0 is due to an inviscid singularity (Le Dizès, 2004), we deduce the expression in (5.2) through the following steps. The singularity can be straightforwardly identified by further reducing the governing equations, as shown in Mayer and Powell (1992, p. 94), originally done by Howard and Gupta (1962). Breaking the eigenvalue problem form in (3.1.9) and (3.1.10) and performing further reduction, we obtain the following second-order differential equation:

$$\gamma^2 \frac{d}{dr}\left(\frac{r}{\kappa^2 r^2 + m^2}\frac{d(r\tilde{u}_r)}{dr}\right) - \left(\gamma^2 + a\gamma + b\right)\tilde{u}_r = 0, \tag{5.3}$$

where

$$\gamma \equiv -\mathrm{i}\sigma + \frac{m\overline{U}_\phi(r)}{r} + \kappa \overline{U}_z(r), \tag{5.4}$$

$$a \equiv r\frac{d}{dr}\left[\frac{r}{\kappa^2 r^2 + m^2}\left(\frac{d\gamma}{dr} + \frac{2m\overline{U}_\phi(r)}{r^2}\right)\right], \tag{5.5}$$

$$b \equiv \frac{2\kappa m \overline{U}_\phi(r)}{\kappa^2 r^2 + m^2}\left(\frac{d\overline{U}_z}{dr} - \frac{\kappa}{m}\frac{d(r\overline{U}_\phi)}{dr}\right). \tag{5.6}$$

The equation becomes singular when $\gamma = 0$, which is feasible when there exist $\sigma_c \in \mathrm{i}\mathbb{R}$ and $r_c \in (0,\infty)$ such that

$$-\mathrm{i}\sigma_c + \frac{m\overline{U}_\phi(r_c)}{r_c} + \kappa\overline{U}_z(r_c) = 0, \tag{5.7}$$

or equivalently,

$$\mathrm{Re}(\sigma_c) = 0, \quad \mathrm{Im}(\sigma_c) = -\frac{m\overline{U}_\phi(r_c)}{r_c} - \kappa\overline{U}_z(r_c). \tag{5.8}$$

Substituting the q-vortex velocity profile into (5.7) shows the relationship between the imaginary eigenvalue σ_c^0 and the radial location r_c of the critical layer:

$$\sigma_c = -\mathrm{i}\left[\frac{m(1-e^{-r_c^2})}{r_c^2} + \frac{\kappa e^{-r_c^2}}{q}\right], \tag{5.9}$$

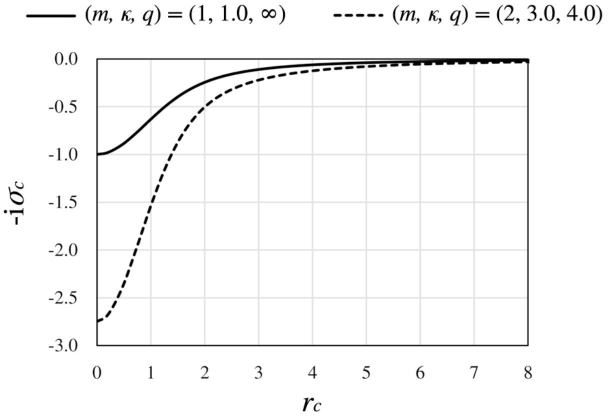

Figure 5.2: Critical-layer singularity radial location r_c versus critical layer eigenvalue σ_c with fixed m, κ and q. See (5.9) and (5.10). The two illustrated cases where $(m, \kappa, q) = (1, 1.0, \infty)$ and $(m, \kappa, q) = (2, 3.0, 4.0)$ are investigated in later analyses.

and for the Lamb-Oseen vortex with $1/q \equiv 0$

$$\sigma_c = -\mathrm{i}\left[\frac{m(1-e^{-r_c^2})}{r_c^2}\right]. \tag{5.10}$$

For every eigenmode associated with σ_c, it must contain at least one singularity at $r = r_c$, which is what we have been referring to as a critical-layer singularity. As a result, the continuum of eigenvalues on the imaginary axis forms σ_c^0, as depicted in figure 5.1(a). For the q-vortices with positive m, κ, and q (including $q \to \infty$), which we will consider in later analyses, the supremum of $-\mathrm{i}\sigma_c$ is 0 (as $r_c \to \infty$) and the infimum of $-\mathrm{i}\sigma_c$ is $-m - \kappa/q$ (as $r_c \to 0$). Also in this case, there is a one-to-one correspondence between σ_c and r_c as $m(1 - e^{-r^2})/r^2 + (\kappa/q)e^{-r^2}$ is monotonic with respect to r (see figure 5.2).

On the other hand, viscosity regularises the critical-layer singularities of the eigenmodes of q-vortices. It is of physical importance to identify how viscosity transforms inviscid spectra, such as σ_c^0, into a subset of the viscous spectra $\sigma(\mathcal{L}_{m\kappa}^{\nu})$ and to determine which branches of σ_c^0 vanish and what new eigenmodes are created. According to Heaton (2007a), for non-zero viscosity, σ_c^0 is replaced by a large number of closely packed discrete eigenmodes, but a detailed explanation was not given. Numerical observations by Bölle *et al.* (2021) identified randomly scattered eigenvalues in the shaded region in figure 5.1(b), suggesting that they are the viscous remnants of σ_c^0. Mao and Sherwin (2011), who earlier discovered this region, named it the *potential* spectrum, denoted σ_p^{ν}, and suggested that it could be continuous based on the shape of the surrounding pseudospectra. The (ε-)pseudospectrum is defined as follows (Trefethen & Embree, 2005).

Definition 2 *Let* $R(z; \mathcal{L}) \equiv (\mathcal{L} - z)^{-1}$ *be the resolvent of* $\mathcal{L}$ *at* $z \in \mathbb{C} \setminus \sigma(\mathcal{L})$*. For* $\varepsilon > 0$*, the*

ε-pseudospectrum, denoted $\sigma_\varepsilon(\mathcal{L})$, is the set

$$\sigma_\varepsilon(\mathcal{L}) \equiv \left\{ z \in \mathbb{C} \,\middle|\, \|R(z;\mathcal{L})\| > \frac{1}{\varepsilon} \right\}. \tag{5.11}$$

Note that the lower bound of the resolvent norm is determined by the inequality

$$\|R(z;\mathcal{L})\| \geq \sup_{\mu \in \sigma(\mathcal{L})} \frac{1}{|z-\mu|}, \tag{5.12}$$

where equality holds if the resolvent is normal (Bölle *et al.*, 2021, pp. 9-10). For discrete eigenvalues, when ε is sufficiently small, the ε-pseudospectrum is formed by an open disk that surrounds the eigenvalue. However, when it comes to continuous spectra, Mao and Sherwin (2011) pointed out that as ε approaches zero, the ε-pseudospectrum tends to cover the entire region in the complex σ-plane that is equivalent to σ_p^ν, as shown in figure 5.1(b). They proposed that this region comprises entirely of the viscous continuous spectra together with σ_f^ν, which is located on the negative real axis. Such an asymptotic topology of pseudospectra implies the presence of continuous spectra in this region.

Although this argument appears reasonable, it requires careful examination for the following reasons. Firstly, as we numerically solve the eigenvalue problem, solutions that do not exhibit convergence may result from spurious modes due to discretisation. While randomly scattered eigenvalues may be true examples of eigenmodes within the continuous spectrum, they can also be spurious eigenmodes created by the disretised approximation of $\mathcal{L}_{m\kappa}^\nu$. Secondly, describing the pseudospectra of $\mathcal{L}_{m\kappa}^\nu$ as proximity to the spectrum is valid only if $R(z;\mathcal{L}_{m\kappa})$ is normal and the equality in (5.12) holds. According to Bölle *et al.* (2021), the resolvent is selectively non-normal in a frequency band where σ_p^ν is located, meaning that $R(z;\mathcal{L}_{m\kappa})$ can take a large value even if z is not actually close to $\sigma(\mathcal{L}_{m\kappa})$. Lastly, for the sake of rigour, the shape of the potential spectrum, as depicted in the schematic in figure 5.1(b), should be considered suggestive. This is because, to the best of our knowledge, its presence has only been numerically proposed in the discretised problem with increasing M (i.e., $\mathbf{L}_{m\kappa}^\nu$), but has not been analytically verified in the original problem (i.e., $\mathcal{L}_{m\kappa}^\nu$). It should be noted that in the present study, we premise the analytic presence of the potential spectrum as depicted in figure 5.1(b), so that numerical eigenvalues found on the ε-pseudospectrum of $\mathbf{L}_{m\kappa}^\nu$ in the limit of $\varepsilon \to 0$ with a sufficiently large value of M can be considered the discretised representation of this analytic entity, and therefore non-spurious.

Although σ_p^ν is known to be associated with stable eigenmodes that decay to zero as $r \to \infty$, their decay rates in r have been reported to be much slower than the exponential decay rates of the discrete eigenmodes (Mao & Sherwin, 2011). In the following section, we will show that the decay behaviours of the inviscid critical-layer eigenmodes are comparable to those of the discrete eigenmodes. Therefore, we cast doubt on whether σ_p^ν accurately represents the viscous remnants of σ_c^0 that result from the viscous regularisation of the critical layers. If there exist spectra associated with eigenmodes that possess not only regularised critical-layer structures due to viscosity but also exhibit radial decay behaviours similar to those seen in the inviscid critical-layer eigenmodes, it would be accurate to refer to them as the *true* viscous remnants of σ_c^0. We propose to distinguish these spectra and call them the "viscous critical-layer spectrum," denoted σ_c^ν. Using the present numerical method, we will demonstrate that σ_c^ν is formed by two distinct curves near the right end of σ_p^ν, as depicted in figure 5.1(b).

Chapter 6

Inviscid linear analysis

The eigenvalue problem $\sigma\,[\mathbb{P}_{m\kappa}(\tilde{\boldsymbol{u}})] = \mathcal{L}^0_{m\kappa}\,[\mathbb{P}_{m\kappa}(\tilde{\boldsymbol{u}})]$ is analysed by finding the spectra of the discretised operator $\mathsf{L}^0_{m\kappa}$ and their associated eigenmodes. Since the number of spatially resolved *discrete* eigenmodes is typically far less than M due to the spatial resolution limit, the majority of numerical eigenmodes should be associated with the *continuous* critical-layer spectrum σ^0_c. Although σ^0_c is associated with neutrally stable eigenmodes, its numerical counterpart often creates a "cloud" of incorrect eigenvalues clustered around the true location of σ^0_c, as observed by Mayer and Powell (1992), Fabre and Jacquin (2004), and Heaton (2007a). However, the previous studies that observed this incorrect spectrum paid less attention to its correction, which is our major interest, as they were primarily interested in discrete unstable modes that can be resolved out of (and thus are sufficiently far from) the cloud. When discrete unstable eigenmodes are present for small q, the most unstable one prevails in the linear instability of the q-vortex. Therefore, the presence of these incorrect eigenmodes may not be problematic.

On the other hand, for large q (typically, $|q| > 1.5$ according to Lessen *et al.* (1974), or $|q| > 2.31$ according to Heaton (2007a), depending on the parameter values of m and κ) where the inviscid q-vortex is linearly neutrally stable and the eigenmodes are located on $\mathrm{i}\mathbb{R}$ of the complex σ-plane. Although the flow is analytically neutrally stable, incorrect eigenmodes may appear in association with eigenvalues clustered around the imaginary axis, leading to the incorrect conclusion that the flow is linearly unstable because some of the eigenvalues lie in the right half of the complex σ-plane ($\mathrm{Re}(\sigma) > 0$). We focus our attention on the analysis of large or infinite q cases as any unstable eigenmodes occurring in the analysis are incorrect. In what follows, we demonstrate that these incorrect eigenmodes are *under-resolved* eigenmodes of the inviscid critical-layer eigenmodes and can be corrected by adjusting the numerical parameters so that they correctly exhibit their neutrally stable nature ($\mathrm{Re}(\sigma) = 0$) in our numerical analysis.

6.1 Numerical spectra and eigenmodes

In figure 6.1, we present the eigenvalues of two inviscid vortices: the Lamb-Oseen vortex with $(m, \kappa, q) = (1, 1.0, \infty)$ and the strong swirling Batchelor vortex with $(m, \kappa, q) = (2, 3.0, 4.0)$. By comparing these two vortices, we demonstrate their common properties and extract features that can be generalised to vortices with large q and moderate m and κ of order unity, which are thought to be relevant for practical aeronautical applications (see Fabre & Jacquin, 2004, pp. 258-259). To observe the effect of the numerical parameter M, we computed each vortex in four ways: with $M = 100,\ 200,\ 300$, and 400. Analytically, every eigenvalue is expected to lie on $\mathrm{i}\mathbb{R}$. The shaded area in each plot is the non-normal region of the spectra, indicating the frequency band that includes the analytic range of σ_c^0.

Clearly, all these *numerical* spectra contain some eigenvalues that are incorrect (i.e, not on the imaginary axis). We can observe three families of numerical eigenvalues. A discrete family $(+)$ corresponds to σ_d^0, where the eigenvalues are discrete and located outside the shaded area. An inviscid critical-layer family $(\bullet)$ corresponds to σ_c^0. Its eigenvalues lie on the imaginary axis, are within the shaded area, and the number of them increases as M increases. Finally, a family of under-resolved eigenvalues $(\times)$, which, had they been spatially well-resolved, would have been eigenvalues belonging to σ_c^0 and lie on the imaginary axis. Instead, these eigenvalues lie off the imaginary axis and within the shaded area. These under-resolved eigenvalues are characterised by non-zero real parts with absolute values typically greater than 10^{-10} as a result of numerical discretisation errors. The eigenvalues form clouds of structures that are symmetric about the imaginary axis. The cloud structures are due to insufficient spatial resolution, and the absolute values of the real parts of the eigenvalues tend to increase as the value of q decreases. As M increases, the absolute values of the real parts of the eigenvalues tend to decrease, and the cloud of eigenvalues gets "squeezed" to the imaginary axis, which is similar to the "squeeze" observed by Mayer and Powell (1992) when they increased the number of Chebyshev basis elements in their spectral method calculation.

6.1.1 Discrete eigenmodes

Although σ_d^0 and the discrete eigenmodes are not the main focus of this research, it is worthwhile to confirm their convergence properties. Figure 6.1 shows that the discrete eigenmodes associated with eigenvalues away from the accumulation points (see Gallay & Smets, 2020, pp. 14-16) (i.e., intersections of the imaginary axis with the lower boundary of the shaded regions in figure 6.1) are spatially resolved for $M \geq 100$, $L = 6$, and $N = M + 2$. For these values of L, M, and N, each eigenvalue approaches a fixed point as M increases. The discrete eigenmodes are distinguishable from each other by their radial structures and, in particular, by the number of "wiggles" (intervals between two neighboring zeroes) as a function of radius. Typically, the eigenmodes with eigenvalues farthest from the accumulation points have the fewest wiggles, as shown in figure 6.2. The discrete eigenmodes have an increasing number of wiggles as the eigenvalue approaches the accumulation point, forming a countably infinite, linearly independent set in the eigenspace of $\mathcal{L}_{m\kappa}^0$.

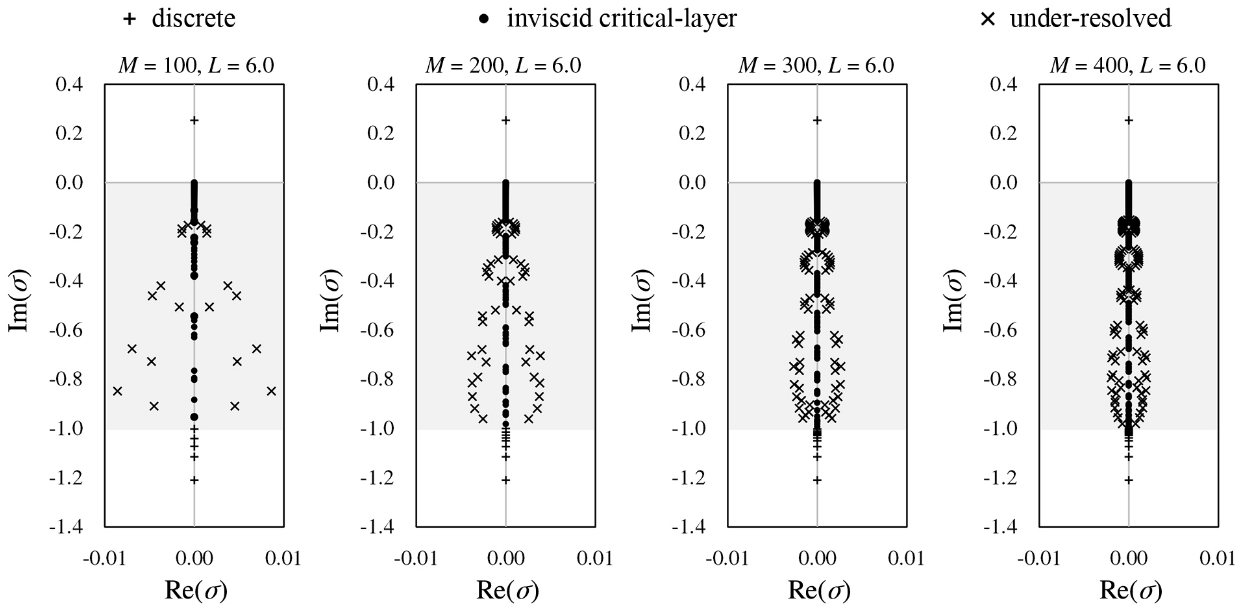

(a) $(m, \kappa, q, Re) = (1, 1.0, \infty, \infty)$

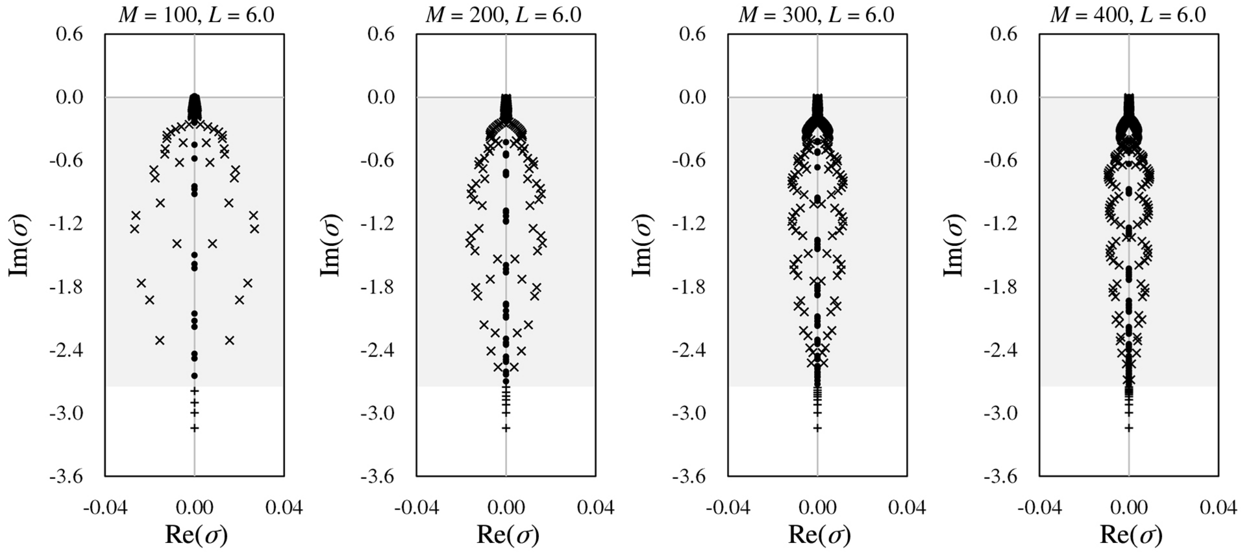

(b) $(m, \kappa, q, Re) = (2, 3.0, 4.0, \infty)$

Figure 6.1: Numerical spectra computed with zero viscosity (a) for the Lamb-Oseen vortex ($q \to \infty$) in $(m, \kappa) = (1,\ 1.0)$ and (b) for the strong swirling Batchelor vortex ($q = 4.0$) in $(m, \kappa) = (2,\ 3.0)$ with respect to $M = 100,\ 200,\ 300$ and 400. L is fixed at 6.0 and $N = M + 2$. A shaded band in each plot indicates the non-normal region where σ_c^0 appears. The larger M we use, the closer the numerical spectra is to their true shape (see figure 5.1(a)). However, with sufficiently large values of M and with appropriately tuned values of L, the under-resolved can be corrected, making all eigenvalues lie on the imaginary axis; see figure 6.5.

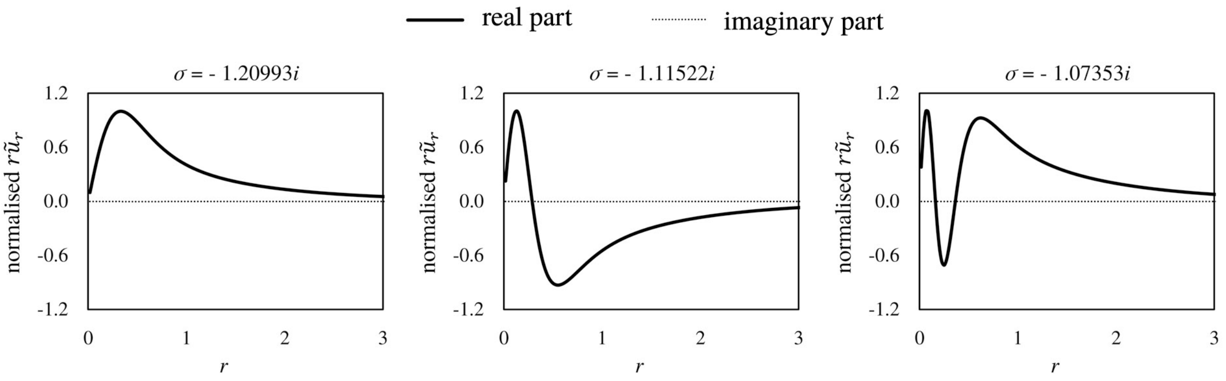

(a) $(m, \kappa, q, Re) = (1, 1.0, \infty, \infty)$

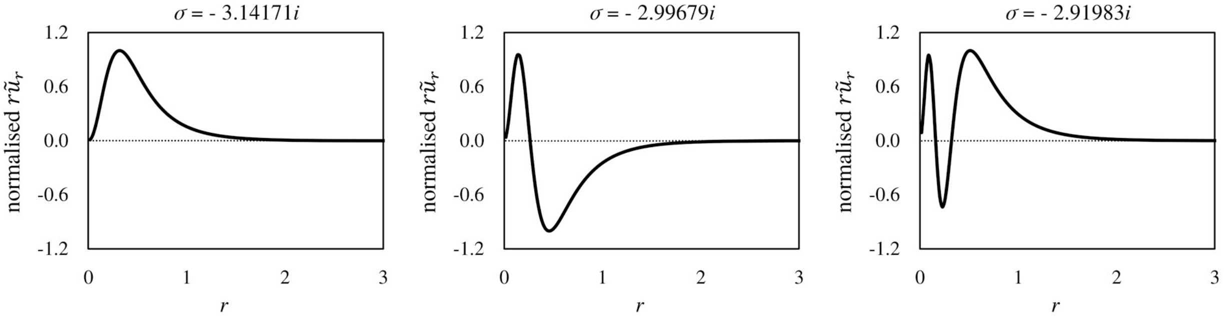

(b) $(m, \kappa, q, Re) = (2, 3.0, 4.0, \infty)$

Figure 6.2: Radial velocity profiles of the inviscid discrete eigenmodes associated with three largest $|\mathrm{Im}(\sigma)|$ (a) for the Lamb-Oseen vortex ($q \to \infty$) in $(m, \kappa) = (1,\ 1.0)$ and (b) for the strong swirling Batchelor vortex ($q = 4.0$) in $(m, \kappa) = (2,\ 3.0)$. The maximum of $\mathrm{Re}(r\tilde{u}_r)$ is normalised to unity. $M = 400$ and $L = 6.0$ are used. The number of "wiggles" in and around the vortex core distinguishes each discrete eigenmode. Note that, for the eigenmodes that are neutrally stable, the phase of the eigenmodes can be chosen such that the radial velocity components are made to be either real or pure imaginary for all r.

The eigenmodes with discrete eigenvalues and $\mathrm{Im}(\sigma)/m > 0$ in figure 6.1 were referred to as "countergrade" by Fabre *et al.* (2006). They appear to exist only for eigenmodes with specific values of m, including $m = \pm 1$ (see Gallay & Smets, 2020). However, we remark that these eigenmodes are also legitimate solutions to the problem and can be spatially resolved using our numerical method, just like those shown in figure 6.2. They are also expected to be crucial for triad-resonant interactions among the eigenmodes and will be actively considered in further instability studies.

The numerically computed eigenmodes correspond to the eigenvectors of the $2M \times 2M$ matrix $\mathbf{L}^0_{m\kappa}$, which implies that the maximum number of numerical eigenmodes that can be obtained is $2M$ under double-precision arithmetic. The number of discrete eigenmodes that our numerical solver can find increases with an increase in M. For instance, in the case of a strong swirling Batchelor vortex illustrated in figure 6.1(b), the number of discrete

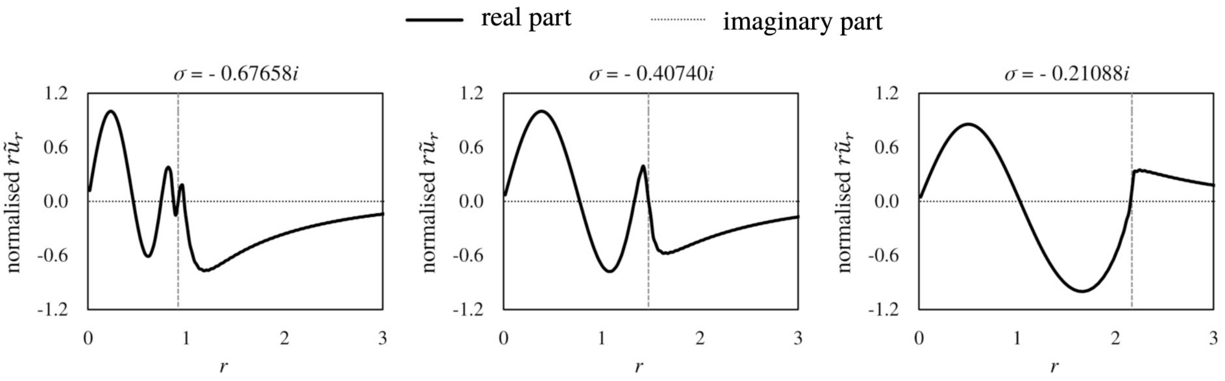

(a) $(m, \kappa, q, Re) = (1, 1.0, \infty, \infty)$

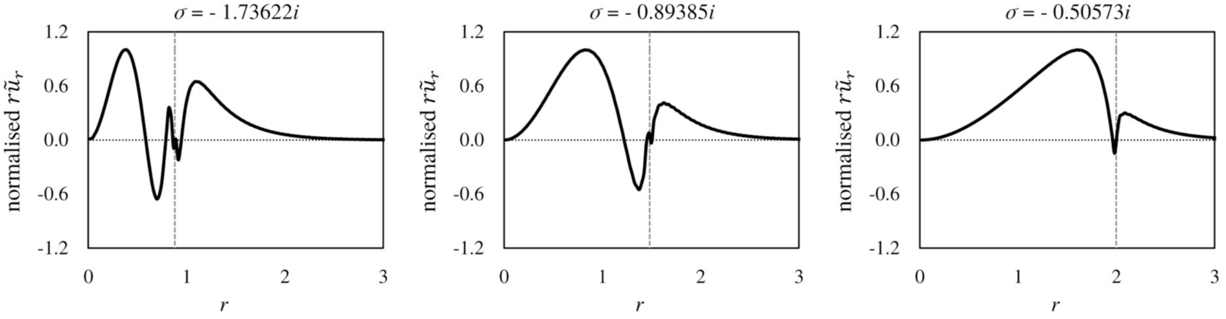

(b) $(m, \kappa, q, Re) = (2, 3.0, 4.0, \infty)$

Figure 6.3: Radial velocity profiles of three inviscid, critical-layer eigenmodes (*a*) for the Lamb-Oseen vortex ($q \to \infty$) in $(m, \kappa) = (1,\ 1.0)$ and (*b*) for the strong swirling Batchelor vortex ($q = 4.0$) in $(m, \kappa) = (2,\ 3.0)$. The maximum of the real part of $r\tilde{u}_r$ is normalised to unity. $M = 400$, $N = M + 2$, and $L = 6.0$ are used. For each eigenmode, the vertical dashed line indicates the critical layer location r_c determined by (5.9). Note that all of the radial components of the velocity can be made to be real-valued for all r by a proper choice of phase as they are neutrally stable as well as discrete ones.

eigenmodes (i.e., in the σ_d^0 spectrum) is 4, 7, 9, and 11 with respect to $M = 100$, 200, 300, and 400, respectively. This behaviour is expected because a finer spatial resolution is required to resolve more wiggles in the eigenmode structure. If n wiggles exist in the vortex core region ($r \leq 1.122$), whose non-dimensionalised scale is of order unity, the necessary spatial resolution to resolve all the wiggles is $O(1/n)$. As $\Delta = 2L/(M + 2) \sim O(1/M)$ in our analysis, the proportionality of n to M is verified. The implication of this scaling is that the number of discrete eigenmodes accounts for only a small portion of the total number of numerical eigenmodes computed, and the vast majority are associated with the non-regular, continuous part of the spectrum, σ_c^0.

6.1.2 Inviscid critical-layer eigenmodes

We emphasise that our essential interest lies in eigenmodes with small, but non-zero viscosity. This ensures that the eigenmodes can be physical and do not have difficult-to-compute singularities. Nevertheless, it is still intriguing to compute the eigenmodes with $\nu \equiv 0$, which are numerically (not physically) regularisable by the spatial discretisation. By selecting a suitably large value of M and an appropriate value for the mapping parameter L (see §6.2), we can resolve the spatial structure of the inviscid eigenmode outside the critical-layer singularity neighbourhood well. In addition, the numerical error in the eigenvalue, caused by the slow decay of spectral coefficients or the Gibbs phenomenon around the critical-layer singularity, can be kept adequately small and the eigenvalues correctly lie on the imaginary axis.

Figure 6.3 shows some critical-layer eigenmodes, which were numerically obtained with $M = 400$. The real parts of the eigenvalues are zero, and the velocity components are either real or purely imaginary for all r, with a suitable phase choice. Typically, r_c increases as $|\sigma|$ decreases along the critical-layer spectrum. The singular behaviour of abrupt slope change commonly occurs at the critical layer singularity, as predicted analytically by (5.9). As stated in §2.3, we cannot claim that they are perfectly resolved due to the presence of the singularity and the continuous nature of their associated spectrum. However, our focus is not on their exact convergence but rather on their well-behaved spatial structure outside the neighbourhood of the singularity, achieved by using a large M, along with purely imaginary eigenvalues that conform to analytic expectations. We use this information later to study the spatial correspondence of eigenmodes with non-zero viscosity to determine which viscous eigenmodes are of physical relevance.

For $r < r_c$, the radial velocity components of the inviscid critical-layer eigenmodes oscillate in r, and the number of oscillations decreases as the value of r_c increases (or equivalently, as $|\sigma|$ decreases). Consequently, when $r_c > r_{cc}$ for some value r_{cc}, there is no longer one full oscillation. In our numerical investigation, we found that for the Lamb-Oseen vortex with $(m, \kappa) = (1, 1.0)$, r_{cc} equals 2.2, which corresponds to $\sigma = -0.21\mathrm{i}$. We believe that our numerically found value of r_{cc} approximately coincides with the theoretical threshold of $r = 2.124$, at which the analytic solutions obtained by the Frobenius method change form regarding the roots of the indicial equation (see Gallay & Smets, 2020, p. 20 and p. 50). For $r > r_c$, the radial velocity components of the critical-layer eigenmodes are not oscillatory, and the amplitudes of $r\tilde{u}_r$ achieve the local maximum or minimum values close to $r = r_c$, before decreasing monotonically as rapidly as those of the discrete eigenmodes, as shown in figure 6.2.

6.1.3 Under-resolved eigenmodes

The under-resolved eigenmodes, which, if resolved, would be part of the spectrum with σ_c^0, have eigenvalues in the complex σ-plane on either side of the imaginary axis in the shaded region in figure 6.1. The eigenvalues come in pairs, with one unstable and one stable eigenmode. The reflection symmetry with respect to the imaginary axis is due to the fact that the analytic operator $\mathcal{L}^0_{m\kappa}$ is time-reversible (cf. Bölle *et al.*, 2021, p. 10). Therefore, the eigenmode $(\tilde{u}_r, \tilde{u}_\phi, \tilde{u}_z, \tilde{p})$ with eigenvalue σ_s corresponds to the eigenmode $(\tilde{u}_r^*, -\tilde{u}_\phi^*, -\tilde{u}_z^*, -\tilde{p}^*)$ with eigenvalue $-\sigma_s^*$.

Some examples of under-resolved eigenmodes are shown in figure 6.4. These eigenmodes are qualitatively incorrect because (1) unlike the eigenmodes in figure 6.2 and figure 6.3, there is no choice of phase that makes their radial components real for all r, and more importantly, because (2) we know that their eigenvalues should be purely imaginary when q is sufficiently large, and they are not. However, these eigenmodes appear to exhibit no other distinguishing properties, except for the two properties listed above, from the inviscid critical-layer eigenmodes in figure 6.3. It should be noted that they have been called "*spurious*" in previous numerical studies (see Mayer & Powell, 1992; Heaton, 2007a), of which the usage was similar to our clarification given in §2.3. However, instead of following convention, we propose naming these numerical eigenmodes "*under-resolved*" eigenmodes of the continuous part of the inviscid spectrum. In this way, we put more emphasis on the fact that adjusting the numerical parameters can "correct" these eigenmodes so that neither of the two key properties listed above applies.

By examining the spatial structure of the under-resolved eigenmodes, we can detect sudden changes in slope at the critical-layer singularity point at $r = r_c$. The value of r_c is obtained by setting the imaginary part of either of the eigenvalues $\mathrm{Im}(\sigma_s)$ to σ_c in (5.9). The break in slope confirms that the under-resolved eigenmodes originate from σ_c^0 and indicates that they have lost their neutrally stable property due to numerical errors at the critical-layer singularity.

Correcting the under-resolved eigenmodes is crucial, not only for correctly evaluating σ_c^0 but also for the following reasons. Despite their invalid origin, half of the under-resolved eigenmodes in $\mathrm{Re}(\sigma) > 0$ erroneously suggest that the wake vortex is linearly unstable. In the future, we plan to use the computed velocity eigenmodes from the present numerical method to initialise an initial-value code that solves the full nonlinear equations of motion given by (3.1.6) and (3.1.7). Inappropriately computed eigenmodes that grow erroneously, rather than remain neutrally stable, are likely to corrupt these calculations.

6.2 Correction of the under-resolved eigenmodes

An intriguing question is whether the under-resolved eigenmodes tend towards something as M increases. What is the potential outcome of such convergence? In the beginning of this section, it was argued that the real part of eigenvalues remains at zero (i.e., all eigenmodes are neutrally stable) when q is sufficiently large. In figure 6.1, this can be observed as the "squeeze" of the eigenvalue cluster towards the imaginary axis. However, we have also indicated that the imaginary part of eigenvalues may not converge to a fixed point, instead continuing to evolve along the imaginary axis. Therefore, instead of concentrating on the convergence of individual under-resolved eigenmodes to a fixed point, it is more pragmatic

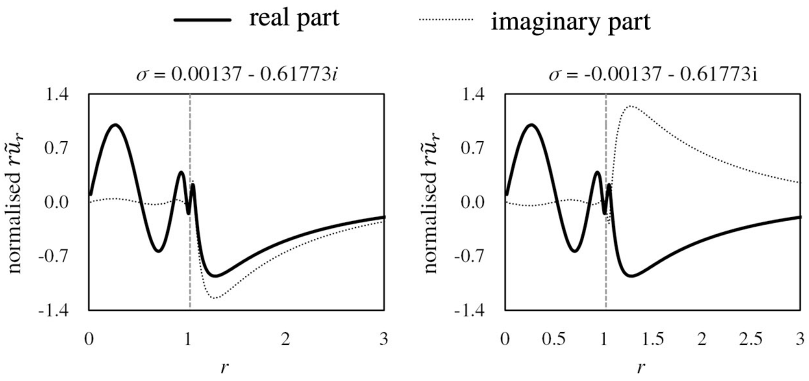

(a) (m, κ, q, Re) = (1, 1.0, ∞, ∞)

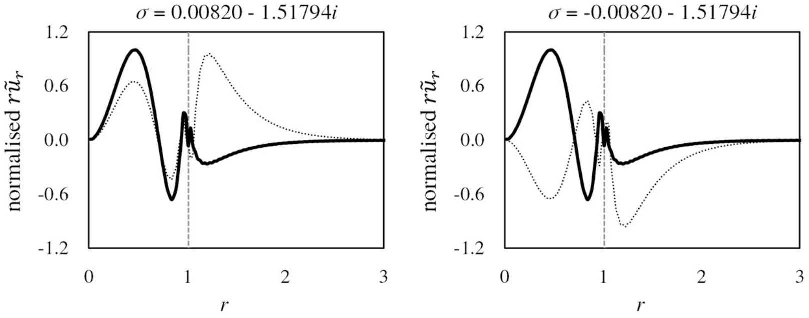

(b) (m, κ, q, Re) = (2, 3.0, 4.0, ∞)

Figure 6.4: Radial velocity profiles of two inviscid under-resolved eigenmodes whose eigenvalues are symmetric about the imaginary axis (a) for the Lamb-Oseen vortex ($q \to \infty$) in $(m, \kappa) = (1,\ 1.0)$ and (b) for the strong swirling Batchelor vortex ($q = 4.0$) in $(m, \kappa) = (2,\ 3.0)$. The maximum of the real part of $r\tilde{u}_r$ is normalised to unity. $M = 400$ and $L = 6.0$ are used. For each eigenmode, an abrupt slope change occurs at the vertical dashed line at the critical layer location, $r = r_c$ (which is determined from (5.9) by ignoring the real part of the eigenvalue), indicating that they will become correct critical-layer eigenmodes given more resolution.

to aim to "correct" the set of eigenmodes as a whole, that is, to restore their neutrally stable nature. The "correction" means that we comprehensively treat the entire set of eigenmodes as a single entity, which complies with the usage of this term in this section up to this point.

To "correct" the under-resolved eigenmodes, We first consider increasing M to its largest possible value within the available computing resources. However, increasing M is generally undesirable because it always comes at a steep computational expense; the cost of finding the eigenmodes is proportional to $(2M)^3$. Instead, we may consider dealing with the mapping parameter L, where the novelty and usefulness of our method come from. L controls the spatial resolution locally as a function of r. As seen from the resolution parameter Δ in (4.2.4), L controls the spatial resolution by providing more resolution near the radial origin (i.e., $0 \leq r < L$). It is important to note that changing or tuning L does not affect the cost of computation.

For a fixed M, with $N = M + 2$, figure 6.5 shows five numerical eigenvalue spectra for two prescribed cases with different values of L, varying from 1.0 to 5.0. Overall, decreasing L brings the numerical spectra closer to the imaginary axis. In particular, some values of L enable complete resolution of σ_c^0 on the imaginary axis, which cannot be achieved by increasing M within a modest computing budget. However, decreasing L does not always shrink the clouds of eigenvalues closer to the imaginary axis. We separate the numerically computed eigenvalues and eigenmodes into two categories: those with the critical layer $r = r_c$ located in the high-resolution region $0 \leq r < L$, and those where r_c is in the low-resolution region $r \geq L$. Figure 6.5 indicates this separation with horizontal dashed lines. For the former, the cloud structures vanish as L decreases, and σ_c^0 is correctly resolved. In contrast, for the latter, the cloud structures persist or even recur if L is too small, resulting from excessive concentration of collocation points solely around the center. Once σ_c^0 is satisfactorily resolved, adjusting L should stop to keep the portion of σ_c^0 resolved in the high-resolution region as large as possible. For instance, in figure 6.5, we propose setting L between 3.0 and 4.0 for the Lamb-Oseen vortex case and between 1.0 and 2.0 for the Batchelor vortex case.

To provide a detailed explanation of what we have seen, we must revisit the differences in the way M and L operate in the current numerical method, as stated in §4.3. One of the roles of L is to serve as a tuning parameter for spatial resolution in physical space, whereas M determines the number of basis elements used in spectral space. Increasing M allows us to handle eigenmodes with more complex shapes, such as (nearly) singular functions, which often have more wiggling and are thus more numerically sensitive. M has only an indirect effect on spatial resolution through N, which is required to be greater than or equal to M. On the other hand, the critical-layer singularity is essentially a phenomenon that occurs in physical space. Although using more spectral basis elements relates to improving spatial resolution because we set $N = M + 2$, the main contribution to dealing with the critical-layer singularity with minimal errors comes from the latter. Therefore, it can be more effective to use L to directly control resolution and suppress the emergence of under-resolved eigenmodes, rather than using M. It is worth noting that increasing N to very large values while keeping M constant can also reduce the number of under-resolved eigenvalues to some extent. This observation supports that high spatial resolution is crucial for suppressing under-resolved eigenmodes.

If one aims to correct the under-resolved eigenmodes and obtain σ_c^0 using the present numerical method, the following steps are suggested to properly set up the numerical parameters. Assuming that M is already at the practical maximum due to finite computing budget, and N follows $M + 2$:

1. Start with an arbitrarily chosen value of L and gradually decrease it if under-resolved eigenmodes exist, until they vanish in the high-resolution region $0 \leq r < L$. This step improves spatial resolution, helping to identify the critical-layer singularity with less numerical error despite the discretisation.

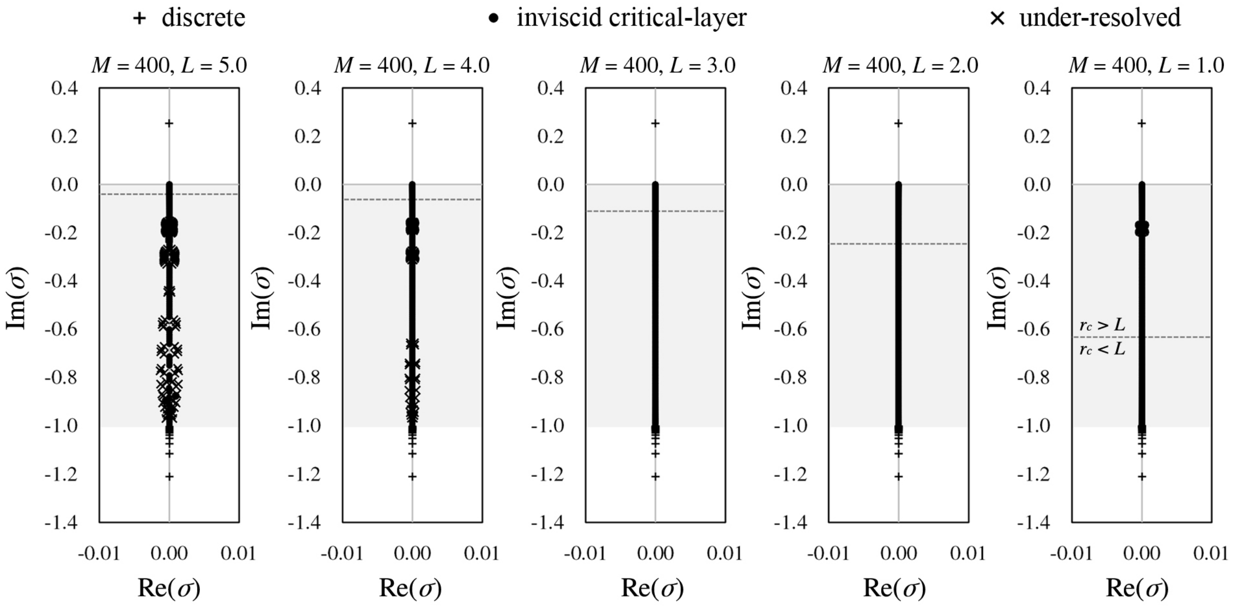

(a) (*m*, *κ*, *q*, *Re*) = (1, 1.0, ∞, ∞)

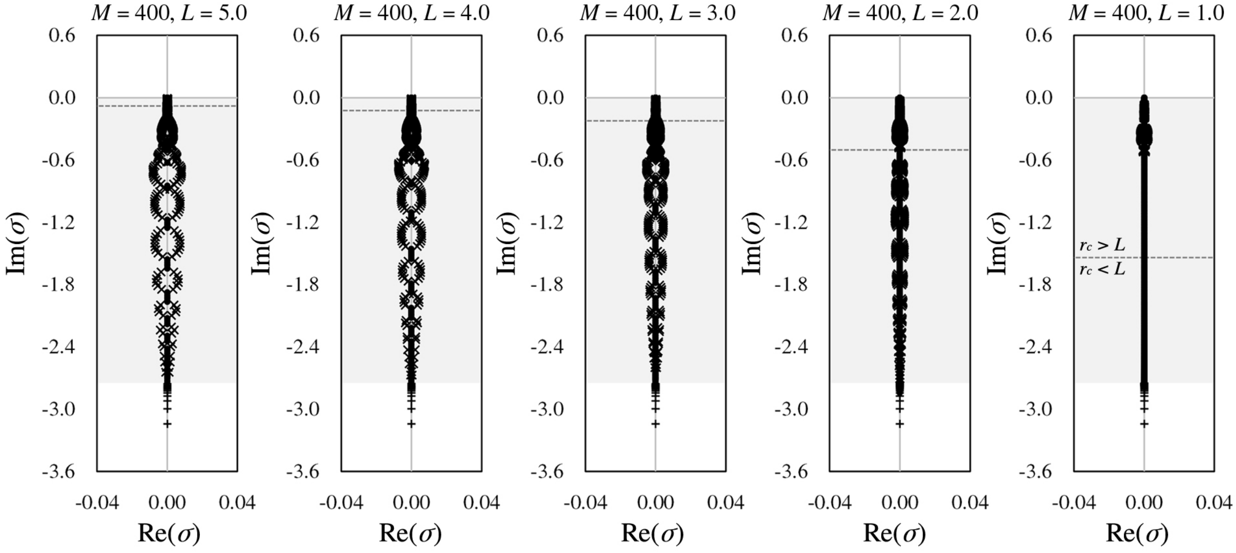

(b) (*m*, *κ*, *q*, *Re*) = (2, 3.0, 4.0, ∞)

Figure 6.5: Numerical spectra computed at zero viscosity (a) for the Lamb-Oseen vortex ($q \to \infty$) in $(m, \kappa) = (1,\ 1.0)$ and (b) for the strong swirling Batchelor vortex ($q = 4.0$) in $(m, \kappa) = (2,\ 3.0)$ with respect to $L = 5.0,\ 4.0,\ 3.0,\ 2.0$ and 1.0. M is fixed at 400 and $N = M + 2$. n each plot, a shaded band indicates the non-normal region in which σ_c^0 appears, and a horizontal dashed line represents the threshold used to determine if the critical layer $r = r_c$ is located within the high-resolution region $0 \leq r < L$. It should be noted that there is a one-to-one correspondence between a critical-layer eigenvalue σ and a critical-layer radius r_c, as seen in (5.9). Furthermore, r_c approaches zero at the bottom of the shaded band, $\mathrm{Im}(\sigma) = m + \kappa/q$, and monotonically increases towards infinity as $|\sigma|$ becomes smaller. By tuning L, under-resolved eigenmodes can be corrected without requiring additional computing resources.

2. If there are no eigenvalue clouds around the imaginary axis, increase L as long as they do not appear in the numerical spectra. This step expands the high-resolution region where the critical-layer singularity can be accurately treated.

6.3 Pairing in the inviscid critical-layer spectrum

In the numerical spectrum of σ_c^0, we observe that numerical eigenvalues tend to appear in pairs. This pairing phenomenon is demonstrated in the left panel of figure 6.6, which illustrates the Lamb-Oseen vortex case with $(m, \kappa) = (1,\ 1.0)$ that we computed with $M = 400$ and $L = 3.0$ (see figure 6.5(a)). We argue that the pairing in our numerical results arises from a degeneracy resulting from the critical-layer singularity. We refer to Gallay and Smets (2020, pp. 19-21), who used the Frobenius method to construct analytic solutions to the problem under the assumption of non-zero m and κ with $q \to \infty$. They showed that if a critical-layer singularity occurs at $r = r_c$, there exists a unique solution with scalar multiplication that is only non-zero on $(0, r_c)$ and another one that is only non-zero on (r_c, ∞). Here we call them inner and outer solutions, respectively. For both the inner and outer solutions, the radial velocity components can be made real-valued by an appropriate choice of phase, since their degenerate eigenvalue is purely imaginary. These two solutions are independent of each other, and their linear combination should be the general form of an inviscid critical-layer eigenmode that is singular at $r = r_c$.

We can observe these analytic characteristics in our numerically computed pairs. In the right panel of figure 6.6, we present the $r\tilde{u}_r$ profiles of the critical-layer eigenmodes from two neighboring pairs. In each pair, the velocity profiles have an abrupt change in slope across an interval between two collocation points, whose location matches the critical-layer singularity radius calculated by (5.9). The difference in r_c among the neighboring pairs corresponds to the collocation interval, indicating their continuous emergence. Furthermore, by linearly combining these paired eigenmodes, we can construct the inner and outer solutions as derived analytically, each of which is approximately zero on $(0, r_c)$ or (r_c, ∞). Although their eigenvalues are slightly different, we believe that it is due to the numerical error resulting from the spatial discretisation, which slightly breaks the degeneracy. This error decreases with increasing M.

Strictly speaking, the discussion made here is limited to infinite q, because the analytic results found in Gallay and Smets (2020) were verified in the Lamb-Oseen vortex case, and we can only compare this case. Nonetheless, we remark that we have numerically observed this same pairing phenomenon with finite q (e.g., $q = 4.0$). We conjecture that the pairing phenomenon exists for values of q where the eigenmodes are all neutrally stable.

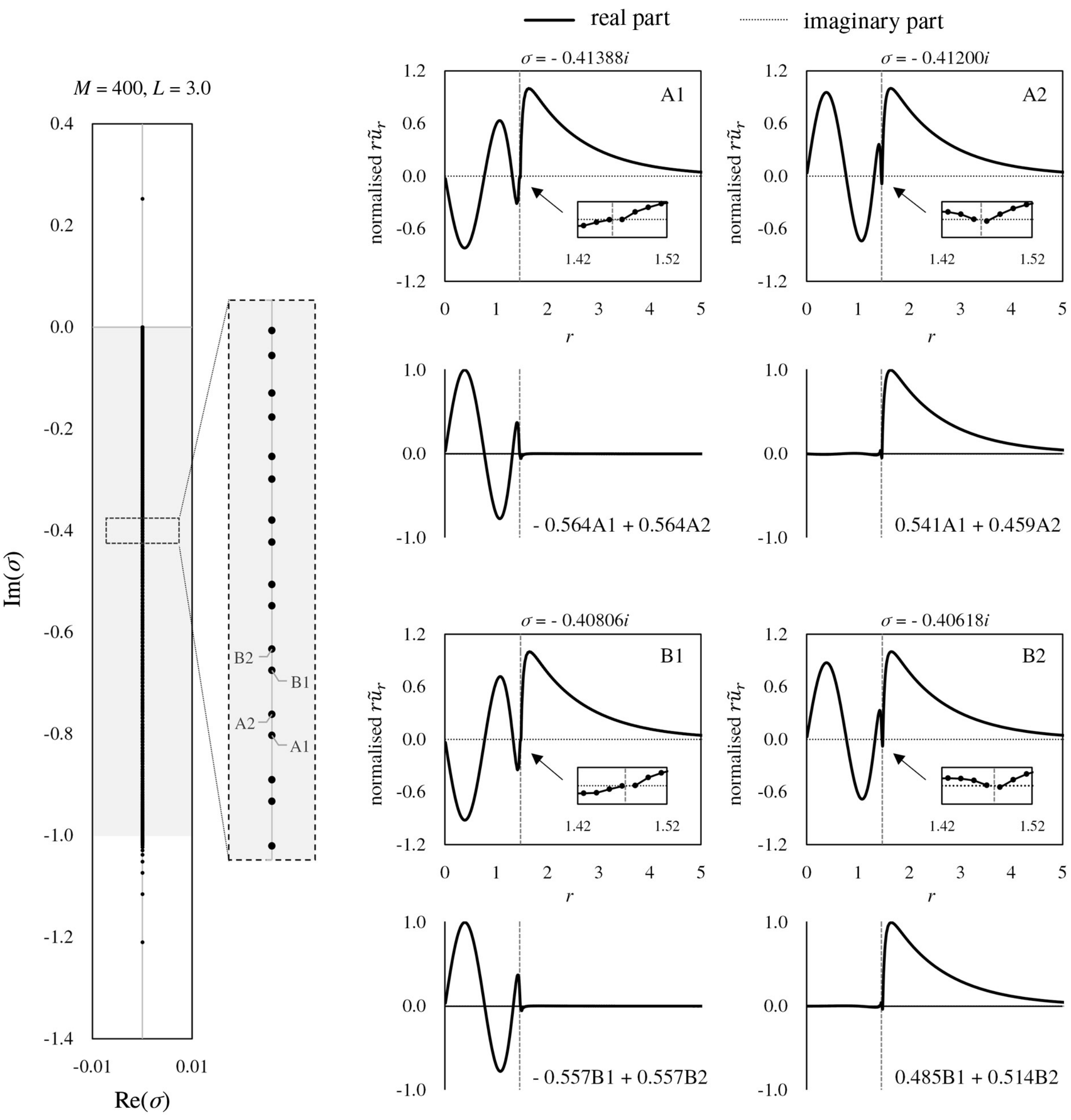

(a) Numerical spectra *(b)* Numerical critical-layer eigenmodes in pairs

Figure 6.6: (*a*) Numerical inviscid spectra with no under-resolved eigenmodes for the Lamb-Oseen vortex ($q \to \infty$) in $(m, \kappa) = (1,\ 1.0)$ along with a magnified part exhibiting the pairing phenomenon, and (*b*) four radial velocity profiles of the critical-layer eigenmodes from two neighboring pairs, labelled as A1/2 and B1/2. Here, $M = 400$, $L = 3.0$, and $N = M + 2$. Note the similarity in structure within each pair, and the change in the critical layer location (marked by vertical dashed lines) by one collocation point between these neighboring pairs. This pairing phenomenon stems from the singular degeneracy in σ_c^0. The linear combination of the pair constructs two independent solutions that are singular at the same critical-layer location and are nearly zero on either $(0, r_c)$ or (r_c, ∞).

Chapter 7

Viscous linear analysis

We numerically examine the viscous eigenvalue problem $\sigma\left[\mathbb{P}_{m\kappa}(\tilde{\boldsymbol{u}})\right] = \mathcal{L}^{\nu}_{m\kappa}\left[\mathbb{P}_{m\kappa}(\tilde{\boldsymbol{u}})\right]$ by studying the spectra of the discretised operator $\mathsf{L}^{\nu}_{m\kappa}$ and their associated eigenmodes. Due to viscous regularisation, the viscous eigenmodes do not exhibit critical-layer singularities. Instead, at or near the locations where the inviscid critical layer would have been, the viscous eigenmodes have thin layers characterised by large amplitudes and small-scale oscillations, with widths proportional to $Re^{-1/3}$ (Maslowe, 1986; Le Dizès, 2004). Note that the $Re^{-1/3}$ law is a well-established analytic principle, similar to the $Re^{-1/2}$ law for the laminar viscous boundary layer thickness. Several classic textbooks have already provided an in-depth description of this principle (see Lin, 1955; Drazin & Reid, 2004).

The families of viscous eigenmodes are not just small corrections to the inviscid eigenmodes; the addition of the viscous term, despite being small for Re^{-1}, serves as a *singular* perturbation (Lin, 1961). This is because it increases the spatial order of the set of equations that govern the eigenmodes. Therefore, the linear stability features of wake vortices from vanishing viscosity can differ from the purely inviscid instability characteristics (see Fabre & Jacquin, 2004, p. 258). It is well known that exactly inviscid flows where $\nu \equiv 0$ often behave quite differently from high Reynolds number flows where $\nu \to 0^+$. In particular, not only do the locations of the eigenvalues in the complex σ-plane change, but new families can also be created. One example is the freestream spectrum σ^{ν}_{f} shown in figure 5.1. This spectrum consists of non-normalisable eigenmodes that do not vanish as $r \to \infty$ and is mathematically derivable. However, its non-physical behaviour at radial infinity renders it unsuitable for computation using our method. Otherwise, all other families that we depicted in figure 5.1 are in the scope of the analysis.

Mao and Sherwin (2011) and Bölle *et al.* (2021) reported that the inviscid critical-layer spectrum σ^{0}_{c} changes with viscosity and spreads to an area on the left half-plane of the complex σ-plane, which they called the potential spectrum σ^{ν}_{p}. In this section, we demonstrate that our numerical method can produce randomly scattered eigenvalues, which represent σ^{ν}_{p} numerically as reported by previous authors, and investigate their spatial characteristics. Also, we identify and describe the viscous critical-layer eigenmodes associated with the spectrum σ^{ν}_{c} (see figure 5.1), which, to the best of our knowledge, have not been distinguished before.

7.1 Numerical spectra and eigenmodes

The Lamb-Oseen vortex with $(m, \kappa, q) = (1, 1.0, \infty)$ and the strong swirling Batchelor vortex with $(m, \kappa, q) = (2, 3.0, 4.0)$ are analysed at $Re = 10^5$. As with the prior inviscid analysis, our aim is to identify common characteristics in the linear vortex dynamics with viscosity for large q and moderate m and κ. In the current analysis, however, we have a specific focus on the physical relevance of each eigensolution. To observe how the viscous numerical spectra converge, we compute four numerical spectra for each case, with different values of M ranging from 100 to 400. The spectra are presented in figure 7.1, or movie 1. Movies of the spectrum animations are provided with the supplementary material available at S. Lee and Marcus (2023). Based on these spectra, we classify the numerical eigenmodes into five families: unresolved (—), discrete (+), spurious (×), potential (□), and viscous critical-layer (●). Note that with increasing numerical resolution, an eigenmode in the unresolved family will always evolve into an eigenmode in one of the other four families.

The eigenvalues in the discrete spectrum, σ_d^ν, converge to fixed points with increasing M. These eigenvalues populate two distinct discrete branches shown near the bottom of the panels in figure 7.1, in addition to a few locations outside of these branches. The eigenmodes in the discrete spectrum were known previously and were studied by other authors. For example, according to Fabre *et al.* (2006), the lower branch was designated as the C-family, while the upper one was labelled the V-family.

With viscosity, none of the eigenmodes have critical-layer singularities as they are regularised, and no eigenvalues lie exactly along the imaginary axis. In the non-normal region, the spectrum of eigenmodes, σ_p^ν, that we have labelled as potential, occupies an area in the complex σ-plane that stretches out towards $\mathrm{Re}(\sigma) \to -\infty$ as M increases. However, unlike the region shown in the schematic in figure 5.1, there is a gap between the upper bound of this numerical spectrum and the real axis on which the freestream spectrum σ_f^ν is located. The reason is that we force solutions to vanish at radial infinity due to the decaying nature of the spectral basis elements. Therefore, the gap should be considered a peculiar product of our numerical method that excludes solutions with decay rates that are too slow in r, such as those with velocity decaying slower than $O(r^{-1})$ in r and ϕ, or $O(r^{-2})$ in z in the far field; see (3.3.8) in §3.3.

The fact that the numerically computed eigenvalues in σ_p^ν shift towards the left side of the complex σ-plane as M increases coincides with Mao and Sherwin (2011). Additionally, the number of potential eigenmodes increases with increasing M. Up to the largest value of M that we have explored, the numerical eigenvalues in σ_p^ν tend to emerge randomly. This random scattering can be understood as the spectrum's extremely high sensitivity to numerical errors even in the order of machine precision (see §7.4.1).

On the other hand, we observe a moving branch of numerical eigenvalues attached to the left end of σ_p^ν. They also never converge with respect to M, and the values of their $|\mathrm{Re}(\sigma)|$

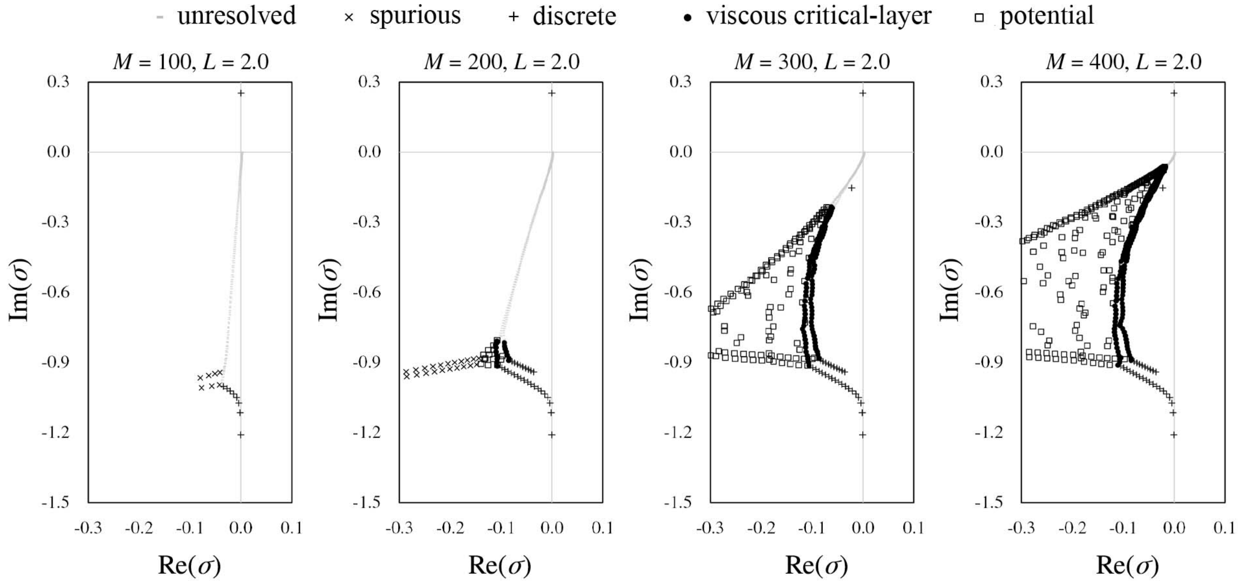

(a) $(m, \kappa, q, Re) = (1, 1.0, \infty, 10^5)$

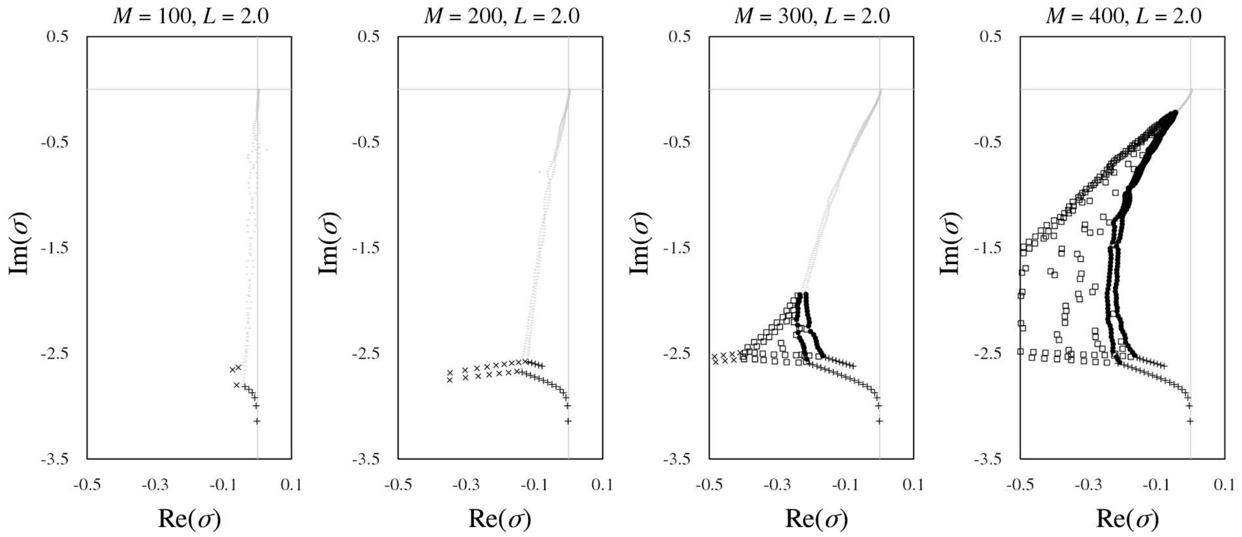

(b) $(m, \kappa, q, Re) = (2, 3.0, 4.0, 10^5)$

Figure 7.1: Numerical viscous spectra at $Re = 10^5$ (*a*) for the Lamb-Oseen vortex ($q \to \infty$) in $(m, \kappa) = (1, 1.0)$ and (*b*) for the strong swirling Batchelor vortex ($q = 4.0$) in $(m, \kappa) = (2, 3.0)$ with respect to $M = 100$, 200, 300 and 400. L is fixed at 2.0 and $N = M + 2$. Larger M enables more portion of the spectra to be resolved. Near the right boundary of the potential spectrum there are two distinct branches of the viscous critical-layer spectrum. See movie 1 (available at S. Lee & Marcus, 2023) for animation.

increase rapidly. We explicitly label them as spurious because of their absolutely irregular spatial characteristics, as shown later in §7.1.2. Although they are not removable, we can pull them away by setting M to a large value.

Last but not least, we report the presence of two new distinct branches of viscous critical-layer eigenvalues, which are seen on the right side of the area containing the potential eigenvalues. The two branches of these eigenvalues, σ_c^ν, as depicted in figure 5.1, converge to distinct loci. We distinguish σ_c^ν from σ_p^ν because of their unique bifurcating shape. Furthermore, this is the only part of the spectra in the non-normal region that approach fixed points at finite M, along with the discrete spectrum. As the name suggests, we argue that their associated eigenmodes are not only non-spurious but also physical, since they are the *true* viscous remnants of the inviscid critical-layer eigenmodes, as explained with details in §7.1.4.

7.1.1 Discrete eigenmodes

Figure 7.2 presents three viscous discrete eigenmodes with respect to each base flow, whose spatial structures are inherited from the inviscid discrete eigenmodes displayed in figure 6.2. They remain non-singular throughout the whole radial domain. Viscosity only marginally affects the spatial structures of these eigenmodes compared to their inviscid counterparts, making the velocity components have slightly non-zero imaginary parts due to viscous perturbation. The number of wiggles in the eigenmodes still determines their spatial characteristics. Moreover, those eigenmodes with more wiggles near $r = 0$ are more stable over time, i.e., $|\mathrm{Re}(\sigma)|$ increases. This phenomenon is physically justifiable since the spatial gradient of velocity components becomes steeper when the spacing between the wiggles is reduced, and viscous diffusion should, therefore, be more intensive. These eigenmodes are physical as they are regular, well-resolved solutions to the linearised Navier-Stokes equations on the q-vortex. They are typically characterised by modest wiggles that are spatially resolved, have rapid monotonous decay in r, and clearly correspond to the inviscid discrete eigenmodes associated with σ_d^0.

7.1.2 Spurious eigenmodes

Two numerically computed eigenmodes that represent the viscous spurious eigenmodes are shown in figure 7.3. We have not observed any signs of convergence up to $M = 400$. These eigenmodes are not spatially resolved, as evidenced by irregularly fast oscillations that alternate at every collocation point. It is apparent that they are neither analytically nor physically meaningful. Therefore, we will not perform an in-depth analysis of them.

7.1.3 Potential eigenmodes

Next, we examine the numerical eigenmodes associated with σ_p^ν, or the potential eigenmodes. If we look at the randomly scattered eigenvalues while increasing M, it is possible to ob-

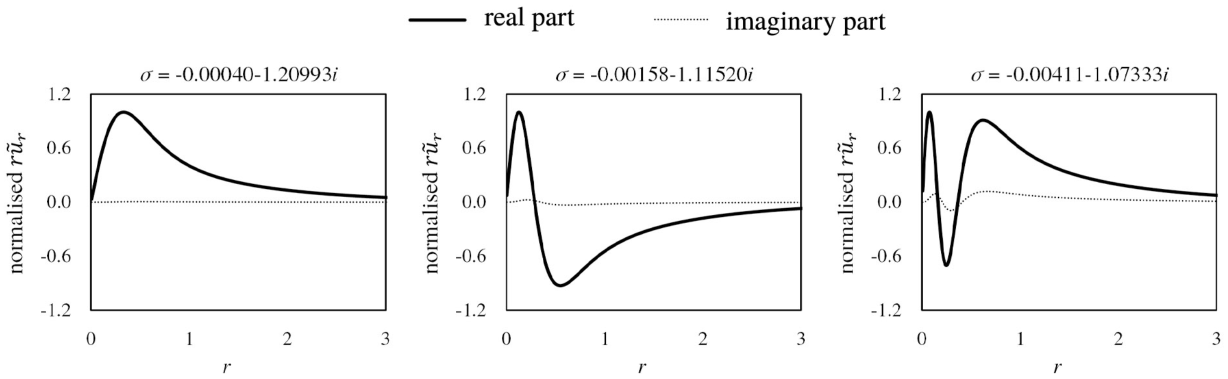

(a) $(m, \kappa, q, Re) = (1, 1.0, \infty, 10^5)$

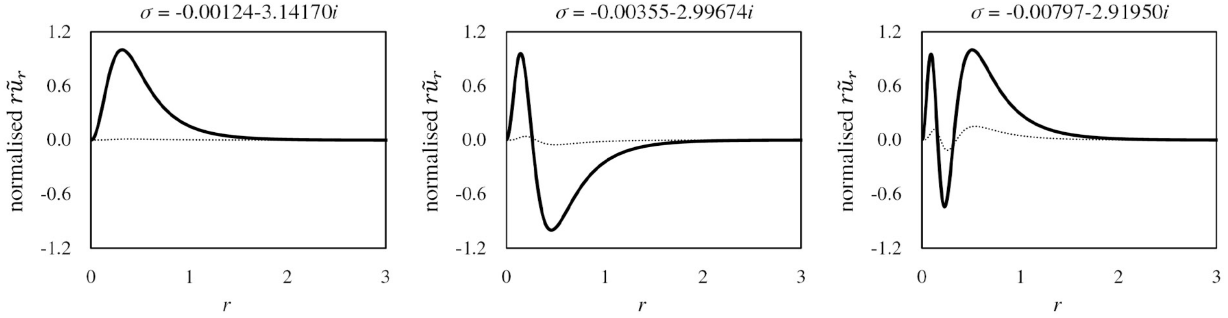

(b) $(m, \kappa, q, Re) = (2, 3.0, 4.0, 10^5)$

Figure 7.2: Radial velocity profiles of the viscous discrete eigenmodes associated with three smallest $\mathrm{Im}(\sigma)$ (a) for the Lamb-Oseen vortex ($q \to \infty$) in $(m, \kappa) = (1,\ 1.0)$ and (b) for the strong swirling Batchelor vortex ($q = 4.0$) in $(m, \kappa) = (2,\ 3.0)$. The maximum of $\mathrm{Re}(r\tilde{u}_r)$ is normalised to unity. $M = 400$ and $L = 2.0$ are used. Compare with the inviscid counterparts in figure 6.2, and notice that viscosity only marginally affects these eigenmodes.

serve common spatial characteristics of these eigenmodes that are spatially resolved with a sufficiently large value of M, unlike the *spurious* family mentioned above. Figure 7.4 presents the three representative potential eigenmodes for each vortex case, using $M = 400$. We note that we have selected eigenmodes whose smallest wiggle is captured with more than two collocation points to ensure that we validly discuss their common spatial features. These eigenmodes are characterised by excessive wiggles, resulting in slow radial decay rates (cf. Mao & Sherwin, 2011). They exhibit generally faster decay rates in time (i.e., larger $|\mathrm{Re}(\sigma)|$) than the discrete ones, as more wiggles demand steeper spatial gradients vulnerable to viscous diffusion.

The potential eigenmodes have wiggles that are usually concentrated roughly near the inviscid critical-layer singularity locations, which is estimated by setting their $\mathrm{Im}(\sigma)$ to σ_c in (5.9). In other words, as noted by Mao and Sherwin (2011), they take the form of "wavepackets," whose major oscillatory components are localised both in physical and spectral spaces.

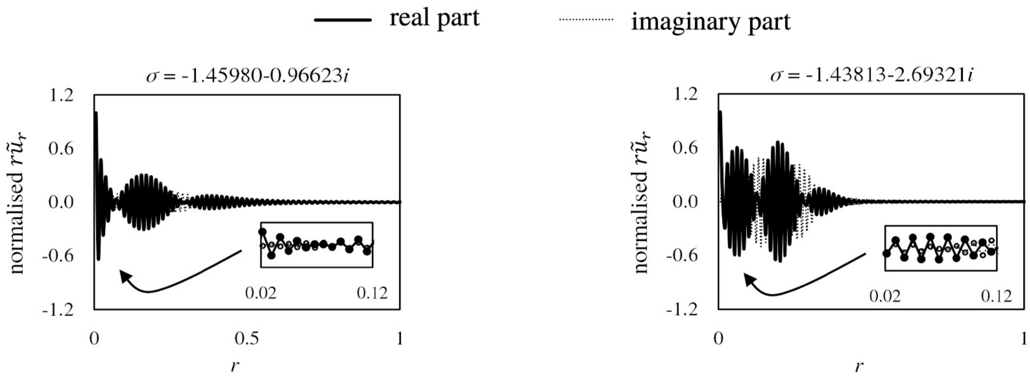

(a) $(m, \kappa, q, Re) = (1, 1.0, \infty, 10^5)$ *(b)* $(m, \kappa, q, Re) = (2, 3.0, 4.0, 10^5)$

Figure 7.3: Radial velocity profiles of a representative viscous spurious eigenmode (*a*) for the Lamb-Oseen vortex ($q \to \infty$) in $(m, \kappa) = (1,\ 1.0)$ and (*b*) for the strong swirling Batchelor vortex ($q = 4.0$) in $(m, \kappa) = (2,\ 3.0)$. The maximum of $\mathrm{Re}(r\tilde{u}_r)$ is normalised to unity. $M = 400$ and $L = 2.0$ are used. Non-trivial and irregularly fast oscillations with alternating sign at every collocation point, as shown in each inset for magnification, manifest that they are spurious.

The correspondence between these "wavepackets" and the inviscid critical-layer singularity locations leads us to posit that the potential eigenmodes originate from the viscous regularisation of the critical layers. From a mathematical standpoint, the introduction of the viscous term serves only to ensure their regularisation and does not impose any restrictions on their appearance following regularisation, such as thickness and wave amplitude. This may explain why potential eigenmodes exhibit various wavepacket widths at different locations.

In figure 7.4, the first and second eigenmodes have similar decay rates in time, i.e., $\mathrm{Re}(\sigma_1) \simeq \mathrm{Re}(\sigma_2)$, which relates to the fact that they also have a similar number of wiggles at their major oscillatory positions. On the other hand, the second and third eigenmodes have similar wave frequencies, i.e., $\mathrm{Im}(\sigma_2) \simeq \mathrm{Im}(\sigma_3)$, which means that their major oscillatory locations are close. As the number of wiggles increases, $|\mathrm{Re}(\sigma)|$ becomes large, and the major oscillatory structure extends to a wide range in r. This extension likely contributes to the retardation of radial decay rates, as the wiggles remain at large radii in small scales (see the insets in figure 7.4).

There are several noteworthy factors that should be pointed out regarding the spatial characteristics of these eigenmodes. Although they appear physical, they make it difficult to believe that they are the *true* viscous remnants of the inviscid critical-layer eigenmodes. First, potential eigenmodes' wavepackets can have varying widths even at the same Re, indicating the absence of a clear scaling relationship between wavepacket widths and the important physical parameter Re. Second, it is challenging to identify a clear spatial similarity to the inviscid critical-layer eigenmodes. The typical radial decaying behaviour of the viscous eigenmodes appears slow and oscillatory, as shown in figure 7.4, in contrast to the inviscid critical-layer eigenmodes that exhibit monotonically rapid radial decay (see figure 6.3). We postulate that the rapid radial decaying behaviour in σ_c^0 must be sustained for its *true* vis-

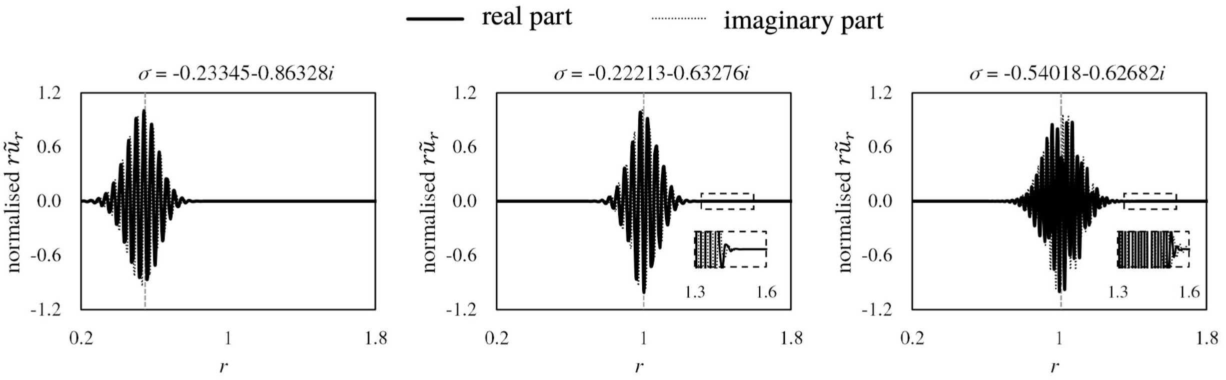

(a) $(m, \kappa, q, Re) = (1, 1.0, \infty, 10^5)$

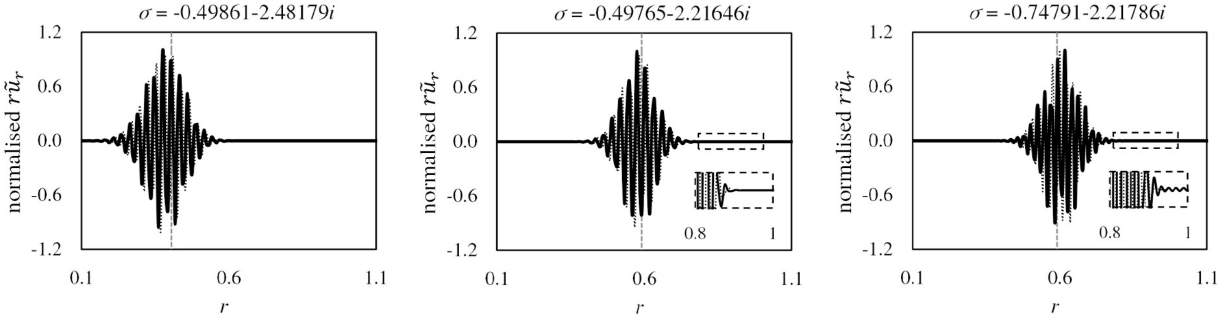

(b) $(m, \kappa, q, Re) = (2, 3.0, 4.0, 10^5)$

Figure 7.4: Radial velocity profiles of three viscous potential eigenmodes (*a*) for the Lamb-Oseen vortex ($q \to \infty$) in $(m, \kappa) = (1,\ 1.0)$ and (*b*) for the strong swirling Batchelor vortex ($q = 4.0$) in $(m, \kappa) = (2,\ 3.0)$. The maximum of $\mathrm{Re}(r\tilde{u}_r)$ is normalised to unity with the use of $M = 400$ and $L = 2.0$. The first and middle two potential eigenmodes exhibit similar $\mathrm{Re}(\sigma)$, and their number of major oscillations is comparable. The middle and last two eigenmodes have similar $\mathrm{Im}(\sigma)$, and their major oscillatory positions are similar. Each vertical dashed line indicates the critical layer location r_c, which is estimated by setting each $\mathrm{Im}(\sigma)$ to σ_c in (5.9). Each inset within a dashed box reveals small-amplitude wiggles where $r\tilde{u}_r \sim O(10^{-5})$ that persist at large r even when the amplitude seems to be nearly zero, indicating their slow radial decay rates.

cous remnants since the viscous regularisation effect should be highly localised around the critical-layer singularity. Therefore, a subsequent question should arise as to which other eigenmodes in the non-normal region can be considered the *true* viscous remnants of σ_c^0. As the name suggests, we claim that the viscous critical-layer eigenmodes associated with σ_c^ν offer the answer, which we set forth in the following.

7.1.4 Viscous critical-layer eigenmodes

Figure 7.5(a) shows two viscous critical-layer eigenmodes of a Lamb-Oseen vortex with values of $\mathrm{Im}(\sigma_c^\nu)$ that are within 6% of each other. Due to the closeness of their eigenvalues and their similar appearances, we believe that they evolved from a pair of degenerate inviscid critical layer eigenmodes. The eigenvalue of the eigenmode in the upper row of figure 7.5(a) is in the left branch, while the lower row is in the right branch of σ_c^ν in figure 5.1 and figure 7.1. We believe that the regions of large amplitude oscillations shown in the middle column of figure 7.5(a) are the *true* remnants of the inviscid critical layers.

The central locations of the critical layers in the middle column of figure 7.5(a), which we define as the centroid of the magnitude of $r\tilde{u}_r$, are nearly equal to the inviscid critical-layer singularity locations r_c, as estimated by setting $\mathrm{Im}(\sigma_c^\nu)$ to σ_c in (5.9). An important qualitative difference from the potential eigenmodes in figure 7.4 and the critical-layer eigenmodes is that in the radial regions outside the large amplitude oscillations, the viscous critical-layer eigenmodes decay monotonically, while the decay of the potential eigenmodes is highly oscillatory. Figure 7.5(b) shows two eigenmodes of the Batchelor vortex, which have similar eigenvalues (differing by only 6%). Their properties are similar to those of the eigenmode of the Lamb-Oseen vortex.

These numerical eigenmodes and eigenvalues exhibit good convergence with increasing M and are spatially resolved. For physical relevance, it is worthwhile to investigate their structures outside the remnant critical layers. By normalising the oscillation amplitude in the remnant critical layer to be of order unity, we can identify small-scale perturbation structures outside the critical layer of $O(10^{-5})$ or less. We note the similarity in shape of these small-scale perturbations to the inviscid critical-layer eigenmodes of similar $\mathrm{Im}(\sigma)$ (see the middle column of panels in figure 6.3), where each part in $(0, r_c)$ and (r_c, ∞) appears to be a scalar multiple of each side of the inviscid solutions (see §6.3). This is one indication that the viscous critical-layer eigenmodes are truly inherited from the inviscid critical-layer eigenmodes. Note that viscosity has a profound influence on the structure of the eigenmode at radial locations inside the remnant critical layer, where it locally regularises the critical layer's singularity, but viscosity has only marginal impact on the eigenmode at radial locations outside the remnant critical layer. Therefore, we expect the inviscid critical-layer eigenmodes (in figure 6.3) and the viscous critical-layer eigenmodes (in figure 7.5) to look similar in the regions outside the critical layer.

As can be seen in the viscous spectra, the decay rates in time of the viscous critical-layer eigenmodes are comparable to those of the viscous discrete eigenmodes, indicating that they can last for a relatively long time against viscous diffusion. Moreover, when comparing an

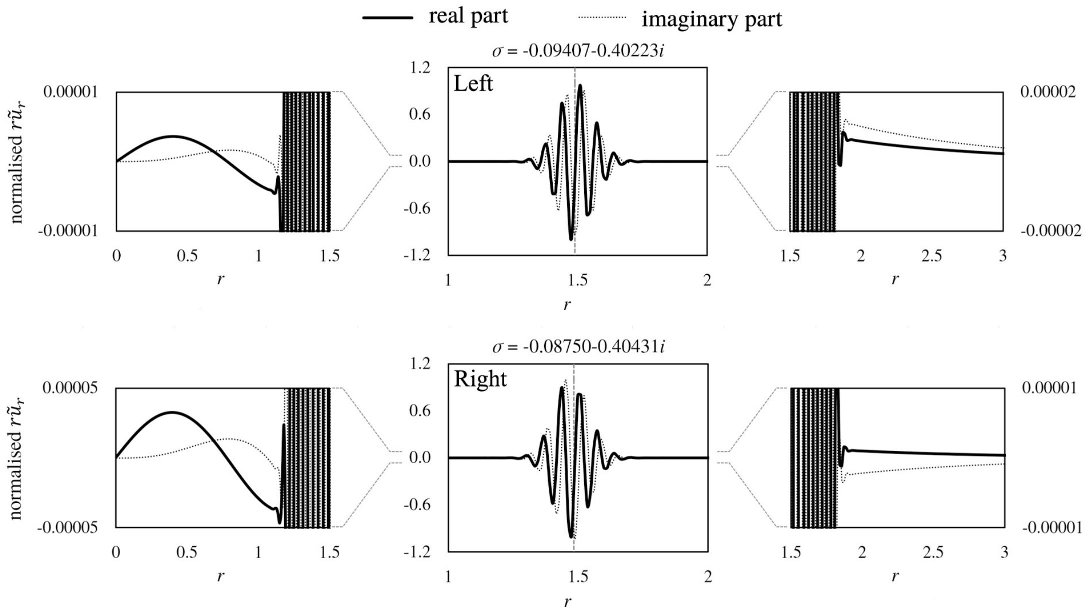

(a) (*m*, *κ*, *q*, *Re*) = (1, 1.0, ∞, 10^5)

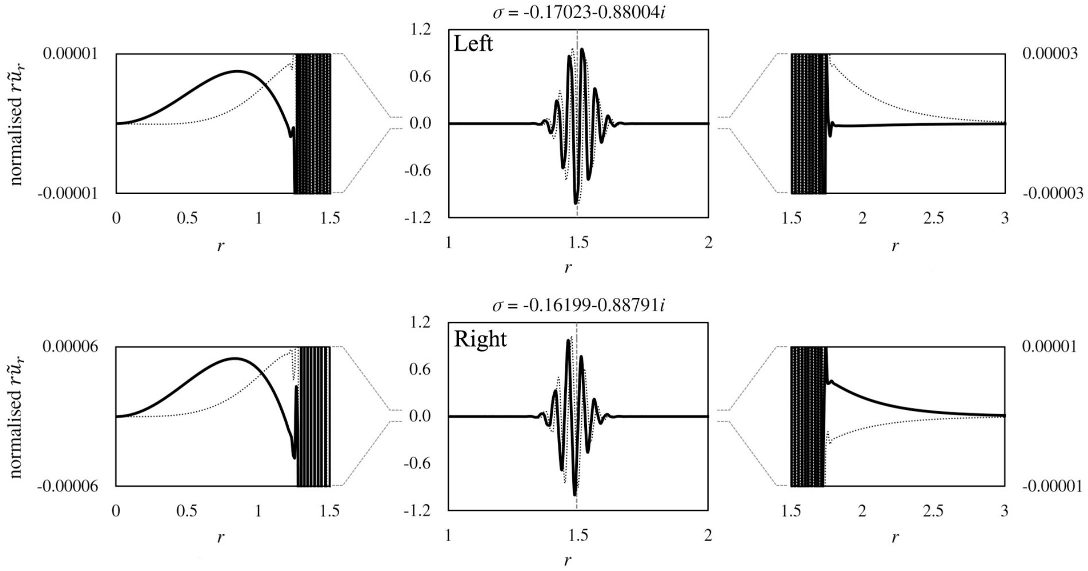

(b) (*m*, *κ*, *q*, *Re*) = (2, 3.0, 4.0, 10^5)

Figure 7.5: Two viscous critical-layer eigenmodes with nearly identical Im(σ). (*a*) Radial component of the velocity eigenmode of the Lamb-Oseen vortex ($q \to \infty$) with $(m, \kappa) = (1,\ 1.0)$ and (*b*) of the Batchelor vortex ($q = 4.0$) with $(m, \kappa) = (2,\ 3.0)$. The maximum of $\mathrm{Re}(r\tilde{u}_r)$ is normalised to unity. $M = 400$ and $L = 2.0$ are used. Each vertical dashed line indicates the location of the viscous critical layer estimated by setting Im(σ) equal to σ_c in (5.9). Those locations are nearly equal to the centroid of the magnitude of $r\tilde{u}_r$. Due to the similarity of the shape of small-amplitude structures in the right and left columns, where $r\tilde{u}_r \sim O(10^{-5})$, to the inviscid critical-layer eigenmodes (compare them with the middle column panels in figure 6.3(*a*) and (*b*), respectively), we hypothesise that these nearly degenerate viscous critical-layer eigenmodes are the viscous analogues of the inviscid two-fold degenerate critical-layer eigenmodes.

eigenmode in the left branch with another in the right branch of σ_c^ν, no notable structural difference is observed between them. This observation is further supported by the fact that these eigenmodes lie in the non-normal region. A more detailed analysis of the viscous critical-layer eigenmodes is presented later in this research, dealing with L and including the viscous remnant critical layers conforming to the $Re^{-1/3}$ scaling law (see §7.2) and the continuity of the viscous critical-layer spectrum σ_c^ν (see §7.4).

If σ_c^ν is the truly regularised descendant of σ_c^0 with the correct critical layer thickness, an important question that remains to be answered is how the spectrum of a single straight line bifurcates into two distinct branches. This bifurcation is physically meaningful because the separation of the branches, or equivalently the difference in $\mathrm{Re}(\sigma)$, is significantly larger compared to the extent of purely numerical error at the same level of M, such as the eigenvalue difference found in the pairing phenomenon in σ_c^0 (see figure 6.6). Recall that there exist numerous singular, degenerate eigenmodes associated with the same eigenvalue due to the critical-layer singularities in σ_c^0. We can infer that the viscous effect perturbs these two-fold degenerate singular eigenmodes and splits them into two regularised eigenmodes with marginally different eigenvalues. Hence, we expect that the emergence of σ_c^ν in two bifurcating curvy branches is not accidental but explicable by means of perturbation theory dealing with two-fold degeneracy (Sakurai & Napolitano, 2021, pp. 300-305).

It is worth discussing why σ_c^ν was not distinguished by previous researchers. When we compare our numerical method with that of Mao and Sherwin (2011) or Bölle *et al.* (2021), we see that they truncated the radial domain at a large but finite r and applied a homogeneous boundary condition there. In contrast, our method essentially involves the entire radial domain $0 \leq r < \infty$, and each basis function $P_{L_m}^n(r)$ obeys the boundary conditions that we want to apply. As a result, our truncated spectral sums, expanded by $P_{L_m}^n(r)$ as the basis elements of the Galerkin method, implicitly and exactly impose the boundary conditions on the solutions, regardless of the value of M used. However, the boundary condition at $r \to \infty$ is only approximately satisfied by the others. Considering the sensitivity of the numerical spectra to numerical errors (see §7.4.1), the truncation is likely to impede the numerical convergence of σ_c^ν because an approximate far-field radial boundary condition introduces errors. For instance, in the numerical spectrum plot provided by Mao and Sherwin (2011, p. 8), we can see *faint* traces of the two bifurcating branches at the location of σ_c^ν found in our results. Nonetheless, the results were substantially disturbed with respect to the radial truncation as well as the number of spectral elements, and the authors could not distinguish them from σ_p^ν.

7.2 Optimal choice of L to resolve the viscous critical layers

One of our goals is to accurately compute the viscous critical-layer modes. Clearly, we should use the largest M (with $N \equiv M + 2$) that our computational budget allows, which in this analysis is $M = 400$. We are interested in finding all of the viscous critical layer eigenmodes and eigenvalues, not just one, nor are we interested in finding them one-at-a-time. Unlike previous studies that looked at individual eigemmodes and stretched the radial domain locally around the location of that eigenmode's critical layer to maximise the resolution there (e.g., Le Dizès & Lacaze, 2005), our numerical method is designed for a fixed Re, m, and κ to compute the entire radial domain for all of the eigenmodes, regardless of the locations of their critical layers, using the same radial collocation points.

Choosing a small value of L is advantageous because the spatial resolution of our method is $\Delta = L/(M+2)$ (see (4.2.4)), and we need to have Δ smaller than the critical-layer thickness to resolve it. However, only half of the collocation points lie in the vast range between L and infinity, so eigenmodes with critical-layer radii with $r_c > L$ will have few collocation points (if any) within their critical layers and therefore be spatially under-resolved. The optimal value of L, denoted L_{opt}, must be a "Goldilocks" value: not too big or too small. Figure 7.6 demonstrates another reason why L_{opt} is a "Goldilocks" value. The figure displays the eigenvalues in the imaginary plane for $Re = 10^5$ with three different values of L. The left column of the figure represents a scenario where L is small, and viscous critical-layer eigenmodes with small r_c (and therefore large $|\sigma_c^\nu|$; see (5.9) - (5.10)) are spatially well-resolved. However, eigenmodes with small values of $|\sigma_c^\nu|$ and large r_c are not adequately resolved. The right column of the figure shows the case with a large L. In this case, only eigenmodes with small $|\sigma_c^\nu|$ and large r_c are well-resolved.

Nevertheless, figure 7.6 reveals another reason for the "Goldilocks" behaviour. The panels in the left column exhibit a clear separation between the potential eigenvalues σ_p^ν and the two new branches of viscous critical-layer eigenvalues σ_c^ν. As L increases, the potential eigenvalues shift towards the right in the complex plane (middle column). When L becomes sufficiently large, the potential eigenvalues become intertwined with those of the viscous critical-layer eigenmodes (right column), and the latter set of eigenmodes are no longer well-resolved spatially.

Upon detailed examination of the viscous critical-layer eigenmodes of the Lamb-Oseen vortex with $(m, \kappa) = (1, 1.0)$ and the Batchelor vortex with $(q = 4.0)$ and $(m, \kappa) = (2, 3.0)$, with $M = 400$ and $Re = 10^5$, we found that $\Delta = L/(M + 2)$ is just small enough to resolve the viscous critical-layer thicknesses when $L = 4.0$ and 2.5, respectively. Figure 7.6 illustrates that these values of L also represent the maximum values where the eigenvalues of the potential eigenmodes remain distinct from those of the viscous critical-layer eigenmodes. Thus, we believe that these values of L are the "Goldilocks" values: large enough to maximise the region $0 \leq r_c < L$, providing a sufficient number of collocation points to resolve the eigenmodes, and small enough that $\Delta = L/(M + 2)$ adequately resolves the critical-layer thicknesses. Our procedure for determining the optimal value L_{opt} is similar to how we found the optimal L for resolving the inviscid critical-layer eigenvalues σ_c^0 in § 6.2:

1. Start with L of order unity (i.e., the core radius of the unperturbed aircraft wake vortex), and increase L to expand the high-resolution region $0 \leq r_c < L$.

2. Stop increasing L just before the spatial resolution is so poor that the σ_p^ν and σ_c^ν eigenvalues intertwine as shown in the middle panels of figure 7.6.

7.3 Use of L_{opt} to find the scaling behavior of the critical layer thickness with *Re*

We hypothesise that the values of L at which the potential and viscous critical-layer eigenvalues intermingle in figure 7.6 and where $L/(M+2)$ just barely resolves the critical layer thickness are the same for all *Re*. We believe that the loss of numerical spatial resolution causes the two families of eigenvalues to become non-distinct from one another. To partially test this hypothesis, we calculate L_{opt} using the two-step procedure mentioned above, using the data in figure 7.6 and figure 7.7. We then assume that $\Delta_{\text{opt}} \equiv L_{\text{opt}}/(M+2)$ represents the critical layer thickness. Plotting Δ_{opt} as a function of *Re* in figure 7.8 demonstrates that the critical layer thickness (if our hypothesis is correct) scales approximately as $Re^{-1/3}$. This scaling agrees with previous analyses using asymptotic expansions (Maslowe, 1986; Le Dizès, 2004).

7.4 Continuity in the viscous critical-layer spectrum

7.4.1 Pseudospectral analysis

Finding the pseudospectra of the viscous operator $\mathbf{L}_{m\kappa}$, we can obtain evidence that the spectra σ_p^ν and σ_c^ν fill the continuous region in the complex σ-plane, as depicted in the schematic in figure 5.1. According to Mao and Sherwin (2011), the ε-pseudospectra around the potential and critical-layer eigenvalues seem to enclose the entire area when ε is small, as shown in figure 7.9. In addition, we present the ε-pseudospectrum with ε as small as 10^{-14}, which is much smaller than the values used by Mao and Sherwin (2011) or Bölle *et al.* (2021). Therefore, we believe that our observation provides strong empirical support for the continuity of the non-normal region that we have numerically resolved.

Furthermore, based on the alternative statement of the pseudospectra given by Trefethen and Embree (2005), any point in the ε-pseudospectra of $\mathbf{L}_{m\kappa}$ can be on the spectrum of $\mathbf{L}_{m\kappa}+\mathbf{E}$ for some small disturbance $\mathbf{E}$ where $\|\mathbf{E}\| < \varepsilon$. Since $\varepsilon = 10^{-14}$ is almost comparable to the double-precision machine arithmetic used in modern computing, one possible explanation for the random scattering of the numerical eigenvalues in the numerical representation of σ_p^ν is that they are perturbed by machine-dependent precision errors serving as $\mathbf{E}$.

As an aside, we observe that the ε-pseudospectrum of $\varepsilon = 10^{-2}$ protrudes into the right half-plane of the complex σ-plane, as shown in figure 7.9. It is well-known that the supremum of the real parts of $\sigma \in \sigma_\varepsilon(\mathbf{L}_{m\kappa})$, denoted α_ε and referred to as the ε-pseudospectral abscissa (Trefethen & Embree, 2005), is relevant to the lower bound of the maximum transient growth

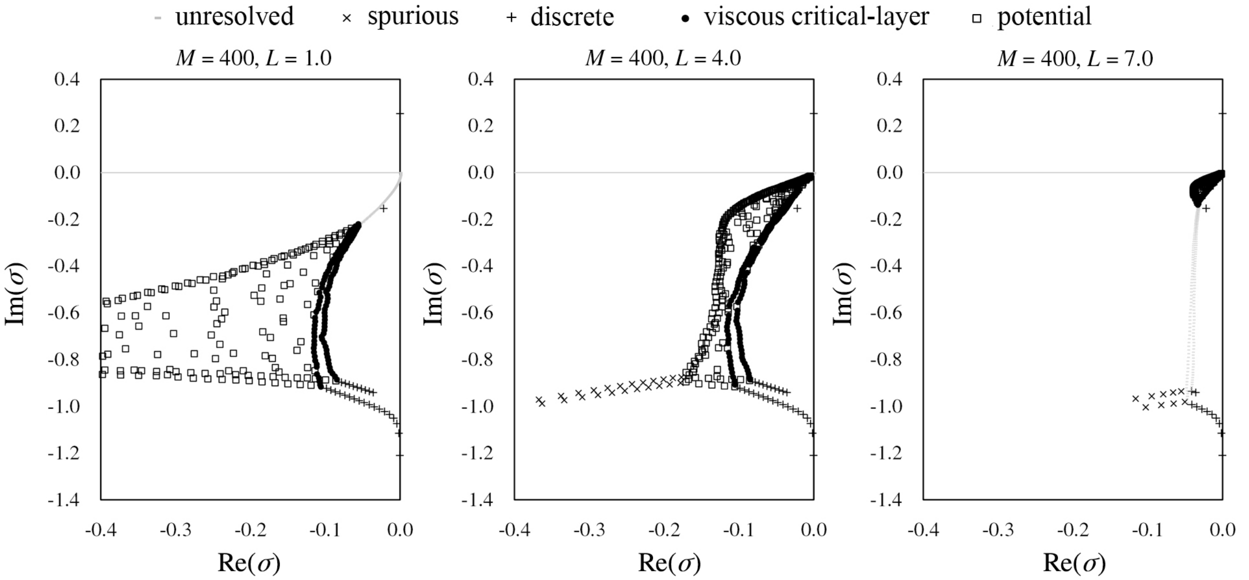

(a) $(m, \kappa, q, Re) = (1, 1.0, \infty, 10^5)$

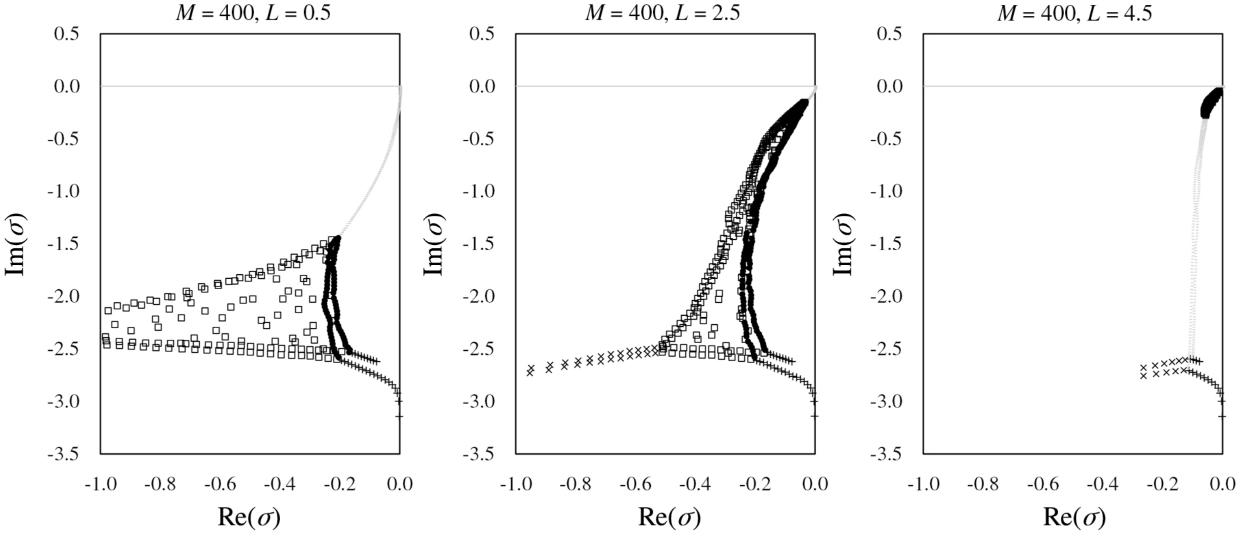

(b) $(m, \kappa, q, Re) = (2, 3.0, 4.0, 10^5)$

Figure 7.6: Changes of numerical viscous spectra (a) for the Lamb-Oseen vortex $(q \to \infty)$ in $(m, \kappa) = (1, 1.0)$ and (b) for the strong swirling Batchelor vortex $(q = 4.0)$ in $(m, \kappa) = (2, 3.0)$ with respect to three different L values. For animation, see movie 2. M is fixed at 400 and $N = M + 2$. If we aim to optimally resolve the critical-layer spectrum, we should appropriately tune L to find a balance between (left) the expansion of the high-resolution region $0 \leq r < L$, and (right) the deterioration of the overall resolution represented by $\Delta \sim O(L)$. The middle one shows the optimal L, denoted L_{opt}, which minimises the emergence of the numerical potential spectrum. Thus, most numerical eigenvalues in the non-normal region belong to the viscous critical-layer eigenvalues. See movie 2 (available at S. Lee & Marcus, 2023) for animation.

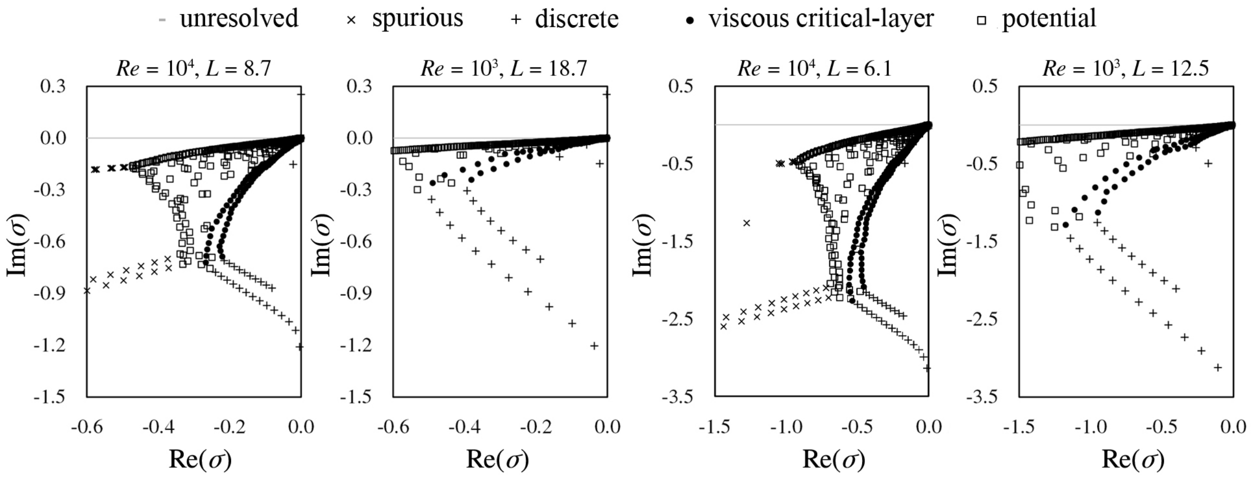

(a) $(m, \kappa, q) = (1, 1.0, \infty)$ *(b)* $(m, \kappa, q) = (2, 3.0, 4.0)$

Figure 7.7: Numerical viscous spectra with L_{opt} at $Re = 10^4$ and 10^3 (*a*) for the Lamb-Oseen vortex ($q \to \infty$) in $(m, \kappa) = (1, 1.0)$ and (*b*) for the strong swirling Batchelor vortex ($q = 4.0$) in $(m, \kappa) = (2, 3.0)$. M is fixed at 400 and $N = M + 2$.

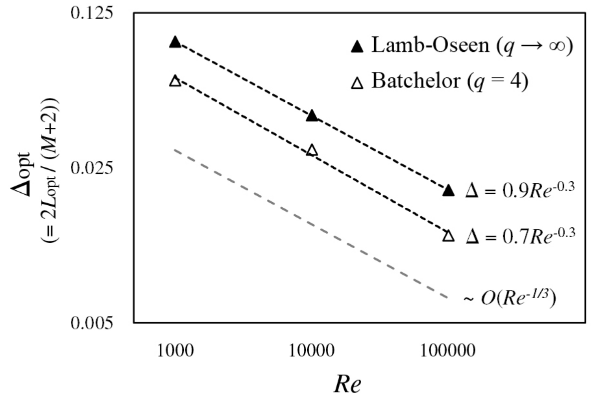

Figure 7.8: The optimal numerical resolution $\Delta_{\text{opt}} \equiv 2L_{\text{opt}}/(M+2)$, at the fixed $M = 400$, to resolve the critical-layer spectrum with respect to Re. The trend indicates $\Delta_{\text{opt}} \propto Re^{-1/3}$. The presented cases of $Re = 10^3$, 10^4 and 10^5 for each vortex can be found in figure 7.6 and figure 7.7.

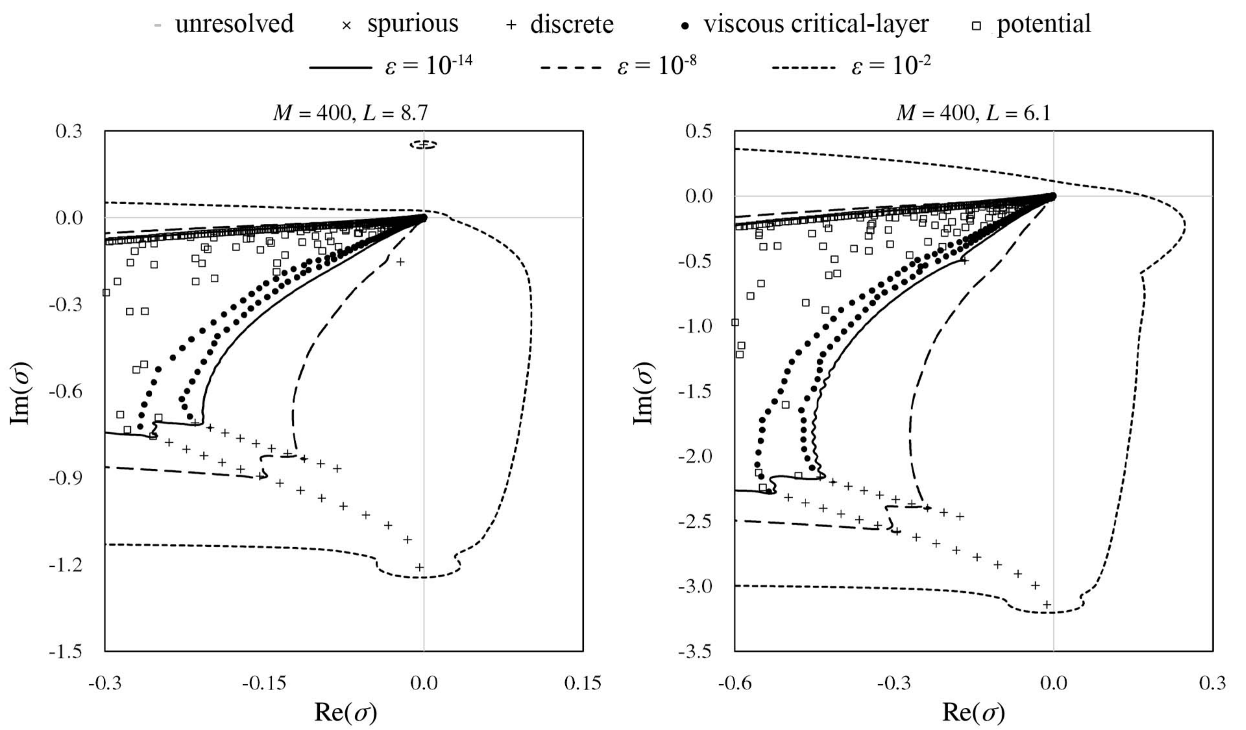

(a) $(m, \kappa, q, Re) = (1, 1.0, \infty, 10^4)$ *(b)* $(m, \kappa, q, Re) = (2, 3.0, 4.0, 10^4)$

Figure 7.9: ε-pseudospectrum bounds of $\varepsilon = 10^{-14}$, 10^{-8} and 10^{-2} with respecto to $\mathsf{L}_{m\kappa}$ at $Re = 10^4$ (a) for the Lamb-Oseen vortex ($q \to \infty$) in $(m, \kappa) = (1, 1.0)$ and (b) for the strong swirling Batchelor vortex ($q = 4.0$) in $(m, \kappa) = (2, 3.0)$. To construct the matrix, we use $M = 400$ and $N = M + 2$. L is optimally chosen. We can infer from their formation which part of the spectra is continuous and how big the maximum transient growth is.

of the stable system with an arbitrary initial state. of $\boldsymbol{x} = \boldsymbol{x}_0$ where $\|\boldsymbol{x}_0\| = 1$,

$$\frac{\partial \boldsymbol{x}}{\partial t} = \mathsf{L}_{m\kappa}\boldsymbol{x}. \tag{7.4.1}$$

The supremum of $\alpha_\varepsilon/\varepsilon$ in $\varepsilon > 0$ determines the lower bound of the maximum transient growth of the system (Apkarian & Noll, 2020), or

$$\sup_{t \geq 0} \left\| e^{\mathsf{L}_{m\kappa} t} \right\| \geq \sup_{\varepsilon > 0} \frac{\alpha_{\varepsilon(\mathsf{L}_{m\kappa})}}{\varepsilon}. \tag{7.4.2}$$

The fact that the ε-pseudospectral abscissa of $\varepsilon = 10^{-2}$ occurs in the frequency band coinciding with the critical-layer spectrum implies the significance of this spectrum in regards to the transient vortex growth, which needs more investigation in further studies.

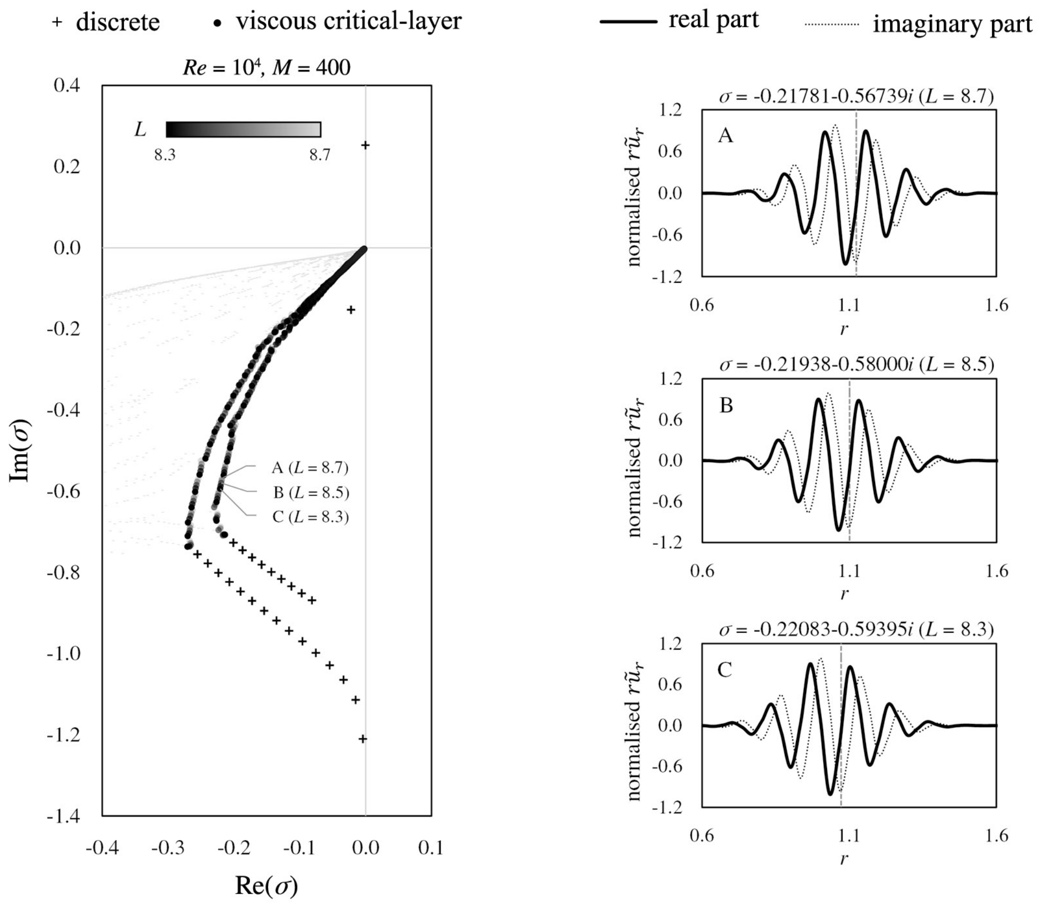

(a) Loci of the numerical spectra by fine-tuning *L*

(b) Numerical critical-layer eigenmodes varying marginally

Figure 7.10: (*a*) Loci of the numerical spectra for the Lamb-Oseen vortex ($q \to \infty$) in $(m, \kappa) = (1, 1.0)$ obtained by fine-tuning L from 8.3 to 8.7, where $Re = 10^4$, and (*b*) three viscous critical-layer eigenmodes that marginally vary, all of which are obtained from different L. Unlike the discrete spectrum that does not change with respect to L, the critical-layer spectrum is continuously filled by numerical eigenvalues associated with valid critical-layer eigenmodes.

7.4.2 Loci of the numerical spectra

One issue with pseudospectra is that they cannot provide non-normal eigenmodes corresponding to each eigenvalue point in the continuum. Instead, pseudomodes can be constructed in association with pseudospectra as an approximation of the eigenmodes, which were introduced and described by Trefethen and Embree (2005). Unfortunately, pseudomodes do not necessarily satisfy the exact governing equations and boundary conditions (see Mao & Sherwin, 2011, p. 11).

In our numerical method, it is possible to find critical-layer eigenmodes whose spatial structures continuously vary by fine-tuning L. Recalling the role of L (see §4), we know that it changes the entire $P_{L_m}^n(r)$ in the basis function set. If we replace L and solve the eigenvalue problem again, we can expect the eigenmodes generated from a new L not necessarily to be identical to the eigenmodes generated from an old L. Moreover, if this parametric change occurs in parts of the spectra where numerical convergence with respect to M is ensured, including σ_d^ν and σ_c^ν, the loci of them with respect to L should genuinely reflect the analytic spectra.

Based on the idea described above, we create the loci of the numerical spectra with respect to L for the Lamb-Oseen vortex case, where $(m,\ \kappa,\ q) = (1,\ 1.0,\ \infty)$ at $Re = 10^4$ in figure 7.10(a). To draw the loci, the viscous eigenvalue problem is solved multiple times with fine-tuning L from 8.3 to 8.7 with $M = 400$, where both σ_d^ν and σ_c^ν are found to be well-resolved. The other parts of the spectra, including σ_p^ν, are excluded due to no clear convergence with respect to M. That being said, we note that the loci of σ_p^ν with varying L sweep over the shaded area depicted in the schematic in figure 5.1.

As for σ_d^ν, its locus is completely invariant against changes in L. It makes sense because there is no chance to find an intermediate form of two discrete eigenmodes. The locus of σ_d^ν remaining discrete rather strengthens our method's robustness for any L. On the contrary, the locus of σ_c^ν is notably different from that of σ_d^ν; as L changes, the eigenvalue points on two branches of σ_c^ν also move and eventually fill in two distinct curves as in figure 5.1. In figure 7.10(b), it can be confirmed that the critical-layer eigenmodes with slightly different eigenvalues, having only a marginal difference in their spatial structures, are obtained from varying L. By comparing the two loci of σ_d^ν and σ_c^ν, we can conclude the continuity of the critical-layer spectrum.

For reference, we report the polynomial fitting results up to 6^{th} order of some loci of σ_c^ν among what we have explored. In the case $(m, \kappa, q) = (1, 1.0, \infty)$ at $Re = 10^4$, the left and right branches of σ_c^ν in the complex σ-plane are fitted as

$$\begin{aligned}\sigma_r = \ & -(1.905 \times 10^1) \cdot \sigma_i^6 - (4.562 \times 10^1) \cdot \sigma_i^5 - (4.138 \times 10^1) \cdot \sigma_i^4 \\ & -(1.741 \times 10^1) \cdot \sigma_i^3 - (2.761 \times 10^0) \cdot \sigma_i^2 + (5.348 \times 10^{-1}) \cdot \sigma_i,\end{aligned} \tag{7.4.3}$$

and

$$\begin{aligned}\sigma_r = \ & -(4.682 \times 10^0) \cdot \sigma_i^6 - (8.233 \times 10^0) \cdot \sigma_i^5 - (6.816 \times 10^0) \cdot \sigma_i^4 \\ & -(3.243 \times 10^0) \cdot \sigma_i^3 - (2.636 \times 10^{-1}) \cdot \sigma_i^2 + (6.108 \times 10^{-1}) \cdot \sigma_i,\end{aligned} \tag{7.4.4}$$

where σ_r and σ_i indicate the real and imaginary parts of σ, respectively. In the case $(m, \kappa, q) = (2, 3.0, 4.0)$ at $Re = 10^4$, the left and right branches of σ_c^ν are fitted as

$$\begin{aligned}\sigma_r = \ & + (1.071 \times 10^{-2}) \cdot \sigma_i^6 + (2.553 \times 10^{-2}) \cdot \sigma_i^5 - (9.022 \times 10^{-2}) \cdot \sigma_i^4 \\ & - (3.417 \times 10^{-1}) \cdot \sigma_i^3 - (1.906 \times 10^{-1}) \cdot \sigma_i^2 + (4.764 \times 10^{-1}) \cdot \sigma_i,\end{aligned} \tag{7.4.5}$$

and

$$\begin{aligned}\sigma_r = \ & + (7.098 \times 10^{-2}) \cdot \sigma_i^6 + (4.052 \times 10^{-1}) \cdot \sigma_i^5 + (8.111 \times 10^{-1}) \cdot \sigma_i^4 \\ & + (6.323 \times 10^{-1}) \cdot \sigma_i^3 + (2.508 \times 10^{-1}) \cdot \sigma_i^2 + (4.833 \times 10^{-1}) \cdot \sigma_i.\end{aligned} \tag{7.4.6}$$

We will work on the analytic formulation of σ_c^ν to better understand the bifurcation in future studies. These fitting forms will be considered for comparison and validation.

Chapter 8

Concluding remarks I

In this part of study, we proposed a numerical method that is capable of computing eigenmodes and eigenvalues for linear stability analyses of aircraft wake vortices with high time-efficiency and accuracy compared to previous studies. Also, we established a means of unambiguously verifying whether the numerically computed eigenmodes and eigenvalues are physical, spatially resolved, or spurious.

We developed a numerical method for the linear stability analysis of aircraft wake vortices, and applied this method to the q-vortex model, which is a non-dimensional vortex model that portrays the Lamb-Oseen or Batchelor vortices, used as the base vortex profile. Our numerical method employs algebraically mapped associated Legendre functions $P_{L_m}^{n}(r)$, defined in (2.2.1), as Galerkin basis functions for the spectral expansion of functions in a radially unbounded domain. We found these basis functions to be suitable as they capture the correct boundary conditions, including analyticity at the origin and rapid decay in the far field. By applying the poloidal-toroidal decomposition to the linearised governing equations, we reduced the problem size for computation while preserving the spatial order of the equations. Furthermore, we believe that our numerical method is preferable for linear analyses of vortex dynamics for the following reasons.

1. Our method, the mapped Legendre spectral collocation method, converts the original vortex stability problem into a standard matrix eigenvalue problem of toroidal and poloidal streamfunctions. In comparison to other methods that lead to a generalised matrix eigenvalue problem of primitive variables, our method effectively reduces the number of state variables of the problem from four to two, and the number of matrices constructed for eigenvalue computation from two to one.

2. Our method does not require extra treatments for analyticity and boundary conditions in a radially unbounded domain. The use of toroidal and poloidal streamfunctions expanded by $P_{L_n}^{m}(r)$ guarantees that computed linear perturbation velocity fields are analytic at $r = 0$ and decay to zero as $r \to \infty$. This prevents artificial interference in the problem, such as truncation of the radial domain and imposition of artificial boundary conditions at the point of truncation, which likely cause unnecessary numerical errors.

3. Our method allocates collocation points properly around the vortex core, ensuring that half of them remain within the high-resolution region of $0 \leq r < L$ while the other half contribute to sustaining the domain's unboundedness, where L is the map parameter of associated Legendre functions. In comparison to the numerical method proposed by Mayer and Powell (1992), our method requires about three times fewer radial basis elements, which is expected to result in roughly ten times greater efficiency in terms of computing time. Moreover, L offers an additional degree of computational freedom, enabling us to adjust the spatial resolution without requiring extra computing resources to match the smallest radial length scale to be resolved.

We numerically computed eigenmodes and eigenvalue spectra with azimuthal and axial wavenumbers of order unity for strong swirling q-vortices, and classified these eigenmodes and eigenvalue spectra into different families based on the criteria outlined in §2.3, which determine whether they are physical, spatially resolved, or spurious. Some family, such as the *freestream* family which do not decay at radial infinity, were beyond the scope of our analysis as we considered such non-vanishing solutions to be non-physical. For this reason, our method only calculates solutions that decay to zero. Our main focus was on physical eigenmodes that exist in the real world, i.e., those that can destabilise an aircraft wake vortex, with greater emphasis on critical layers. In this regard, we identified the following important families of eigenmodes and eigenvalue spectra, some of which we believe we distinguished for the first time.

1. *Discrete family* (see §6.1.1 and §7.1.1). They consist of entirely regular solutions to the linearised governing equations. Each of their eigenvalues is discrete, and approaches a fixed point as the number of spectral basis elements M increases. The eigenmodes are characterised by "wiggles" around the vortex core, and monotonically rapid decay in the r direction. All spatially resolved eigenmodes with small but finite viscosity are found to have their respective inviscid counterparts, exhibiting only marginal changes in their spatial structures. Without doubt, this family are physical.

2. *Inviscid critical-layer family* (see §6.1.2). The analytic presence of their spectrum on the imaginary axis arises from mathematical point singularities, which are given in (5.9). Although the eigenmodes possess a critical-layer singularity, our numerical method yields well-behaved spatial structures outside the neighbourhood of the singularity when using a sufficiently large value of M. These structures are crucial for identifying the remnants of this family after adding small viscosity. However, their singular nature often causes the eigenmodes to be under-resolved, i.e., to have incorrect eigenvalues out of the imaginary axis, leading to a misjudgement of the wake vortex's linear instability. Adjusting the map parameter L can help correct these errors so that the numerical spectrum reflects its analytic ground-truth (see §6.2). In the corrected inviscid critical-layer spectrum, eigenvalues tend to emerge in pairs. This phenomenon is understood as a marginal separation caused by numerical errors of two singular de-

generate critical-layer eigensolutions, whose exact eigenvalues are supposed to be the same (see §6.3).

3. *Potential family* (see §7.1.3), which were first proposed by Mao and Sherwin (2011). Bölle *et al.* (2021, p. 17) suggested this family be the viscous remnants of the inviscid critical-layer spectrum. The spectrum is supposed to fill continuously a portion of the left half of the complex eigenvalue plane, as depicted in the schematic in figure 5.1. Its discretised representation can be found in our method through an area with randomly scattered numerical eigenvalues that keeps stretching out to the left as M increases. We cannot establish the convergence of a particular eigenvalue to a fixed point due to the continuous nature of the spectrum. The random scattering makes it impossible to find a clear correspondence between the eigenvalue computed with $M+1$ basis elements and another computed with M basis elements. Nevertheless, the eigenmodes are spatially resolved enough to identify their common spatial characteristics. They are typified by local rapid oscillations ("wavepackets") around the corresponding critical-layer radius, estimated by setting the imaginary part of their respective eigenvalues to (5.9). This implies that they stem from the viscous regularisation of the inviscid critical layers. Considering their uninteresting near-zero region outside the respective "wavepackets" together, we deem these eigenmodes to be physical. Nonetheless, the fact that their "wavepackets" can have varying widths even at the same Re raises concern about the absence of a scaling relationship between wavepacket widths and Re. Moreover, their slow and oscillatory decaying behaviour does not resemble the inviscid critical-layer eigenmodes' rapid and monotonous decaying behaviour (see §6.1.2). Unlike the suggestion by Bölle *et al.* (2021), we argue that they do not represent the *true* viscous remnants of the inviscid critical-layer family. The *true* viscous remnants mean that they not only originate from the viscous regularisation but also exhibit spatial similarity to the inviscid critical-layer eigenmodes, in compliance with the $Re^{-1/3}$ scaling law for critical layers.

4. *Viscous critical-layer family* (see §7.1.4), which are believed to be distinguished for the first time. As the name suggests, we argue that this family is the *true* viscous remnants of the inviscid critical-layer spectrum. The spectrum of this family is identified near the right end of the potential spectrum as two distinct continuous curves. It shows good numerical convergence with respect to M, and their continuous loci are confirmed by fine-tuning L (see §7.4). When spatially resolved, these eigenmodes exhibit thin and distinct local rapid oscillations at the inviscid critical-layer singularity radius as estimated above. This implies their origination from the viscous regularisation of the inviscid critical layers, as with the potential family. However, unlike the potential family, they are not only considered physical but also thought of as the *true* viscous remnants of the inviscid critical-layer spectrum for the following reasons. First, the similarity in spatial structure to the corresponding inviscid critical-layer eigenmode is noticeable in the regions outside the critical layer. Second, the optimal resolution

required to numerically compute the viscous critical-layer eigenmodes as many as possible is defined (see §7.2), providing a measure of the numerical resolution necessary to resolve the viscous critical-layer family overall. This optimal numerical resolution is found to be scaled in the order of $Re^{-1/3}$.

The bifurcation of the viscous critical-layer spectrum has remained an unanswered question yet. This will be analytically examined based on our conjecture that viscosity breaks the singular degeneracies, which are numerically shown as the pairing phenomenon in the inviscid critical-layer spectrum.

Part II

Transient Growth Analysis

Chapter 9

Transient growth of a wake vortex

Nota bene
For those who are specifically interested in this part, a separate preprint is available online as of this writing (see S. Lee & Marcus, 2024). As noted in the preceding part, the dissertation synthesises various aspects of topics related to wake vortex motion for the sake of comprehensively exploring the early-time growth of a wake vortex.

9.1 Background

Wake vortex following an aircraft is widely recognised for its long-lived presence over time, which has made it a significant focus of aerodynamic research. It holds importance, particularly in comprehending the mechanisms behind its decay process. Rapid destruction of the wake vortices is deemed beneficial in several aspects, including enhancing air traffic safety by mitigating wake-related hazards and improving airport operation efficiency by reducing intervals between aircraft during take-off and landing on the same runway (Spalart, 1998; Hallock & Holzäpfel, 2018). Not only that, but wake vortices also contribute to the development of condensation trails (or contrails), whose impact on climate change via radiative forcing has been being actively assessed (e.g., Schumann, 2005; Naiman *et al.*, 2011; D. S. Lee *et al.*, 2021), by capturing the jet exhaust particles around the low-pressure vortex core, facilitating the formation of ice crystals. The early demise of wake vortices may impede early contrail development and, as a result, potentially influence its subsequent climate impact.

There are several factors influencing the decay process of the wake vortex, such as stratification (Sarpkaya, 1983), ground effect (Proctor *et al.*, 2000), and various surrounding factors (see Hallock & Holzäpfel, 2018, p. 30). Above all, the activation of wake vortex instability typically provides the dominant route to effective vortex breakup. Classical wake vortex instability mechanisms were investigated under the typical counter-rotating vortex pair configuration for aircraft trailing vortices (Crow, 1970; Moore & Saffman, 1975; Tsai & Widnall, 1976), where one vortex is 'disturbed' by the strain created by the other vortex. If there exists an infinitesimal perturbation (or eigenmode) of the base vortex profile with a positive real growth rate (or eigenvalue), the perturbation may be activated by atmospheric turbulence (e.g., Crow & Bate, 1976) and grow exponentially in time until nonlinear dynamics govern, eventually resulting in the linkage of the two vortices. In this aspect, the growth is evidenced by the presence of an unstable eigenmode that is a solution to the Navier-Stokes or Euler equations linearised on the base vortex profile, which is often referred to as linear instability analysis.

However, when it comes to an 'undisturbed' wake vortex (i.e., a vortex without the influence of nearby vortices), typically modelled as the Batchelor vortex (Batchelor, 1964), the linear instability analysis usually ends up with stable configuration. In most of the inviscid cases, the vortex is found to be linearly neutrally stable unless it accompanies a strong axial velocity component (Leibovich & Stewartson, 1983; Stewartson & Brown, 1985; Heaton, 2007a). Several experiments have supported that the axial velocity of the wake vortex in reality is not strong enough to match the prediction from the analysis (e.g., Leibovich, 1978; Fabre & Jacquin, 2004). With viscosity, Fabre and Jacquin (2004) demonstrated the viscous instability of centre-modes even with a non-strong axial velocity, whose major spatial structure was concentrated at the vortex centre. However, this instability is weak (Heaton, 2007b, p. 496) and the authors also left cautions about the practicality of this instability due to the lack of knowledge about the exact properties of the centre of real trailing vortices. In many cases, the role of viscosity for the majority of eigenmodes has been believed to be close to stabilisation rather than destabilisation (see Khorrami, 1991, p. 198).

To unravel the early development of a single vortex, various approaches have been successfully employed to some extent. One approach is the analysis of resonant triad instability (RTI), which focuses on instability resulting from the resonance of two secondary modes due to the primary mode serving as a disturbance to the vortex (e.g., Mahalov, 1993; Wang *et al.*, 2024). In the context of vortex stability, the RTI mechanism is essentially a generalised version of the elliptical instability (Moore & Saffman, 1975; Tsai & Widnall, 1976), where the primary disturbance is the strain caused by the neighboring vortex. Another approach is transient growth analysis, which explores an optimal initial perturbation (usually as a sum of eigenmodes) that may exhibit large energy growth at finite times, even though it vanishes asymptotically as time approaches infinity (e.g., Schmid & Henningson, 1994; Heaton, 2007b; Mao & Sherwin, 2012; Navrose *et al.*, 2018). This transient behaviour is expected due to the non-normality of the linearised Euler or Navier-Stokes operator, which yields families of continuously varying eigenmodes (Mao & Sherwin, 2011; S. Lee & Marcus, 2023). Several studies have examined the application of transient growth in the context of vortices with axial flows (Heaton & Peake, 2007; Mao & Sherwin, 2012) or, similarly, jets with swirling flows (Muthiah & Samanta, 2018), emphasising the role of continuous eigenmodes.

9.2 Research Goals

In this research, we dig into more details of transient growth of wake vortices under regular conditions, in addition to revisiting the previous discovery. In a non-zero viscosity regime with physical relevance, the continuous eigenmodes are further categorised into different families. Therefore, an important question arises: Which family of continuous eigenmodes makes the dominant contribution to optimal perturbations for transient growth – the potential family (Mao & Sherwin, 2011), the viscous critical-layer family (S. Lee & Marcus, 2023), or both equally? The question, which we will primarily address in this research, provides guidance on which continuous eigenmode family should be the specific focus, avoiding the exploration of the entire region of possibilities.

Subsequently, another crucial aspect to consider is that the numerically resolvable portion of continuous eigenmodes depends on the discretisation scheme of the method in use. Thus, addressing the question above also offers insights into the proper methodology for addressing the current type of problems. In the literature, Chebyshev spectral collocation methods have been preferred for the wake vortex stability problem e.g., Ash and Khorrami, 1995, pp. 354-357. On the other hand, S. Lee and Marcus (2023) suggested the mapped Legendre spectral collocation method and successfully distinguished the viscous critical-layer family for the first time, despite its similarity in appearance to the potential one. Here, we extend the use of the mapped Legendre spectral collocation method to transient growth analysis of wake vortices so as to demonstrate its competitiveness, especially in solving radially unbounded swirling flow problems.

Finally, we consider ice particles as a source of initiating optimal perturbations at the early stage of vortex development towards the transient growth process. Based on computational fluid dynamics (CFD), the interaction between the jet and the vortex during the early stage of a trailing vortex has been studied in terms of contrail development, typically associated with ice microphysics (Lewellen & Lewellen, 2001; Paoli & Garnier, 2005; Shirgaonkar, 2007; Naiman *et al.*, 2011). However, to the best of the authors' knowledge, the backward impact of jet exhaust (or simply ice) particles on the short-term wake vortex development has not been clearly established, despite its potential significance. Particle drag may disturb the vortex out of the core in a short time if the particles are clustered during jet entrainment around the vortex core, presumably leading to a temporarily large-growing perturbation known to be structured at the periphery of the vortex core (Mao & Sherwin, 2012, p. 43). In jet exhaust, each particle's size can grow only up to a few microns during the early stage. However, the total particle number density is reported to be large (10^9 per cubic metre to 10^{11} per cubic metre) (Paoli *et al.*, 2004; Paoli & Garnier, 2005). This can make their bulk effect with respect to momentum exchange non-negligible. This study is the first step to investigate the role of the particle concentration nearby the vortex in the initiation of transient growth.

The remainder of this part, from §10 to §13, is structured as follows. In §10, the essence of the linear stability analysis of wake vortices is revisited (S. Lee & Marcus, 2023) and then incorporated into a transient growth analysis. In §11, the optimal perturbation structures acquired from the analysis are revealed, determining the continuous eigenmode family that takes dominant contribution. In §12, we examine the initiation of the optimal perturbations via inertial particles near the vortex. In §13, our overall findings are presented with a conclusion.

Chapter 10

Transient growth formalism

10.1 Formulation

We briefly revisit the gist of the linear stability analysis of wake vortices by S. Lee and Marcus (2023), and then incorporate it into a transient growth analysis. Unless specified, we use the cylindrical coordinate system (r, ϕ, z) and all variables are presented in a non-dimensional form with respect to the characteristic length and velocity scales, R_0 and U_0, detailed by Lessen *et al.* (1974, p. 755) and the fluid density ρ. The base flow velocity profile $\overline{\boldsymbol{U}}$ is the Batchelor vortex (Batchelor, 1964), or the q-vortex in the non-dimensional form, given by

$$\overline{\boldsymbol{U}}(r) = \left(\frac{1 - e^{-r^2}}{r} \right) \hat{\boldsymbol{e}}_\phi + \left(\frac{1}{q} e^{-r^2} \right) \hat{\boldsymbol{e}}_z, \tag{10.1.1}$$

where q is a swirl parameter that determines the relative strength of swirling. The vortex core region is defined by the radial location where the azimuthal velocity component is maximised, which is $r \leq 1.12$.

The governing equations of fluid motion assume Newtonian fluid with constant density ρ and constant kinematic viscosity ν. In terms of the total velocity $\boldsymbol{u} \equiv u_r \hat{\boldsymbol{e}}_r + u_\phi \hat{\boldsymbol{e}}_\phi + u_z \hat{\boldsymbol{e}}_z$ and the total specific energy $\varphi \equiv (\boldsymbol{u} \cdot \boldsymbol{u})/2 + p$, where p denotes the total pressure (which is non-dimensionalised by ρU_0^2), they are written as

$$\frac{\partial \boldsymbol{u}}{\partial t} = -\boldsymbol{\nabla} \varphi + \boldsymbol{u} \times \boldsymbol{\omega} + \frac{1}{Re} \nabla^2 \boldsymbol{u} \quad \text{with } \boldsymbol{\nabla} \cdot \boldsymbol{u} = 0, \tag{10.1.2}$$

where $\boldsymbol{\omega} \equiv \boldsymbol{\nabla} \times \boldsymbol{u}$ is the total vorticity, and $Re \equiv U_0 R_0 / \nu$ is the Reynolds number. We then linearise the equations on the base flow profile by decomposing $\boldsymbol{u}$ and p into the base terms (indicated with overbars $\overline{*}$) and the perturbations (indicated with primes $*'$), and we apply the toroidal-poloidal decomposition using $\hat{\boldsymbol{e}}_z$ as a reference vector to reach the following form:

$$\frac{\partial}{\partial t} \begin{pmatrix} \psi' \\ \chi' \end{pmatrix} = \mathbb{P}\big(\overline{\boldsymbol{U}}(r) \times \boldsymbol{\omega}'\big) - \mathbb{P}\big(\overline{\boldsymbol{\omega}}(r) \times \boldsymbol{u}'\big) + \frac{1}{Re} \nabla^2 \begin{pmatrix} \psi' \\ \chi' \end{pmatrix}, \tag{10.1.3}$$

where $\psi'(r,\phi,z,t)$ and $\chi'(r,\phi,z,t)$ are the toroidal and poloidal streamfunctions of $\boldsymbol{u}'(r,\phi,z,t)$, respectively, and $\mathbb{P}$ indicates an operator that takes a smooth vector field as input and outputs its toroidal and poloidal scalar components. If the input vector field is solenoidal, then $\mathbb{P}$ is invertible. That is to say, $\mathbb{P}(\boldsymbol{u}') = (\psi',\ \chi')$ and $\boldsymbol{u}'$ is uniquely reconstructed from $(\psi',\ \chi')$ (for more details see S. Lee & Marcus, 2023, pp. 9-11). Thus, (10.1.3) only has two state variables: ψ' and χ'. These reduced linearised governing equations are beneficial to imposing the analyticity constraint at $r = 0$ as each state variable is treated independently of one another without coupling.

If we introduce the Fourier ansatz (indicated with tildes $\tilde{*}$) of the azimuthal and axial wavenumbers $m \in \mathbb{Z}$, $\kappa \in \mathbb{R} \setminus \{0\}$, i.e.,

$$\begin{pmatrix} \psi' \\ \chi' \end{pmatrix} = \begin{pmatrix} \tilde{\psi}(r,t) \\ \tilde{\chi}(r,t) \end{pmatrix} e^{\mathrm{i}(m\phi+\kappa z)}, \tag{10.1.4}$$

(10.1.3) further reduces to the spatially one-dimensional form expressed as

$$\frac{\partial \tilde{\boldsymbol{\wp}}}{\partial t} = \mathcal{L}^{\nu}_{m\kappa}(\tilde{\boldsymbol{\wp}}), \tag{10.1.5}$$

where $\tilde{\boldsymbol{\wp}}(r,t) \equiv (\tilde{\psi}(r,t),\ \tilde{\chi}(r,t))$ is the toroidal-poloidal streamfunction set (equivalent to its corresponding velocity Fourier ansatz $\tilde{\boldsymbol{u}}(r,t)e^{\mathrm{i}(m\phi+\kappa z)}$) and $\mathcal{L}^{\nu}_{m\kappa}$ is the linear operator with respect to $\tilde{\boldsymbol{\wp}}$ which represents the right-hand side of (10.1.3) with the incorporation of (10.1.4). Note that the operator varies with the wavenumbers m and κ and the Reynolds number Re, as indicated by the subscript and the superscript.

To obtain physically meaningful solutions to (10.1.5) in an unbounded domain ($0 \le r < \infty$), the analyticity at the origin and the rapid decay condition as $r \to \infty$ are required. The most prevalent discretisation schemes for computing the solutions have been Chebyshev spectral collocation methods (e.g., Ash & Khorrami, 1995; Antkowiak & Brancher, 2004; Fontane *et al.*, 2008; Mao & Sherwin, 2011; Muthiah & Samanta, 2018) despite their bounded domain of two closed ends, demanding the approximation of the above constraints. In contrast, the mapped Legendre spectral collocation method, described by S. Lee and Marcus (2023), is fundamentally designed for unbounded domains while accurately satisfying the constraints without additional treatments. Given the problem is discretised by either method, we have

$$\frac{d\tilde{\boldsymbol{\varrho}}}{dt} = \mathsf{L}^{\nu}_{m\kappa}\tilde{\boldsymbol{\varrho}}, \tag{10.1.6}$$

where $\tilde{\boldsymbol{\varrho}}(t)$ is the discretised version of $\tilde{\boldsymbol{\wp}}(r,t)$ in spectral space, consisting of the spectral coefficients of $\tilde{\psi}$ and $\tilde{\chi}$ in order, and $\mathsf{L}^{\nu}_{m\kappa}$ is the matrix expression of $\mathcal{L}^{\nu}_{m\kappa}$.

Similarly, we define the discretised version of $\tilde{\boldsymbol{u}}(r,t)$ as $\tilde{\boldsymbol{v}}(t)$ in physical space, consisting of the collocated values of $\tilde{u}_r$, $\tilde{u}_\phi$ and $\tilde{u}_z$ in order. The conversion between $\tilde{\boldsymbol{\varrho}}$ and $\tilde{\boldsymbol{v}}$ is possible through the matrix expression of $\mathbb{P}$, denoted P, whose construction scheme based on the mapped Legendre spectral collocation method can be found in Matsushima and Marcus (1997, pp. 330-333). We use the following notations: $\tilde{\boldsymbol{\varrho}} = \mathsf{P}^{\dagger}\tilde{\boldsymbol{v}}$ and $\tilde{\boldsymbol{v}} = \mathsf{P}\tilde{\boldsymbol{\varrho}}$. Under the solenoidal velocity assumption, we may treat both $\mathbf{P}^\dagger\mathbf{P}$ and $\mathbf{P}\mathbf{P}^\dagger$ as an identity map. Now we define the 'energy' E of a velocity Fourier ansatz $\tilde{\boldsymbol{u}}(r,t)e^{\mathrm{i}(m\phi+\kappa z)}$ as

$$E(\tilde{\boldsymbol{u}}) \equiv \int_0^\infty \left(\tilde{u}_r^*\tilde{u}_r + \tilde{u}_\phi^*\tilde{u}_\phi + \tilde{u}_z^*\tilde{u}_z\right) rdr. \tag{10.1.7}$$

A similar usage can be found in Mao and Sherwin (2012). Using numerical integration, e.g., a quadrature rule, $E(\tilde{\boldsymbol{u}})$ may be expressed as

$$E(\tilde{\boldsymbol{u}}) = \tilde{\boldsymbol{v}}^*\mathbf{M}\tilde{\boldsymbol{v}} = \tilde{\boldsymbol{\varrho}}^*\mathbf{P}^*\mathbf{M}\mathbf{P}\tilde{\boldsymbol{\varrho}}, \tag{10.1.8}$$

where $\mathbf{M}$ represents the numerical integration form of (10.1.7). A specific example of $\mathbf{M}$ using the Gauss-Legendre quadrature rule is given in Appendix C.

At last, we apply the transient growth formalism (Schmid & Henningson, 2001; Mao & Sherwin, 2012; Muthiah & Samanta, 2018) in order to complete our formulation. Consider a set (or subset) of eigenmodes of $\mathbf{L}_{m\kappa}^{\nu}$ containing p elements $\{\tilde{\boldsymbol{\varrho}}_1,\ \tilde{\boldsymbol{\varrho}}_2, \cdots,\ \tilde{\boldsymbol{\varrho}}_p\}$, which correspond to eigenvalues $\{\sigma_1,\ \sigma_2, \cdots,\ \sigma_p\} \subset \mathbb{C}$, respectively. Assuming that $\tilde{\boldsymbol{\varrho}}$ belongs to the eigenspace where all elements are spanned by these p eigenmodes, i.e.,

$$\tilde{\boldsymbol{\varrho}}(t) = \sum_{k=1}^{p} \tilde{\xi}_k e^{\sigma_k t}\tilde{\boldsymbol{\varrho}}_k, \tag{10.1.9}$$

we use a new vector $\tilde{\boldsymbol{\xi}}_0 \equiv (\tilde{\xi}_1, \tilde{\xi}_2, \cdots, \tilde{\xi}_p) \in \mathbb{C}^p$ to represent $\tilde{\boldsymbol{\varrho}}$. For instance, at time $t=\tau$, $\tilde{\boldsymbol{\varrho}}(\tau)$ corresponds to $\exp(\tau\mathbf{S})\tilde{\boldsymbol{\xi}}_0$, where $\mathbf{S} \equiv \mathrm{diag}(\sigma_1, \sigma_2, \cdots, \sigma_p)$. In order to focus on the transient growth process, the chosen eigenmodes are supposed to be asymptotically stable in time ($\mathrm{Re}(\sigma_k) < 0$), which mostly holds true for strong swirling q-vortices. By defining $\mathbf{V} \equiv \left(\ \tilde{\boldsymbol{\varrho}}_1 \ \vdots\ \tilde{\boldsymbol{\varrho}}_2 \ \vdots\ \cdots \ \vdots\ \tilde{\boldsymbol{\varrho}}_p\ \right)$, (10.1.9) at time $t=\tau$ becomes

$$\tilde{\boldsymbol{\varrho}}(\tau) = \mathbf{V}\exp(\tau\mathbf{S})\tilde{\boldsymbol{\xi}}_0, \tag{10.1.10}$$

and applying it to (10.1.8) yields the energy formula using the following ℓ^2 norm:

$$\begin{aligned} E(\tilde{\boldsymbol{u}}(\tau)) &= \tilde{\boldsymbol{\xi}}_0^*\exp(\tau\mathbf{S}^*)\mathbf{V}^*\mathbf{P}^*\mathbf{M}\mathbf{P}\mathbf{V}\exp(\tau\mathbf{S})\tilde{\boldsymbol{\xi}}_0 \\ &= \left\|\mathbf{F}\exp(\tau\mathbf{S})\tilde{\boldsymbol{\xi}}_0\right\|_2^2, \end{aligned} \tag{10.1.11}$$

where the matrix $\mathbf{F}$ is provided through $\mathbf{F}^*\mathbf{F} = \mathbf{V}^*\mathbf{P}^*\mathbf{M}\mathbf{P}\mathbf{V}$. The maximum energy growth G, determining the optimal perturbations under the transient growth formalism, at time $t=\tau$ is then obtained as

$$\begin{aligned} G(\tau) \equiv \sup_{\tilde{\boldsymbol{u}}(0)\neq\mathbf{0}} \frac{E(\tilde{\boldsymbol{u}}(\tau))}{E(\tilde{\boldsymbol{u}}(0))} &= \sup_{\tilde{\boldsymbol{\xi}}_0\neq\mathbf{0}} \frac{\left\|\mathbf{F}\exp(\tau\mathbf{S})\tilde{\boldsymbol{\xi}}_0\right\|_2^2}{\left\|\mathbf{F}\tilde{\boldsymbol{\xi}}_0\right\|_2^2} \\ &= \left\|\mathbf{F}\exp(\tau\mathbf{S})\mathbf{F}^{-1}\right\|_2^2. \end{aligned} \tag{10.1.12}$$

Using the fact that the L^2 norm of an arbitrary matrix is the same as its largest singular value, we finally have the following; for the largest singular value ς_1 (assumed to be non-zero) of $\mathsf{F}\exp(\tau\mathsf{S})\mathsf{F}^{-1}$ and its associated right and left singular vectors $\boldsymbol{r}_1$ and $\boldsymbol{l}_1$, i.e.,

$$\mathsf{F}\exp(\tau\mathsf{S})\mathsf{F}^{-1}\boldsymbol{r}_1 = \varsigma_1\boldsymbol{l}_1, \tag{10.1.13}$$

which can result from the singular value decomposition (SVD), we get

$$G(\tau) = \varsigma_1^2, \tag{10.1.14}$$

and the optimal perturbation velocity input and output at time $t = \tau$ are

$$\tilde{\boldsymbol{v}}_{\text{opt}}(0) = \mathsf{PVF}^{-1}\boldsymbol{r}_1 \quad \text{and} \quad \tilde{\boldsymbol{v}}_{\text{opt}}(\tau) = \varsigma_1\mathsf{PVF}^{-1}\boldsymbol{l}_1. \tag{10.1.15}$$

10.2 Numerical parameters

Discretisation is necessary for the current problem formulation, and care should be taken to avoid non-physical errors arising from numerical parameters. In this research, we take advantage of the mapped Legendre spectral collocation method suitable for a rotating flow in an unbounded domain. The key numerical parameters in this scheme are the number of spectral basis elements M, the number of radial collocation points N, and the map parameter L. Detailed manipulation to well-resolve the eigenmodes is thoroughly explained in S. Lee and Marcus (2023). Here, we set $M + |m| = N$ to ensure $N \geq M$ and use various L to explore both potential and viscous critical-layer eigenmode families by adjusting the characteristic resolution of the scheme.

For comparison purposes, we secondarily consider the Chebyshev spectral collocation method with domain truncation at $r = R_\infty$. The domain of Chebyshev polynomials is linearly mapped from $[-1, 1]$ to $[0, R_\infty]$, as favoured in previous literature (e.g., Khorrami *et al.*, 1989; Mao & Sherwin, 2011), taking the primitive variables $\tilde{\boldsymbol{u}}$ and $\tilde{p}$ as state variables. The usage of this scheme in this research, however, is solely limited to investigating how sensitively the domain truncation affects the transient growth analysis outcome in comparison to the mapped Legendre spectral collocation method, serving as one significant drawback despite its constructional convenience for computation.

10.3 Physical parameters

There are five physical parameters affecting the nature of the problem: τ, q, Re, m and κ. We here clarify what range or value of each parameter shall be considered the target of analysis.

The maximum energy growth G is explicitly a function of the total time of growth τ, which indicates how much in time we permit linear transient dynamics of the wake vortex. In the context of aircraft trailing vortices, the upper limit may be clear due to the dominance of the Crow instability mechanism after several hundred time units ($= R_0/U_0$). For instance, Matsushima and Marcus (1997, pp. 341-343) reported the prevalence of the long wavelength instability at around $t = 200$ from the initial counter-rotating vortex pair configuration. Under proper rescaling of units, the trailing vortex simulation by Han *et al.* (2000, pp. 295-297, also see figure 10) exhibited the vortex linkage at $t = 229.12$ under a moderate level of ambient turbulence. Based on this reasoning, we concentrate on investigating the region where $\tau \lesssim O(10^2)$. We typically focus on the transient growth in the time range of $10 < \tau \leq 100$, in which relatively fast transient growth is expected (Mao & Sherwin, 2012). However, we note that a further range may be explored in case we need to confirm the asymptotic decay of this transient growth.

In addition, the outcomes of the analysis can be subject to the underlying physical parameters including the swirl parameter q, the Reynolds number Re and the azimuthal and axial wavenumbers m and κ. We fix the first two parameters in this research and, unless specified, we use $q = 4$ and $Re = 10^5$. We believe these values represent the cases where the swirling motion is strong enough to exclude the significant linear instabilities (e.g., $q \geq 2.31$, see Heaton, 2007a) and the viscous diffusion is small enough to assume the base vortex profile to be quasi-steady. It is remarked that, according to the experiment-based estimation by Fabre and Jacquin (2004, p. 259), this setup may reflect the condition of actual trailing vortices behind a large transport aircraft. As for the perturbation wavenumbers, we take attention to the axisymmetric or helical cases ($m = 0$ or 1) with small axial wavenumbers of order unity or less. This is not only because these cases have been the most prevalently examined in the vortex transient growth literature (e.g., Antkowiak & Brancher, 2004; Pradeep & Hussain, 2006; Mao & Sherwin, 2012; Navrose *et al.*, 2018), but also because these relatively low-frequency perturbations are more likely to account for the principal portion of perturbation structure we later desire to initiate via particles nearby the vortex.

Chapter 11

Optimal perturbations

11.1 Numerical sensitivity and proper discretisation

We construct optimal perturbations by combining the eigenmodes of the wake vortex. To obtain correct results, the computation scheme we choose should accurately represent every physical eigenmode family in a well-resolved manner, and the results should remain insensitive to changes in numerical parameters. We compare the numerical sensitivity of the mapped Legendre spectral collocation method and the Chebyshev spectral collocation method and determine which one is more suitable for the present analysis.

When considering the viscous eigenmodes that are regular throughout the entire radial domain, including their asymptotic behaviours near the origin and as r approaches infinity, there are three important eigenmode families: the discrete family, the potential family, and the viscous critical-layer family (S. Lee & Marcus, 2023). The first family, as the name suggests, is associated with discrete spectra (i.e., sets of eigenvalues), and each eigenmode's spatial structure is uniquely identified by the number of 'wiggles' clustered in or around the vortex core. The other two families consist of continuous eigenmodes with spatial structures that vary continuously, associated with continuous spectra.

Figure 11.1 shows numerically resolved spectra of the q-vortex with the following physical parameters: $(m,\, \kappa,\, q,\, Re) = (1,\, 1.0,\, 4.0,\, 10^5)$, envisioning the families of eigenmodes. We employed both the Chebyshev spectral collocation method, where $M = 800$, and the mapped Legendre spectral collocation method, where $M = 400$. To illustrate the continuous spectra, we have gathered all numerical eigenvalues obtained through varying the values of the domain truncation radius R_∞, which falls within the range of $[12,\, 13]$ for the Chebyshev spectral method, and the map parameter L, which spans $[3,\, 3.1]$ for the mapped Legendre spectral method. Given perfect resolution, the free-stream and potential spectra are expected to stretch out to $\mathrm{Re}(\sigma) \to -\infty$. We note that the spectra are presented in two panels with different aspect ratios. The left panel extends to large $|\mathrm{Re}(\sigma)|$ to showcase the free-stream and spurious spectra. The eigenmodes associated with the free-stream spectrum and the spurious spectrum exhibit non-regular characteristics. The former is singular as it does not

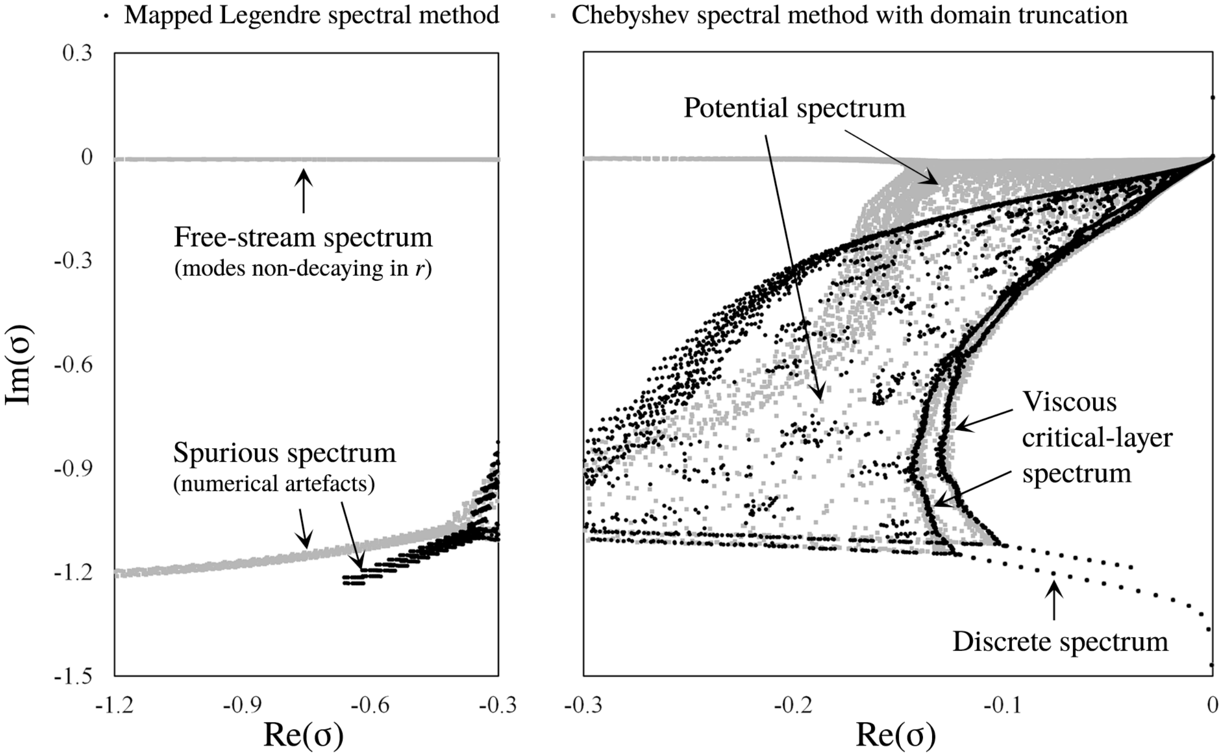

Figure 11.1: Numerical spectra of the q-vortex with $(m,\ \kappa,\ q,\ Re) = (1,\ 1.0,\ 4.0,\ 10^5)$ using the Chebyshev spectral collocation method (grey squares), and the mapped Legendre spectral collocation method (black dots). The consistency of the discrete spectrum attests the robustness of the two methods. The free-stream and spurious spectra (in the left panel) are associated with either singular or non-physical eigenmodes, thus superfluous for this study. Most of them are generated by the Chebyshev spectral method. The discrete, potential and viscous critical-layer spectra (in the right panel) are associated with regular eigenmodes. Two curves of the viscous critical-layer spectrum are more distinctive via the mapped Legendre spectral method.

decay to zero as $r \to \infty$ (Mao & Sherwin, 2011), and the latter is non-physical, characterised by irregular oscillations near the origin (S. Lee & Marcus, 2023). The right panel contains the discrete, potential, and viscous critical-layer spectra. These are associated with the respective regular eigenmode families mentioned above.

A couple of issues arise when we choose the Chebyshev spectral method over the mapped Legendre spectral method to resolve the eigenmodes. First of all, as depicted in the left panel of figure 11.1, a significant portion of the numerically resolved spectra account for the eigenmode families either singular or non-physical, which are solely redundant for the present problem. This issue is most likely to stem from approximating the asymptotic constraints to the subordinate boundary conditions at both ends of the computational domain. In the Chebyshev spectral method, as for $m = 1$, we have implemented the boundary conditions of

$$\frac{d\tilde{u}_r}{dr} = \frac{d\tilde{u}_\phi}{dr} = \tilde{u}_z = \tilde{p} = 0 \quad \text{at} \quad r = 0, \tag{11.1.1}$$

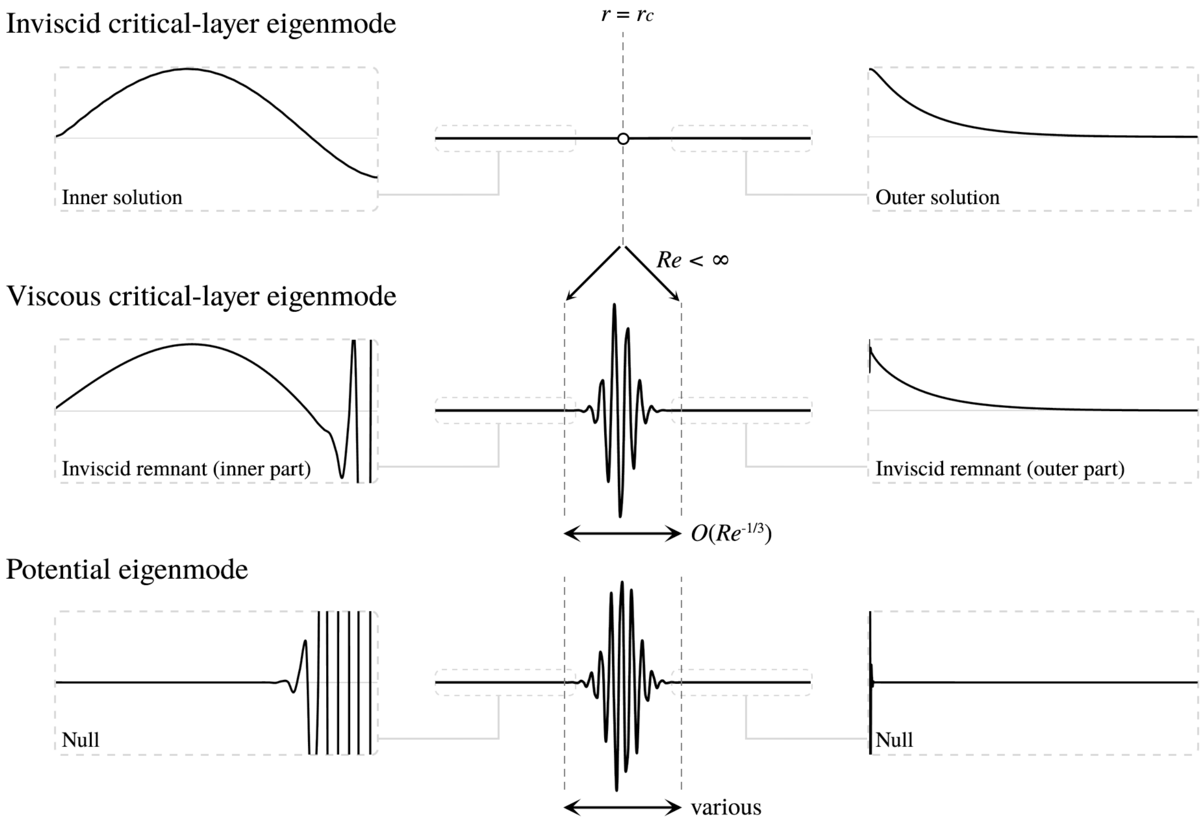

Figure 11.2: Schematic comparison between viscous critical-layer and potential eigenmodes. Both exhibit a similar large-scale structure in the region where the viscosity effect is locally dominant, which corresponds to a singularity at $r = r_c$ in the inviscid limit. The width of this large-scale structure scales as $O(Re^{-1/3})$ (see Lin, 1955) for the viscous critical-layer eigenmode. In contrast, for the potential eigenmode, the width can vary even at the same Re. The potential eigenmode forms a 'wave packet' in compliance with the pseudomode analysis (see Trefethen & Embree, 2005). Aside from the location $r = r_c$, the viscous critical-layer eigenmode inherits the structure of its inviscid counterpart, while the potential eigenmode just turns into null.

and

$$\tilde{u}_r = \tilde{u}_\phi = \tilde{u}_z = \tilde{p} = 0 \quad \text{at} \quad r = R_\infty, \tag{11.1.2}$$

which are proxies for the analyticity at the origin and the rapid decay condition as $r \to \infty$, respectively (see Ash & Khorrami, 1995). Even though (11.1.1) and (11.1.2) may serve as necessary conditions for what they are supposed to mimic, they can never be considered formally equivalent. For instance, (11.1.2) does not prohibit solutions from oscillating in the far field as long as the oscillation is momentarily zeroed out at $r = R_\infty$, which explains the emergence of the free-stream spectrum.

The second issue comes with the unclear distinction between the viscous critical-layer spectrum and the potential spectrum. As discussed in S. Lee and Marcus (2023, pp. 41-42),

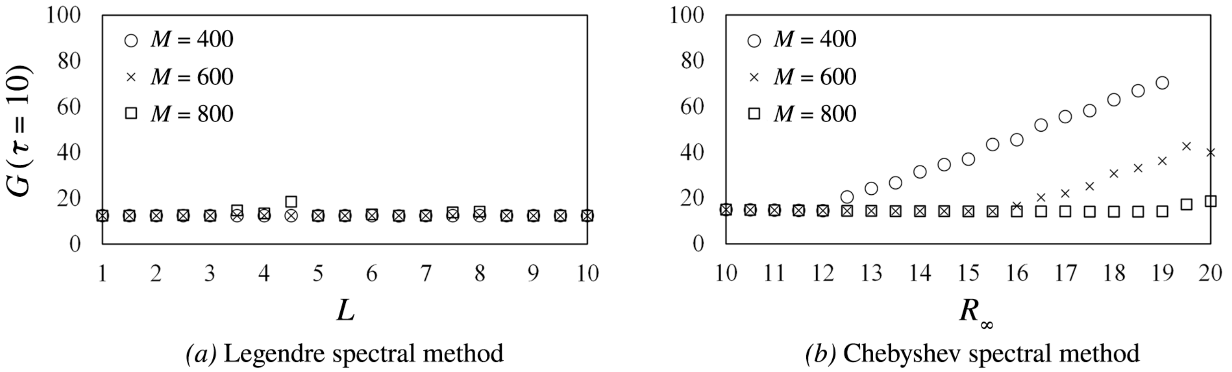

Figure 11.3: Numerical sensitivity test by evaluating $G(\tau = 10)$ from the entire eigenspace associated with $(m,\ \kappa,\ q,\ Re) = (1,\ 1.0,\ 4.0,\ 10^5)$ using (a) the mapped Legendre spectral collocation method with varying L, and (b) the Chebyshev spectral collocation method with varying R_∞, for $M = 400$, 600 and 800. The test ranges are based on typical usage for each parameter. Setting a finite R_∞ fundamentally damages the unbounded nature of the problem, and therefore, a large R_∞ should be preferred, while L can be arbitrarily chosen without impacting the unboundedness of the domain. However, as R_∞ increases, the evaluation is undesirably numerically sensitive.

the Chebyshev spectral method produces scattered traces of the two curves of the viscous critical-layer spectrum, making it less clear to distinguish the curves from the surrounding continuous region. This scattering can be attributed to the high sensitivity of the continuous spectra even to minor errors. In the Chebyshev spectral method, the domain truncation removes any spatial information apart from the origin, which, albeit diminutive, holds physical significance. Figure 11.2 illustrates the difference between the viscous critical-layer eigenmodes and the potential ones. Despite their structural resemblance on a large scale, the viscous critical-layer eigenmodes maintain the structure of their inviscid counterparts outside the region where viscosity effect dominates locally, scaled in the order of $Re^{-1/3}$ (Lin, 1955). In contrast, the potential eigenmodes just turns into null outside this region, epitomising their 'wave packet' form (Mao & Sherwin, 2011) which conforms to the twist condition presented by Trefethen and Embree (2005, pp. 98-114). More details of their comparison are omitted here; they have been elucidated in S. Lee and Marcus (2023).

A numerical sensitivity test involving the evaluation of the maximum energy growth G at $\tau = 10$ from the entire eigenspace using the two methods is presented in figure 11.3. The other physical parameters remain the same: $(m,\ \kappa,\ q,\ Re) = (1,\ 1.0,\ 4.0,\ 10^5)$. Unsurprisingly, increasing the number of spectral elements M enables both methods to be less sensitive to changes in numerical parameters. At a fixed M, the map parameter L serves as a resolution tuning parameter in the mapped Legendre spectral collocation method, and the domain truncation radius R_∞ in the Chebyshev spectral collocation method. Note that the test ranges shown in figure 11.3 are based on the typical usage for each parameter as found in S. Lee and Marcus (2023) and Mao and Sherwin (2011), respectively. Changes in L

by and large do not affect $G(\tau = 10)$ in the test range of the mapped Legendre spectral collocation method ($1 \leq L \leq 10$). Therefore, we may arbitrarily choose L within this range. On the contrary, $G(\tau = 10)$ is affected by changes in R_∞ in the test range of the Chebyshev spectral collocation method ($10 \leq R_\infty \leq 20$), particularly as R_∞ increases. This is problematic because using a large R_∞ should be preferred to minimise its detrimental influence on the unbounded nature of the radial domain. We observed that this problem is mitigated by manually excluding the sub-eigenspace spanned by the free-stream eigenmodes, which is, in fact, proactively removed in the mapped Legendre spectral collocation method. We believe that the exclusion is reasonable from a physical standpoint because the non-decaying behaviour of the free-stream eigenmodes implies that they analytically possess infinite energy. This, in turn, renders them formally inapplicable in the current transient growth context.

To recapitulate, when it comes to resolving the eigenmodes of the q-vortex in a radially unbounded domain, the Chebyshev spectral method has a couple of issues resulting from domain truncation, and they unfavourably affect the numerical sensitivity with respect to transient growth evaluation. Instead, the mapped Legendre spectral method can be an effective alternative to overcome these numerical limitations, making it more suitable for the current problem. Consequently, we choose the mapped Legendre spectral collocation method to analyse the transient growth of the wake vortex.

11.2 Maximum energy growth

Mao and Sherwin (2012) demonstrated that transient growth primarily results from the non-normality of the continuous eigenmodes, while the discrete eigenmodes play a less significant role. Here, they used the term ‘continuous eigenmodes’ as a compilation of the potential and free-stream families. However, as we pointed out earlier, the free-stream eigenmodes may not be appropriate for evaluating maximum energy growth because their energy reaches infinity. Therefore, in their argument, ‘continuous eigenmodes’ should be more specifically referred to as the potential ones. Not only that, but their argument also requires further refinement because they overlooked the viscous critical-layer eigenmodes. In their classification, this eigenmode family was not distinguished from the potential family, presumably due to the overlap in the spectra of these two families (see Mao & Sherwin, 2011, p. 8), as well as their structural similarity on a large scale (see figure 11.2).

Accordingly, the argument put forth by Mao and Sherwin (2012) still necessitates further clarification regarding which continuous eigenmode family primarily contributes to the optimal perturbation leading to maximum energy growth: the potential family or the viscous critical-layer family. To that end, we first evaluate the values of $G(\tau)$ from the entire eigenspace and then compare them with those from different sub-eigenspaces respectively spanned by a distinct eigenmode family.

Figure 11.4 shows the plots of numerically evaluated values of $G(\tau)$ from the entire eigenspace at various wavenumbers κ for the $m = 0$ and $m = 1$ cases, respectively. In the

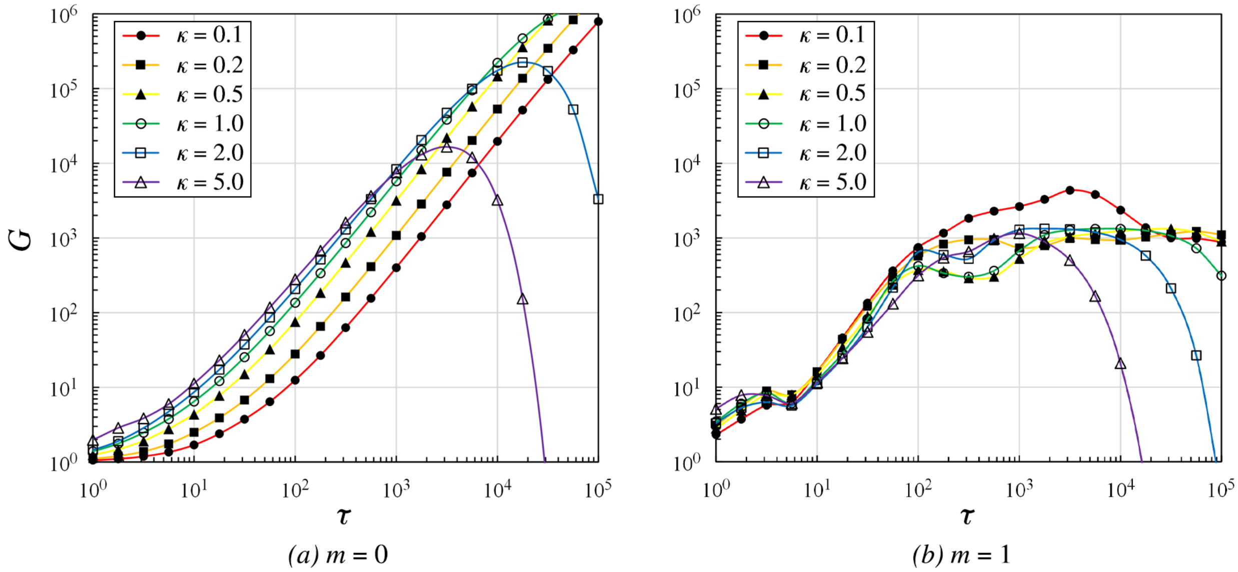

Figure 11.4: Maximum energy growth with respect to total growth time (a) at $m = 0$ (axisymmetric) and (b) at $m = 1$ (helical). The values of G are evaluated from the entire eigenspace, whose basis elements involve the whole discrete, potential and viscous critical-layer families. Here, $q = 4$ and $Re = 10^5$.

cases of $m = 0$, where the perturbations are essentially two-dimensional (i.e., subject only to r and z), the dependence of the G curves on κ is clear and monotonous. In the short run, the growth is strong with large κ, whereas in the long run, the largest G is obtained with smaller values of κ. One may check in figure 11.4(a) that the upper envelope of all curves sequentially corresponds to the curves with decreasing κ as τ increases. This trend at $m = 0$ aligns with previous observations in the literature (Pradeep & Hussain, 2006; Mao & Sherwin, 2012), supporting the validity of our evaluation. When it comes to $m = 1$, with three-dimensional perturbations, the κ-dependence of the G curves is no longer monotonous, as previously reported in Antkowiak and Brancher (2004). Focusing on a relatively short-term growth, we can see that the largest G at $m = 1$ is generally greater than that at $m = 0$. For example, at $\tau = 10^2$, the largest G among the evaluated values is 7.5×10^2 for $\kappa = 0.1$ at $m = 1$, while it is 2.8×10^2 for $\kappa = 5.0$ at $m = 0$.

The maximum energy growth curves evaluated from the entire eigenspace and the sub-eigenspaces, each respectively spanned by the discrete family, the viscous critical-layer family and the potential family, are compared in figure 11.5. It is clear that the curves from the entire eigenspace are mainly reproduced by those evaluated from the sub-eigenspace spanned by the viscous critical-layer family, indicating its dominant contribution. On the other hand, the values of $G(\tau)$ from the rest of the continuous sub-eigenspace, for which the potential eigenmodes account, exhibit a similar order of magnitude to those from the discrete sub-eigenspace. The contribution of the potential family is, therefore, as minor as that of the

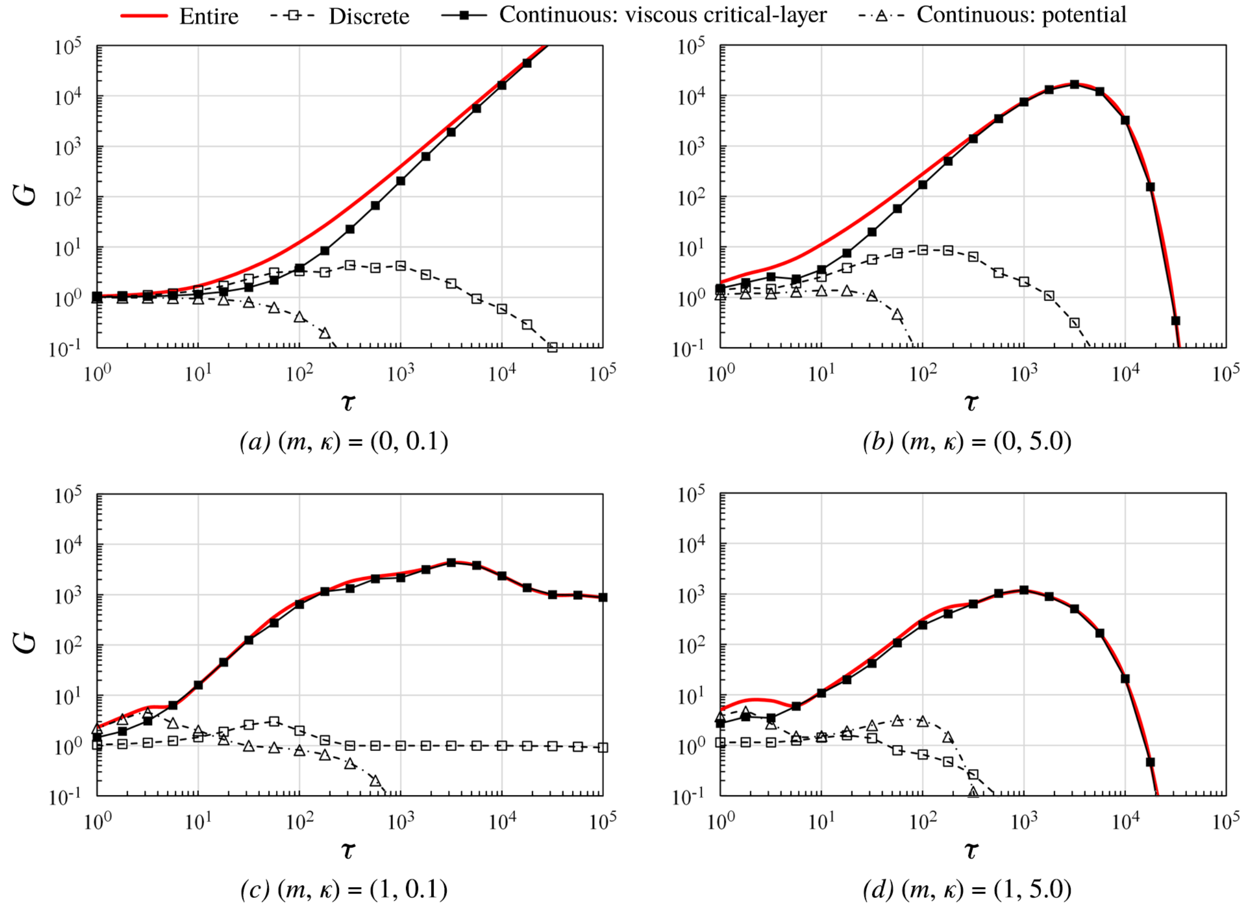

(a) (m, κ) = (0, 0.1)

(b) (m, κ) = (0, 5.0)

(c) (m, κ) = (1, 0.1)

(d) (m, κ) = (1, 5.0)

Figure 11.5: Comparison of the curves of $G(\tau)$ evaluated from different sub-eigenspaces, each respectively spanned by a distinct eigenmode family: (*a*) $(m,\ \kappa) = (0,\ 0.1)$, (*b*) $(m,\ \kappa) = (0,\ 5.0)$, (*c*) $(m,\ \kappa) = (1,\ 0.1)$, and (*d*) $(m,\ \kappa) = (1,\ 5.0)$. Here, $q = 4$ and $Re = 10^5$. The maximum energy growth curves from the entire eigenspace are the same as those plotted in figure 11.4, which are mainly reproduced by those evaluated from the sub-eigenspace spanned by the viscous critical-layer family.

discrete family in transient growth.

There are two minor exceptions worth noting. At $m = 0$, the discrete family accounts for short-term optimal growth as significantly as the viscous critical-layer family, especially when κ is small. We believe that this is relevant to the fact that when $m = 0$, critical layers vanish in the limit of $\kappa \to 0$, and so do the derived continuous eigenmodes, while the discrete ones remain. Next, at $m = 1$, the contribution of the potential family to optimal growth slightly supersedes that of the viscous critical-layer family for a brief period ($\tau < 10$), explaining the presence of a quirk in the G curves around $\tau = 5.6$. However, the exception clears quickly after this period, and the largest G attainable in this period never exceeds 10, thus not overturning the general dominance of the viscous critical-layer family in terms of transient growth.

Based on these observations, we revisit the demonstration provided by Mao and Sherwin (2012) with the following clarification; the non-normality of the continuous eigenmodes induces significant transient growth, and more precisely, it is the viscous critical-layer family that predominantly contributes to this growth, instead of the potential family. The distinction is important as it addresses the 'true' origin of transient growth of the wake vortex as critical layers. The potential eigenmodes have their theoretical foundation in the wave packet pseudomode analysis (Trefethen & Embree, 2005). As showcased in figure 11.2, they omit the asymptotic information of critical layers, making their birth irrelevant to those requiring asymptotic matching or equivalently, the critical layer analysis (Lin, 1955; Le Dizès, 2004). Although the wave packet pseudomode analysis is deemed to be a powerful tool to explore all possible forms of continually varying eigensolutions, it may divert our attention too much from the genuine gems more worthy of our focus. Furthermore, our clarification provides a better alignment with the previous argument made by Heaton (2007b) that inviscid continuous spectrum (CS) transients dominate the growth over short time intervals. The viscous critical-layer family in our classfication corresponds to the viscous regularisation of the inviscid CS, which we have denoted the inviscid critical-layer spectrum (S. Lee & Marcus, 2023), when $Re < \infty$.

11.3 Perturbation structures

The impact of changes in m and κ on perturbation structures leading to optimal transient growth has been widely investigated and is well-known in the context of linear vortex dynamics (Antkowiak & Brancher, 2004; Pradeep & Hussain, 2006; Mao & Sherwin, 2012). In this chapter, we examine whether our transient growth calculation complies with the established findings and then compare and analyse the perturbation structures with respect to different values of m and κ for further consideration.

Pradeep and Hussain (2006) reported that axisymmetric perturbation cases ($m = 0$) generally exhibit the largest energy growth, as we showed in figure 11.4. However, as the largest G increases, the total growth period of the perturbation is monotonously extended (i.e., τ required to achieve G increases), as its spatial structure becomes increasingly distant from the vortex core, resulting in slower interactions. For helical perturbation cases ($m = 1$), a common spatial structure emerges, with the primary motion localised around a certain radius near the vortex core. In the case of $m = 1$ perturbations, it is noteworthy that their growth may lead to the initiation of vortex core fluctuations, even though they initially originate outside the core. This mechanism has occasionally been considered a trigger of erratic long-wavelength displacements in experimental vortices (e.g., Edstrand *et al.*, 2016; Bölle *et al.*, 2023), referred to as 'vortex meandering' (see Antkowiak & Brancher, 2004, p. L4). Mao and Sherwin (2012) found that the vortex meandering phenomenon can be driven by the transient response of the vortex to an out-of-core perturbation.

As mentioned in §10.3, our focus is on the relatively short time period of $10 < \tau \leq 100$ to study the transient growth process. In longer periods, classical linear instability mechanisms like the Crow instability may predominate in real conditions. Within this time range, the largest values of G attained from our considerations (see figure 11.4) occur at $\kappa = 5.0$ for the $m = 0$ cases and at $\kappa = 0.1$ for the $m = 1$ cases. We consider these cases as representative. In figure 11.6, we illustrate the optimal perturbation velocity inputs and outputs for $\tau = 31.6$ and $\tau = 100$, all of which are depicted by the absolute velocity components. For more intuitive visualisation, we portray their corresponding three-dimensional structures alongside, each of which is represented by the iso-surface of 50% of the maximum specific energy in physical space, i.e., $|(\tilde{\boldsymbol{u}}(r)e^{\mathrm{i}(m\phi+\kappa z)} + \text{c.c.})/2|^2$, where c.c. stands for the complex conjugate of the antecedent term. The dark and light surface colours respectively express counterclockwise and clockwise swirling directions.

In all cases, the following characteristics are commonly observed. First, azimuthal velocity components are initially dominant for all optimal perturbations, while the other velocity components evolve significantly towards the end of the growth period. This clearly indicates that the azimuthal velocity component should be the primary focus if one intends to induce these optimal perturbations from the unperturbed state. Second, the most energetic part of the optimal perturbation inputs, coinciding with the peak of the absolute azimuthal velocity component, tends to be distant from the vortex core as τ increases. One may see a considerable difference particularly for cases (c) and (d), as the major perturbation structure overlaps the core region when $\tau = 31.6$ whereas it moves out of the core when $\tau = 100$.

For cases (a) and (b), where $(m, \kappa) = (0, 5.0)$, the input perturbations generally form a ring structure owing to its azimuthal independence. As the perturbation develops, it is evident that the radius of the ring does not change significantly. Taking into account other cases with different wavenumbers (even besides the illustrated ones), we found this tendency toward local confinement of optimal perturbation structures to take place in general with increasing κ. This indicates that a perturbation with a shorter axial wavelength has a more localised influence around the initially perturbed region.

For cases (c) and (d), where $(m, \kappa) = (1, 0.1)$, a spiral structure emerges in the most energetic region of the input perturbation due to the alternating layering of two oppositely swirling fluid motions at the periphery of the vortex core. Unlike the axisymmetric cases, the perturbation structure undergoes a drastic change when comparing its input and output states. Specifically, the most energetic region of the perturbation, even if it was originally

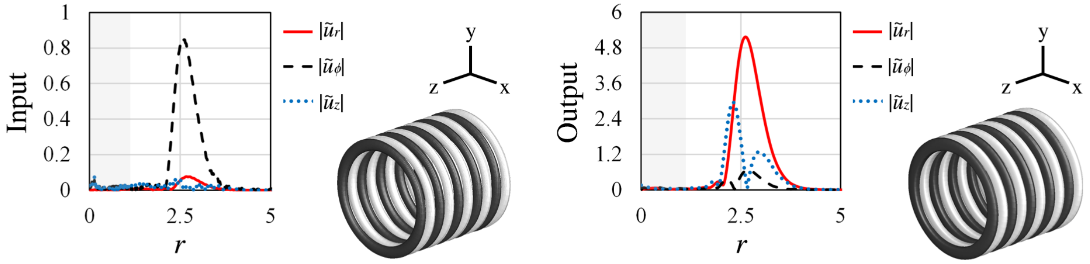

(a) $(m, \kappa) = (0, 5.0)$, $\tau = 31.6$, $G = 5.0 \times 10^1$

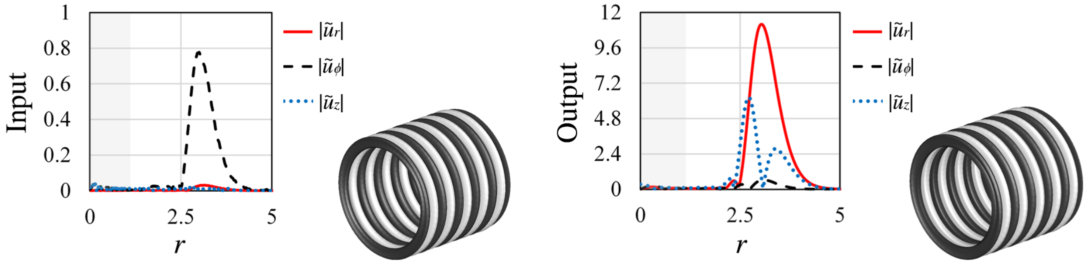

(b) $(m, \kappa) = (0, 5.0)$, $\tau = 100$, $G = 2.8 \times 10^2$

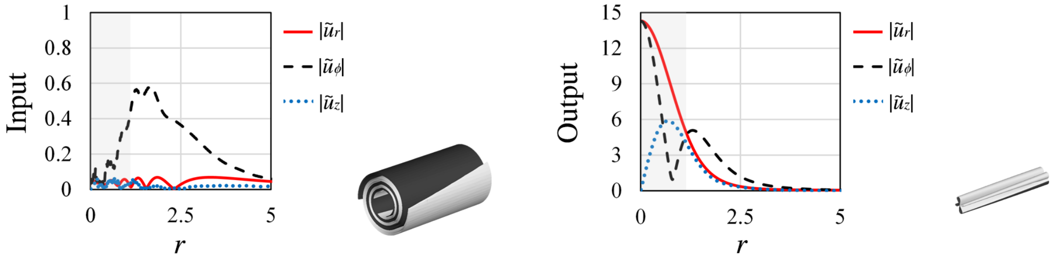

(c) $(m, \kappa) = (1, 0.1)$, $\tau = 31.6$, $G = 1.3 \times 10^2$

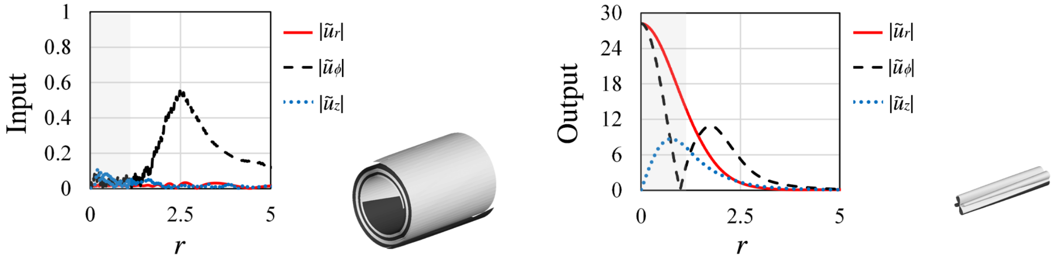

(d) $(m, \kappa) = (1, 0.1)$, $\tau = 100$, $G = 7.5 \times 10^2$

Figure 11.6: Optimal perturbation inputs of unit energy E defined in (10.1.7) and amplified outputs at $t = \tau$, depicted by the absolute velocity components alongside their corresponding three-dimensional structures, each represented by the isosurface of 50% of the maximum specific energy in space. The dark and light colours respectively indicate counterclockwise and clockwise swirling of the flow at each position. Here, four representative cases with the largest value of G in figure 11.4 are displayed: (a, b) the axisymmetric cases of $(m, \kappa) = (0, 5.0)$ for $\tau = 31.6$ and $\tau = 100$, respectively, and (c, d) the helical cases of $(m, \kappa) = (1, 1.0)$ for $\tau = 31.6$ and $\tau = 100$, respectively. The initial dominance of azimuthal velocity components is common to all cases, and that for $m = 1$, energy is transferred into the core region $r \leq 1.12$ (shaded in each plot).

located outside the vortex core, ultimately penetrates into the vortex core. As a consequence, the transverse velocity ($\tilde{u}_r$ and $\tilde{u}_\phi$) at the vortex centre becomes the greatest. In other words, the principal response of the vortex to optimal perturbations with $m = 1$ is transverse motion of the vortex core, which is likely to be connected with the vortex meandering phenomenon (Edstrand *et al.*, 2016; Bölle, 2021).

We want to clarify that the finding regarding the induction of vortex meandering by optimal helical perturbations with an axially long wavelength was formerly given by Mao and Sherwin (2012). They employed mesh-based direct numerical simulations instead of the matrix-based analysis (corresponding to (10.1.6) - (10.1.15) in our formulation), even though they used the matrix-based approach when $m = 0$. In a way, this choice seems to have been made to overcome difficulties in dealing with analyticity at the origin, which depends on the value of m (see S. Lee & Marcus, 2023, pp. 51-52). On the other hand, our approach, based on the mapped Legendre spectral collocation method, is fundamentally designed to remain robust for any value of m. Therefore, our contribution here lies in recognising the same phenomenon linked with $m = 1$ perturbations based on the computationally fast and formally consistent matrix-based transient growth analysis.

11.4 Non-linear impacts on an optimally perturbed vortex

Given an optimally perturbed vortex, the linearised theory (see §10.1) predicts that the perturbation is gradually amplified as time approaches $t = \tau$ and then decays as far as there are no extrinsic factors to give rise to secondary instabilities starting from the most perturbed state. We spare this chapter for verifying that such transient behaviour still takes importance in the original non-linear system, complying with (10.1.2), in spite of energy transfer across different wavenumbers or relevant non-linear effects.

Although the optimal perturbation structures vary with the selection of m, κ and τ, what we aim to investigate here is their comprehensive and common trend of evolution in time anticipated in the linearised theory. We pay attention to one specific optimal perturbation case where $(m, \kappa) = (1, 0.1)$ with the optimal growth time $\tau = 50$, where the z-component of the perturbation vorticity input $\omega'_z(t = 0)$ on the $z = 0$ plane is illustrated in figure 11.7. This perturbation is chosen because the drastic transition of the most energetic portion of the perturbation from the periphery to the vortex core, as shown in figure 11.6(c, d), may be a good means to a plain illustration of the vortex growth. We emphasise that, however, this specific behaviour at $m = 1$ (presumably related to vortex meandering) itself is not the target of interest at this point. To those who are interested in the meandering of vortices, we suggest referring to Edstrand *et al.* (2016) and Bölle (2021).

According to the linearised theory, the optimal perturbation velocity input, which can be expressed as $\tilde{\boldsymbol{v}}_{\mathrm{opt}}(0) = \mathbf{P}\mathbf{V}\mathbf{F}^{-1}\boldsymbol{r}_1$ as in (10.1.15), evolves at $t = \eta$ as

$$\tilde{\boldsymbol{v}}_{\mathrm{opt}}(\eta) = \mathbf{P}\mathbf{V}\exp(\eta\mathbf{S})\mathbf{F}^{-1}\boldsymbol{r}_1. \tag{11.4.1}$$

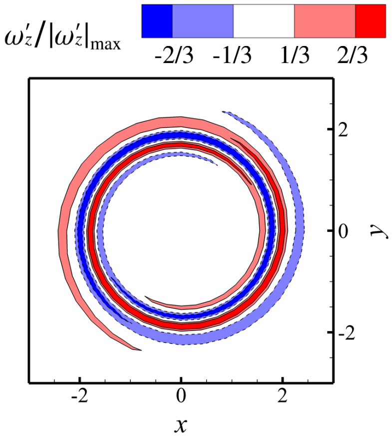

Figure 11.7: Axial perturbation vorticity contour on the $z = 0$ plane of the optimal input where $(m,\ \kappa) = (1,\ 0.1)$ with the optimal growth time $\tau = 50$. The contour lines are solid for the positive levels (-67 % and -33 % of the absolute maximum) and dashed for the negative levels (33 % and 67 % of the absolute maximum).

One may check the consistency of the above equation when $\eta = \tau$ with $\tilde{\boldsymbol{v}}_{\mathrm{opt}}(\tau)$ given in (10.1.15). We label this prediction from the linearised theory as 'linear.' The 'linear' prediction, however, may be ideal as it strips off all higher-order interactions coming from the non-linear convection term, i.e., $\boldsymbol{u} \times \boldsymbol{\omega}$ in (10.1.2), which transfers energy from the perturbation wavenumbers of $(m,\ \kappa)$ to the multiples (e.g., $(2m,\ 2\kappa)$, $(3m,\ 3\kappa)$, $\cdots$) or vice versa. We refer to the growth of the optimal perturbation in consideration of the influence of higher-order interactions as 'non-linear.' The significance of this non-linearity substantially depends on the initial perturbation's energy level. If the perturbation energy approaches zero (or the perturbation is infinitesimal), the 'non-linear' evolution should follow the 'linear' prediction. We set aside the numerical details regarding our non-linear simulations in Appendix D.

In the non-linear simulations, the initial velocity field $\boldsymbol{u}(t = 0)$ is defined as follows:

$$\boldsymbol{u}(r, \phi, z, t = 0\,;\, \varepsilon) \equiv \overline{\boldsymbol{U}}(r) + \varepsilon \tilde{\boldsymbol{u}}_{\mathrm{opt}}(r) e^{i(m\phi + \kappa z)} + \text{c.c.}, \tag{11.4.2}$$

where ε determines how intense the initial perturbation is, adjusting the perturbation energy input. The base term representing the unperturbed q-vortex, $\overline{U}(r)$, has been assumed to be unchanging in time in the linear analysis, as its radial diffusion due to viscosity is negligible due to the high Re number in our problem setup. In contrast, the non-linear simulations take this small viscous diffusion effect of the base q-vortex into account for accuracy purposes. That is to say, even the unperturbed flow changes slowly with respect to time. This can be calculated as the non-linear simulation with $\varepsilon = 0$. As a result, the perturbation velocity field at $t = \eta$ is assessed as the difference between two time-varying fields, i.e.,

$$\boldsymbol{u}'(r, \phi, z, \eta\,;\, \varepsilon) \equiv \boldsymbol{u}(r, \phi, z, \eta\,;\, \varepsilon) - \boldsymbol{u}(r, \eta\,;\, 0). \tag{11.4.3}$$

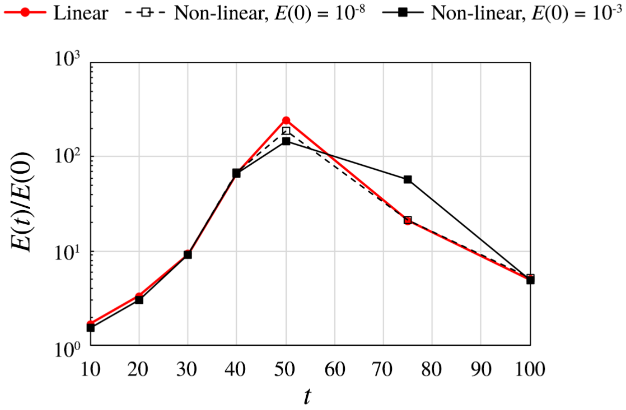

Figure 11.8: Comparison of the transient energy growth curves in the 'linear' evolution case, calculated via (11.4.1), and in the 'non-linear' evolution cases with the initial perturbation energy of 10^{-8} and of 10^{-3}, calculated via three-dimensional non-linear simulations. The initial perturbation is illustrated in figure 11.7.

The perturbation energy at $t = \eta$, denoted $E(\eta)$, is evaluated as the volume integration of $\boldsymbol{u}' \cdot \boldsymbol{u}'$ divided by 2π times the axial wavelength ($= 2\pi/\kappa$), for the consistency with our energy definition in (10.1.7).

In figure 11.8, three energy growth curves are plotted together for comparison. First, the energy growth curve in the linear evolution case peaks at $t = \tau = 50$. In this case, the maximum energy growth G is 2.5×10^2. This curve serves as an index of the prevalence of the linear process during early transient growth of vortices. Second, the energy growth curve in the non-linear evolution case with $E(0) = 10^{-8}$ is almost identical to the 'linear' index curve. In this case, the non-linearity should be considered but only in an infinitesimal manner and its influence appears to be marginal. The only notable exception is a debilitation of the maximum energy growth at $t = \tau = 50$. However, it is unlikely that this debilitation is entirely due to the introduction of non-linearity because, according to Mao and Sherwin (2012, p. 55), such a drop in energy growth at the peak appears to stem from the consideration of viscous diffusion of the base flow in time. Lastly, the energy growth curve in the non-linear evolution case with $E(0) = 10^{-3}$ exhibits more debilitation at the peak even than the prior non-linear case. Unlike the previous case, this demonstrates the clear intensification of the non-linearity. Nevertheless, the overall trend of the curve does not drift away from that of the 'linear' index curve. The coherence in trend holds particularly well until the maximum vortex growth ($t < \tau = 50$), which means that the linearised theory on transient growth is still effective in the original non-linear system.

The prevalence of the linear process in the early-stage vortex growth is much clear when we take a look at the evolution of the perturbation structure, which is shown in figure 11.9. Using the same contour style across the three different cases presented above, we illustrate three snapshots of the axial vorticity perturbation contours on the $z = 0$ plane at $t = 25$, $t = 50$ and $t = 100$ for each case. The structural coherence in vorticity perturbation between the linear and non-linear cases is evident at $t = 25$, representing the stage of rapid perturbation growth. At $t = 50$, or the optimal growth time, the perturbation structures are still comprehensively coherent. However, in the non-linear evolution case with $E(0) = 10^{-3}$, it can be found that the $m = 1$ symmetry weakly breaks up, which means that the other azimuthal wavenumbers rather than $m = 1$ begin to possess non-negligible energy via the higher-order energy transfer across different wavenumbers. At $t = 100$, representing the stage of asymptotic stabilisation, the perturbation structures no longer show strong resemblance. This is another evidence of the non-linearity intensification particularly as a result of prolonged vortex growth in time.

Last but not least, we note that the simulation with the initial perturbation energy of 10^{-3} results in the substantial displacement of the vortex core, as shown in figure 11.10, notwithstanding the seemingly small level of energy. The λ_2-isosurface where $\lambda_2 = -0.05$ is used to detect the vortex core (see Jeong & Hussain, 1995). The largest displacement of the vortex centre in the simulation is nearly equal to the core radius, coinciding with the experimentally observed meandering amplitude in the order of the core radius (see Devenport *et al.*, 1997; Bölle, 2021). Based on the rough figures of a large transport aircraft given in Fabre and Jacquin (2004, p. 259), the characteristic scales in our formulation become $U_0 \approx 27$ m/s and $R_0 \approx 0.5$ m and using the density of air $\rho \approx 1$ kg/m^3, the 'dimensionless' energy of 10^{-3} corresponds to the 'actual' kinetic energy of $(10^{-3}) \times 2\pi\rho(U_0^2/2)R_0^2 \approx 0.6$ J/m ('per metre' stands for the axial unit length), which appears to be not exorbitant in practice. We believe this strengthens the practicability of the optimal transient growth process under consideration, arguably owing to the radially concentrated nature of the optimal perturbation structures (see figure 11.7).

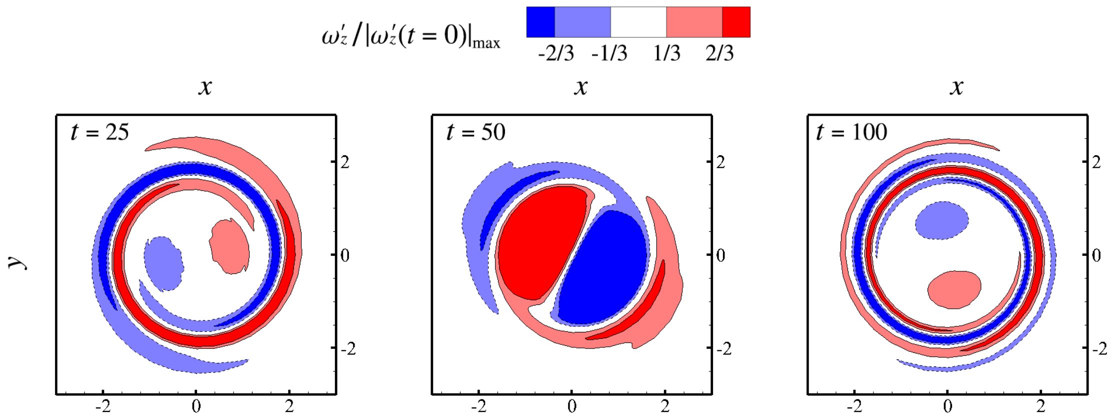

(a) Linear evolution

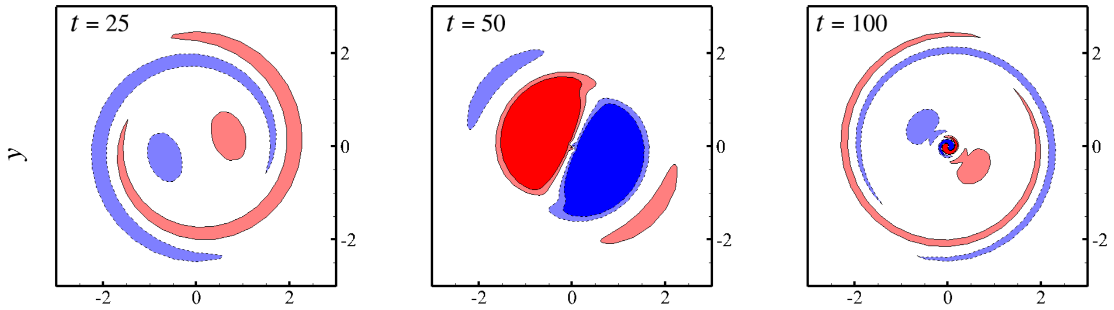

(b) Non-linear evolution, initial perturbation energy = 10^{-8}

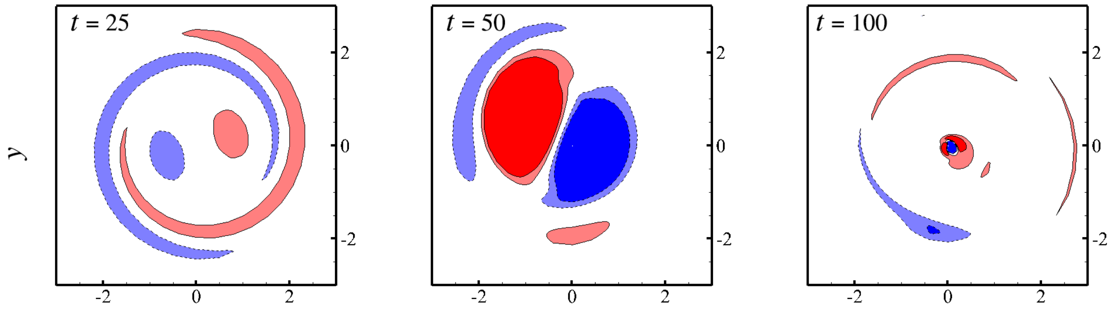

(c) Non-linear evolution, initial perturbation energy = 10^{-3}

Figure 11.9: Axial vorticity perturbation contours of the optimally perturbed vortex (refer to figure 11.7 for the illustration of the initial perturbation) on the $z = 0$ plane at $t = 25$, $t = 50$ and $t = 100$: (a) the 'linear' evolution case where the maximum energy growth is known to occur at $t = \tau = 50$, (b) the 'non-linear' evolution case with the initial perturbation energy of 10^{-8}, (c) the 'non-linear' evolution case with the initial perturbation energy of 10^{-3}. The same contour style as figure 11.7 is applied to all plots. Despite the non-linearity and its intensification with an increase in perturbation energy or in time, the 'linear' process still prevails the overall dynamics with respect to early vortex growth in the original non-linear system.

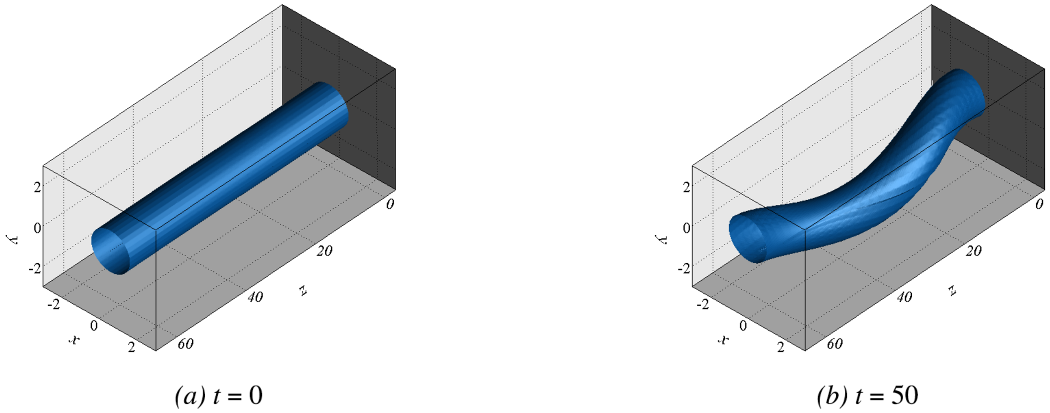

(a) $t = 0$ (b) $t = 50$

Figure 11.10: Three-dimensional illustration of the q-vortex with the helical perturbation (see figure 11.7) of the initial energy of 10^{-3}: (a) the initial core ($t = 0$), and (b) the most excited core ($t = \tau = 50$). To detect the vortex core, the λ_2-isosurface where $\lambda_2 = -0.05$ is depicted (see Jeong & Hussain, 1995). The maximum displacement of the vortex centre comes up to the order of the core radius, which is as substantial as the experimental meandering amplitude (see Devenport *et al.*, 1997; Bölle, 2021).

Chapter 12

Initiation of optimal transient growth

12.1 On a means of initiating optimal transient growth

The transient evolution of the optimally perturbed q-vortex that we have analysed in the previous chapter unveils a promising way to significantly disturb the vortex even if the base vortex is known to be linearly stable. For this growth process to be practically meaningful, an important question remains: By what means is the perturbation initiated? In our analyses and simulations thus far, perturbations have been presumed to be initially present along with the vortex, which is supposed to be initially in an undisturbed state. However, from a practical standpoint, there should be a means of causing such perturbations because they cannot originate from the undisturbed flow — the q-vortex, which by itself is quasi-steady. Without a plausible initiation process, the optimal transient vortex growth process may be no more than hypothetical.

One may consider ambient turbulence as a compelling explanation for initiation, as often addressed in the linear instability context (e.g., Crow & Bate, 1976; Han *et al.*, 2000). However, in contrast to linear instability mechanisms, where we anticipate that perturbations are destined to be explosive in the limit of $t \to \infty$ due to the most unstable eigenmode growing in an exponential manner, a transient growth process typically necessitates a specific (optimal) form of perturbation as input. The issue of whether such a specific perturbation can spontaneously originate from ambient turbulence, which is fundamentally stochastic and uncontrolled, has led to recurrent criticisms of optimal transient growth (see Fontane *et al.*, 2008, p. 235). In the work by Fontane *et al.* (2008), where the transient dynamics of vortices with stochastic forcing was analysed, they confirmed the activation of optimal perturbations by noise-like forcing that is random in both space and time. This mitigates the aforementioned criticisms of optimal transient growth. Nonetheless, as the authors stated, it remains questionable whether such random isotropic forcing effectively represents turbulence in real conditions. The lack of clear universality in modeling turbulence is believed to be an intractable challenge when incorporating ambient turbulence in the current problem.

Instead, we take the initiative in considering a different means of initiating optimal transient growth: ice crystals (or particles). Their presence in real life is ascertained through the observation of contrails. The formation of contrails primarily begins with jet exhaust plumes produced by aircraft engines, which contain particulate matter that sooner or later serves as condensation nuclei (Kärcher, 2018). We clarify that our focus does not lie in this very initial stage of contrails in the form of jet plumes. During this stage, the vortex roll-up process is underway, and, according to the early experimental study by El-Ramly and Rainbird (1977), there is no appreciable influence of the engine exhaust on the alteration of the rolled-up structure. As a matter of course, our attention is directed towards the later stage associated with a formed wake vortex, where the interaction between a vortex and ice crystals is manifest.

During the stage of ice crystals interacting with a wake vortex, the size of an individual particle reportedly comes up to a few microns (Kärcher *et al.*, 1996; Paoli & Garnier, 2005; Naiman *et al.*, 2011; Voigt *et al.*, 2011; Kärcher, 2018). Due to its relatively small length scale compared to the vortex scale (in metres), the entire ice crystals are often treated as flow tracers, i.e., particles with no backward influence on the carrier fluid (Paoli & Garnier, 2005; Naiman *et al.*, 2011). The assumption appears to be acceptable and efficiently simplifies the dynamics of the flow with particles. However, when considering the large particle number density, reportedly between 10^9 per cubic metre to 10^{11} per cubic metre (Paoli *et al.*, 2004; Paoli & Garnier, 2005), and the density ratio of ice to air (approximately 10^3), the bulk effect of the ice crystals cannot be simply negligible. Under optimistic estimation based on the given figures, the upper limit of the particle mass fraction may fall in the range between 10^{-2} and 10^{-1}. This amount is appreciable enough to initiate a perturbation that ultimately evolves into a substantial vortex disturbance via the transient growth process (recall §11.4).

When considering ice crystals in the development of contrails, the primary emphasis has typically centred on their microphysical growth. Consequently, the analysis often takes account of an ice microphysics model alongside a flow solver (e.g., Lewellen & Lewellen, 2001; Paoli *et al.*, 2004; Paoli & Garnier, 2005; Naiman *et al.*, 2011). However, this aspect is excluded from our consideration. Instead, we direct our attention to two-way coupling, specifically through drag momentum exchange. This approach aligns with our essential focus on examining the significance of the particles' backward disturbance to the wake vortex. Recalling that azimuthal perturbations commonly dominate during initial optimal transient growth (see the left panels in figure 11.6), we speculate that momentum exchange via drag provides an effective means of initiating optimal perturbations, complementing ambient turbulence whose action is stochastic and, in an ideal sense, non-directional.

We note that, according to recent studies by Shuai and Kasbaoui (2022) and Shuai *et al.* (2022), weakly inertial particles within a vortex under two-way coupled conditions are found to be influential enough to trigger instabilities and expedite the vortex decay process. Although the initial particle distributions considered in these studies, where particles are loaded either over the entire domain or inside the vortex core region, are not directly applicable to our case, where particles interact with the vortex along the periphery of the vortex core, the studies support the underlying idea that even a dilute amount of particles meaningfully affects the surrounding vortex.

12.2 Two-way coupled equations for a vortex interacting with particles

To simulate the initiation process leading to the transient growth of a vortex via particle drag, we need to consider additional parameters and variables in order to establish an equation for the motion of particles. Also, we should add a coupling term to the momentum equation of fluid motion in (10.1.2) to complete a two-way coupled formulation. In our discussion, the particles under consideration are dispersed ice crystals, with a density roughly 10^3 times greater than that of the surrounding fluid (air). We define the ratio of particle density ρ_p to fluid density ρ as a new dimensionless parameter, denoted by ϑ ($\equiv \rho_p/\rho$). We typically set ϑ to the constant value of 10^3 in later calculations.

In this study, we employ the Eulerian approach adopting the fast equilibrium approximation, proposed by Ferry and Balachandar (2001). In this method, the set of particles is treated as continuum, allowing the flow-particle system to behave like a two-phase flow. Due to the high particle number density, we refrain from the use of Lagrangian approaches tracking particles individually (e.g., Paoli *et al.*, 2004; Naiman *et al.*, 2011; Shuai *et al.*, 2022). Thanks to the relatively moderate computational cost, we believe the Eulerian approach is favourable for scale-up simulations, such as two or more vortices, to account for secondary vortex evolution in future studies. Also, our focus on the ‘bulk’ influence of particles on the surrounding vortex, rather than individual particle statistics, fairly justifies the treatment of particles as continuum.

The following two variables now represent the particles in the form of dispersed phase: particle velocity field $\boldsymbol{u}_p(r, \phi, z, t)$ and particle volume fraction $c(r, \phi, z, t)$. The fast equilibrium approximation allows $\boldsymbol{u}_p$ to be explicitly evaluated in terms of the fluid velocity field $\boldsymbol{u}$. Based on the Maxey-Riley equation with the added mass effect (Maxey & Riley, 1983; Auton *et al.*, 1988), $\boldsymbol{u}_p$ can be reduced in the resulting two-way coupled equations (see Ferry & Balachandar, 2001, p. 1221). They are

$$\frac{\partial \boldsymbol{u}}{\partial t} = -\boldsymbol{\nabla}\varphi + \boldsymbol{u} \times \boldsymbol{\omega} + \frac{1}{Re}\nabla^2 \boldsymbol{u} - (\vartheta - 1)c\frac{D\boldsymbol{u}}{Dt} \quad \text{with } \boldsymbol{\nabla} \cdot \boldsymbol{u} = 0, \tag{12.2.1}$$

and

$$\frac{\partial c}{\partial t} = -\boldsymbol{u} \cdot \nabla c + \frac{2Stk(\vartheta - 1)}{2\vartheta + 1}\nabla \cdot \left(c\frac{D\boldsymbol{u}}{Dt} \right), \tag{12.2.2}$$

where D/Dt is the material derivative with respect to the fluid phase and Stk is the Stokes number, i.e., the dimensionless particle relaxation time normalised by R_0/U_0. In calculations, we set $Stk = 10^{-5}$ to comply with the fast equilibrium approximation as well as practical conditions (Kärcher *et al.*, 1996). The discretisation and time-integration procedures for (12.2.1) and (12.2.2) are not different from the previous pure vortex cases, as detailed in

Appendix D. Compared to (10.1.2), it can be seen that the last term in (12.2.1) represents the particle drag, whose magnitude depends upon the order of c.

12.3 Initial particle distribution

As briefly discussed above with the recent studies on vortex-particle interactions (Shuai & Kasbaoui, 2022; Shuai *et al.*, 2022), the observable scope of vortex-particle interactions varies based on the initial distribution of particles. Accordingly, in order to substantiate that particle drag initiates optimal transient growth in the vortex, it is necessary to set up an effective initial distribution of the particles. We first remark that the role of particles here should be limited to small disturbance to the vortex system, which implies $(\vartheta-1)c$ significantly less than order unity in the following discussions.

To begin with, let's comprehend how the particles induce perturbations in the carrier fluid. Reorganising the coupled momentum equation in (12.2.1), we obtain

$$(1+(\vartheta-1)c)\,\frac{D\boldsymbol{u}}{Dt}=-\boldsymbol{\nabla}p+\frac{1}{Re}\nabla^2\boldsymbol{u}, \tag{12.3.1}$$

which is in fact the original form Ferry and Balachandar (2001) provided. In this form, it is clearly demonstrated that the combined motion of the two phases behaves like a single-phase flow with a slight density variation with a multiplication factor of $(1+(\vartheta-1)c)$. This effect is understood as a consequence of the dispersed phase absorbing momentum from the fluid phase. Loosely speaking, if the fluid accelerates, the presence of the particles retards the fluid's acceleration and therefore results in negative perturbation velocity, and vice versa.

Given that the perturbation velocity is induced by non-zero c, we can derive from the velocity decomposition of (12.3.1) that

$$(\vartheta-1)c\frac{D\overline{\boldsymbol{u}}}{Dt}+\frac{D\boldsymbol{u}'}{Dt}=-\boldsymbol{\nabla}p'+\frac{1}{Re}\nabla^2\boldsymbol{u}'. \tag{12.3.2}$$

It can be confirmed that (12.3.2) becomes identical to the total equation in (12.3.1) if $c=0$. Recalling that the aim is to investigate the initial particle distribution $c(t=0)$, denoted c_0, that effectively perturbs the 'undisturbed' vortex towards optimal transient growth, we assume zero perturbations at $t=0$. This makes (12.3.2) reduce to

$$\frac{\partial\boldsymbol{u}'}{\partial t}\Big|_{t=0}=-(\vartheta-1)c_0\frac{D\overline{\boldsymbol{u}}}{Dt}\Big|_{t=0}. \tag{12.3.3}$$

Suppose that we aim to initiate a specific velocity perturbation $\breve{\boldsymbol{u}}'$. If we find c_0 such that right-hand side of (12.3.3) coincides with (a positive constant multiple of) $\breve{\boldsymbol{u}}'$, then we may expect $\boldsymbol{u}'$ after a brief advancement in time to exhibit the perturbation in the form of $\breve{\boldsymbol{u}}'$. The existence of such c_0 is rare since (12.3.3) in fact comprises three component equations whereas c_0 is the only unknown. We inevitably concentrate on the most important one among those in order to circumvent this overdetermination issue. If we choose the azimuthal component, the problem is converted into finding c_0 such that

$$-(\vartheta - 1)c_0\left(\frac{D\overline{\boldsymbol{u}}}{Dt}\right)_\phi\Big|_{t=0} = C\breve{u}'_\phi, \tag{12.3.4}$$

where C is an arbitrary positive constant, standing for scaling c_0 later when solving (12.2.1) and (12.2.2) with various levels of particle volumetric loading. Arranging the terms with the fact that $(D\overline{\boldsymbol{u}}/Dt)_\phi|_{t=0} = -4re^{-r^2}/Re$ for the 'undisturbed' q-vortex profile $\overline{\boldsymbol{U}}$, the relation may be more simplified to $c_0 \propto \breve{u}'_\phi/(re^{-r^2})$.

The suggested c_0 involves two serious drawbacks, restricting its utility. Nonetheless, we affirm that it is still useful enough to initiate optimal transient growth. First, the radial and axial perturbation velocity components are excluded from consideration. This is justifiable due to the fact that the azimuthal component of velocity perturbation in transient growth is found to be commonly predominant at the beginning (see the left panels in figure 11.6). Second, more importantly, particle volume fraction cannot be negative. The fluid continuity might aid this issue; in a local sense, the deficiency (surplus) in speed in particle-laden fluid must be counterbalanced by the speed gain (lose) of circumferential particle-free fluid. Consequently, we set c_0 to zero when its estimate from (12.3.4) is negative.

For comparison's sake, we bring ourselves back to the optimal perturbation case considered in §11.4, where $(m, \kappa) = (1, 0.1)$ with $\tau = 50$. Figure 12.1 shows the initial particle volume fraction calculated via the suggested estimation, and the axial vorticity after a brief advancement in time ($t = 0.01$) as a result of the two-way interactions between the particles and the vortex with the initial particle volumetric loading level $c_{\max} = 10^{-6}$. Computing the perturbation velocity fields in two-way coupled vortex-particle simulations is essentially the same as in (11.4.3), except that what determines the perturbation intensity now is the particle volumetric loading level $c_{\max}$. Despite the drawbacks addressed above, the resulting perturbation satisfactorily resembles the desired perturbation input (see figure 11.7) towards optimal transient growth.

12.4 Particle-initiated transient growth

Now that the evolution of perturbations of a vortex is governed by (12.3.2), where the term $(\vartheta - 1)c(D\overline{\boldsymbol{u}}/Dt)$ serves as a non-zero external force, the overall perturbation dynamics are not only explained by the transient growth process but are also affected by the continual interaction between the particles and the vortex flow (n.b., simliar discussion can be found in Fontane *et al.*, 2008, p. 249). In what follows, we substantiate particle-initiated transient growth by confirming some clear indications of transient growth over short time intervals in the vortex-particle system with the initial particle distribution given in figure 12.1.

Temporal changes in perturbation energy are displayed in figure 12.2 with four different levels of particle volumetric loading: $c_{\max} = 10^{-4}$, 10^{-5}, 10^{-6}, and 10^{-7}. The case of $c_{\max} = 10^{-4}$ is considered to be the upper limit of having $(\vartheta - 1)c$ significantly less than order

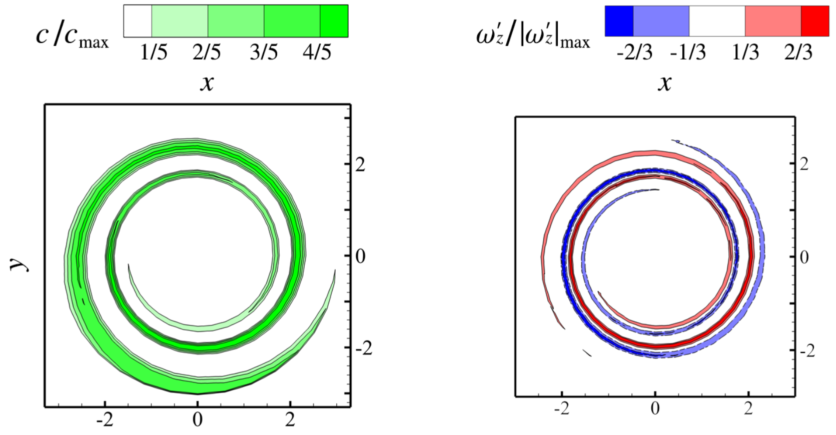

(a) $c(t = 0)$ (b) $\omega_z'(t = 0.01)$

Figure 12.1: Initiation of optimal transient growth via inertial particles: (*a*) (left) the initial particle volume fraction contour on the $z = 0$ plane, in the pursuit of initiating the perturbation studied in §11.4 (see figure 11.7), and (*b*) (right) the axial vorticity perturbation contour on the $z = 0$ plane after a brief advancement in time ($t = 0.01$) in the two-way coupled vortex-particle simulation solving (12.2.1) and (12.2.2) with the initial particle volumetric loading level of $c_{\max} = 10^{-6}$. In the right panel, the same contour style as figure 11.7 is used and $|\omega_z'(t = 0.01)|_{\max} = 5.80 \times 10^{-6}$.

unity (n.b., $\vartheta = 10^3$). All energy curves follow an almost identical trend, indicating that the same general dynamics take control of these cases. In the right panel of the figure, the data are normalised by the perturbation energy at $t = 10$ for each case (note that $E(0)$ is zero and the energy growth we have used, $E(t)/E(0)$, is undefined here) to compare energy amplification between these cases. Overall, the energy amplification in the end appears to be levelled at around 10^2 times $E(10)$ due to the long-time response of the vortex to the particles. Arguably, the amplification above this level should be attributed to the transient growth process, especially including the energy amplification 'hump' up to $t = 80$. Also, the peak of this hump at $t = 50$ coincides with the optimal transient growth period $\tau = 50$ that we intend to induce, which we believe strengthens our argument.

Another indication of the particle-initiated transient growth is observed in the evolution of the perturbation structure. In figure 12.3, the axial vorticity perturbation contours on the $z = 0$ plane at $t = 25$, $t = 50$ and $t = 100$ in the vortex-particle simulation with $c_{\max} = 10^{-4}$ are depicted. We compare these snapshots with those of the optimally perturbed non-linear vortex growth in figure 11.9(*c*). The continual vortex-particle interactions produce the structural discrepancy of the perturbation; this is clearly discernible at $t = 100$, where the strong spiraling arms are formed at the periphery as a result of the long-term drag momentum exchange. Nonetheless, in the light of the early-stage perturbation growth until $t = 50$, some crucial features representing the optimal transient growth process can be identified, such as the appearance of two weak spiraling arms at the periphery of the core at $t = 25$. Most importantly, at the time of the maximum energy growth ($t = 50$), the perturbation energy

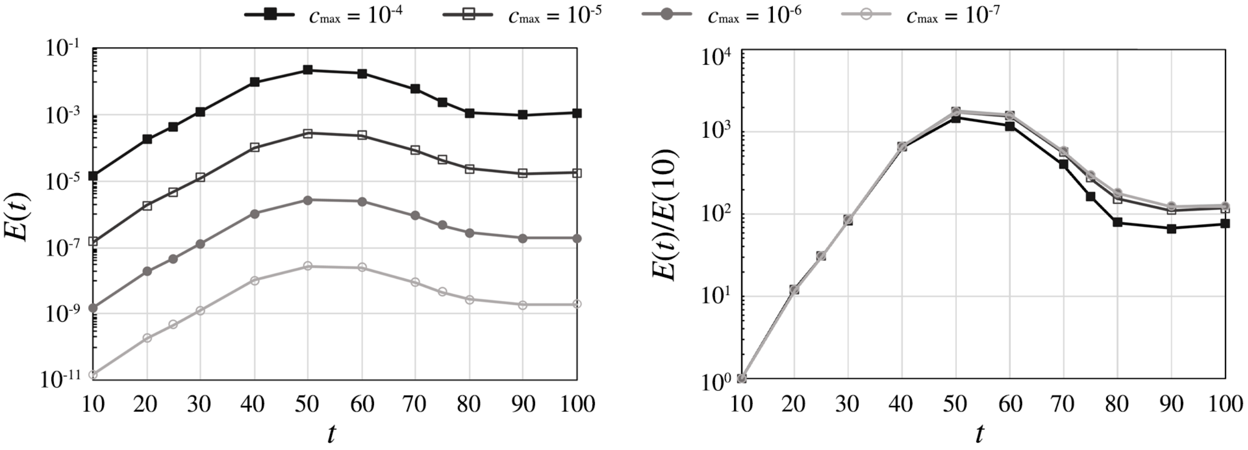

Figure 12.2: (Left) temporal perturbation energy changes in the vortex-particle motion (see figure 12.1 for the initial setup) with various particle volumetric loading levels: $c_{\max} = 10^{-4}$, 10^{-5}, 10^{-6} and 10^{-7} and (right) the same data but normalised by $E(10)$ to compare energy amplification. Note that $E(10)$ is arbitrarily chosen as $E(t)/E(0)$ is undefined in these cases because $E(0) = 0$.

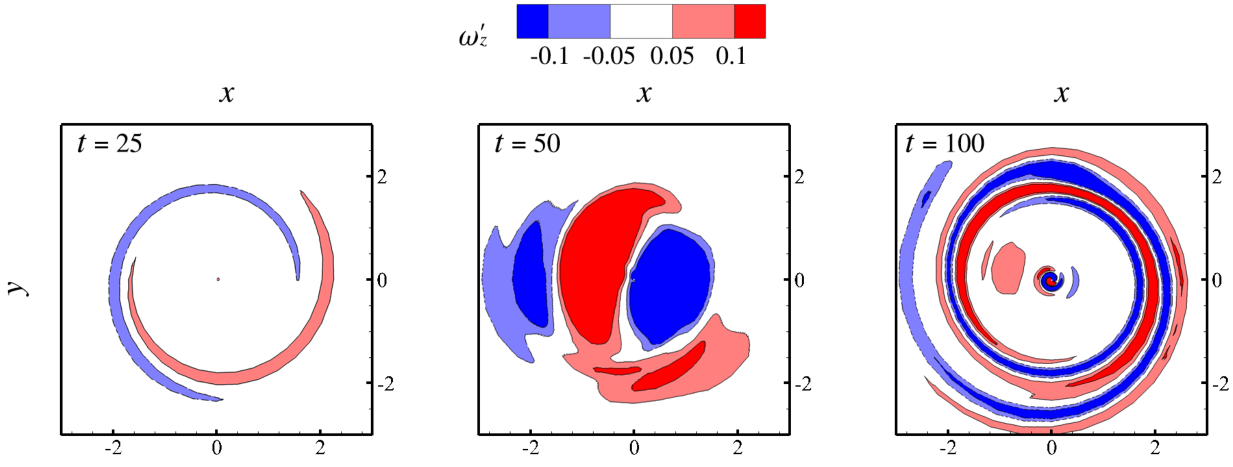

Figure 12.3: Axial vorticity perturbation contours of the vortex interacting with the peripherially located particles (refer to figure 12.1 for the illustration of the initial particle distribution) on the $z = 0$ plane at $t = 25$, $t = 50$ and $t = 100$. Here, depicted is the case of $c_{\max} = 10^{-4}$.

transfer from the periphery to the core—the iconic feature of the optimal transient growth process with respect to $m = 1$—is identifiable. We believe that this serves as the plausible evidence that nearly optimal transient growth takes place via vortex-particle interactions.

Lastly, we report the transient development of the particle distribution in association with the vortex transient growth. In figure 12.4, the vortex interacting with the particles

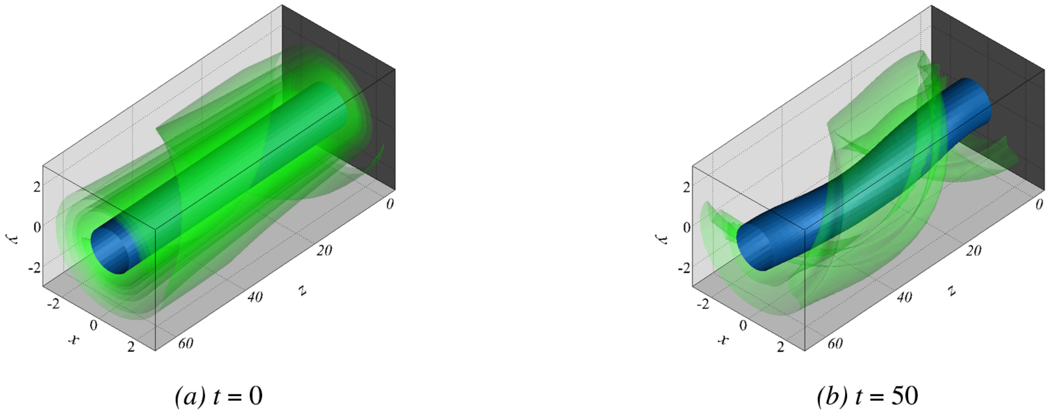

Figure 12.4: Three-dimensional illustration of the q-vortex interacting with the peripherally located particles (see figure 12.1) of the initial particle volumetric loading level of $c_{\max} = 10^{-4}$: (a) $t = 0$, and (b) $t = 50$. The vortex core is detected using the λ_2-isosurface where $\lambda_2 = -0.05$, as with figure 11.10. The green isosurface of $c = 2 \times 10^{-5}$ (20 % of $c_{\max}$) is drawn together to visualise the particle distribution at each time.

where $c_{\max} = 10^{-4}$ is visualised using the λ_2-isosurface for the vortex core and the isosurface of 20 % of $c_{\max}$ for the particles. While the vortex evolves into the most excited state ($t = 50$) from the unperturbed state ($t = 0$), the particles tend to be less dispersed, forming a coherent helical structure that encompasses the vortex core. However, the coherence remains evanescent and dissolves quickly after the maximum perturbation growth at $t = 50$. The physical implication of such a temporary increase in coherence, as well as whether it is not just the special case for $m = 1$, should be investigated further. For now, we note that the physical phenomenon relevant to the current exemplary case, vortex meandering, is known to have a particular tendency of increasing the 'orderliness' of the system (i.e., reduction of the number of dynamically active proper orthogonal decomposition (POD) modes), according to Bölle (2021); the coherence of the particles during the vortex's transient growth is likely to be correlated with this tendency.

Chapter 13

Concluding remarks II

In this part of study, we examined the transient dynamics of a wake vortex using a spectral method tailored to a radially unbounded domain, leading us to confirm that the essential contributor to optimal transient growth among continuous eigenmode families is the viscous critical-layer eigenmode family, rather than the potential eigenmode family. In addition, we explored inertial particles at the periphery of a vortex, motivated by ice crystals forming contrails in the real world, as a significant means of initiating optimal transient growth through drag momentum exchange that has often been neglected.

Using the spectral method for an unbounded domain, which we developed using the mapped Legendre functions as basis functions (see S. Lee & Marcus, 2023), we numerically analysed the transient growth process of the q-vortex slightly disturbed by a perturbation in the form of a sum of well-resolved eigenmodes. In a numerical sense, our method is not vulnerable to some critical issues that unfavorably affect the numerical sensitivity with regard to transient growth analysis, usually found in the conventional spectral method involving Chebyshev polynomials with domain truncation. These issues include the excessive spawning of unnecessary (non-regular or spurious) eigenmode families and the unclear distinction of the viscous critical-layer spectrum from the potential spectrum, due to the incomplete mimicking of the unbounded domain setup. Our method was found to prevent these problems in a proactive manner and, consequently, provide more tolerance for tuning numerical resolution using the map parameter L.

Following the typical transient growth formalism, we treated perturbations as a sum of eigenmodes. We then naturally investigated which family of eigenmodes contributes dominantly to optimal perturbations for achieving optimal transient growth. The important behaviour of short-term perturbation energy growth is known to be associated with continuously varying eigenmodes, grounded upon the non-normality of the linearised Navier-Stokes operator. Mao and Sherwin (2012) showed the predominance of continuous eigenmodes in optimal perturbations for the transient growth of a wake vortex, while not providing further categorisation of the continuous eigenmodes, especially for the viscous critical-layer eigenmode family. Through the exploration of the sub-eigenspaces, each respectively spanned by a distinct eigenmode family, it was corroborated that optimal transient growth is principally attributed to the viscous critical-layer eigenmodes. We believe that this finding provides a better alignment of the theoretical foundation of transient growth with the critical layer analysis, rather than the wave packet pseudomode analysis, in compliance with the argument relating inviscid continuous spectrum (CS) transients to vortex growth over short time intervals (Heaton, 2007b). Also, this helps us narrow down our focus when exploring the continuous spectra, as the viscous critical-layer spectrum solely accounts for continuous curves neighbouring the discrete spectrum, whereas the remaining continuous spectrum (potential spectrum) fills an extensive area in the left half of the complex eigenvalue plane.

The energy growth curves and the associated optimal perturbation structures acquired in the present analysis, concerning the axisymmetric ($m = 0$) and helical ($m = 1$) cases with axial wavenumbers κ of order unity or less, were found to be in agreement with previous literature. Overall, we revealed the generic responses during the optimal transient growth process: for $m = 0$, the transition of the azimuthal velocity to the other components in consistent ring streaks, and for $m = 1$, the transition of the swirling velocity layers outside the vortex core to the large transverse motion in the core. These processes are consistent with those unraveled by previous vortex transient growth studies such as Pradeep and Hussain (2006), Fontane *et al.* (2008), and Mao and Sherwin (2012). In the nonlinear simulations of the q-vortex initially with an $(m, \kappa) = (1, 0.1)$ optimal perturbation given the optimal growth period of $\tau = 50$, we were able to assert the prevalence of the dynamics of transient growth, particularly until the expected time of maximum energy growth ($t \leq \tau = 50$), concluding that these processes predicted by the linearised system are robust even in the original nonlinear system over meaningful time intervals.

Lastly, we discussed the initiation process of transient growth (i.e., generating perturbations from physical interactions, rather than naively assuming their presence at the beginning) and studied the validity of our discussion. Instead of ambient turbulence, which may provide a compelling path for initiation yet is difficult to model precisely due to its fundamental intricacy, we considered vortex-particle interactions inspired by ice crystals, or contrails, in association with aircraft wake vortices in practice. Despite the small size of individual particles, often leading to the assumption that their backward influence on the flow is negligible, their bulk inertial effect along with the large particle number density might make them not simply neglected. Enabling the two-way coupling between the particles and the vortex flow via drag momentum exchange, we ran the vortex-particle simulations with the particles initially distributed at the periphery of the vortex core, in order to initiate the optimal perturbation for $(m, \kappa) = (1, 0.1)$ studied ahead. We successfully spotted clear indications of optimal transient growth during the continual vortex-particle interactions, including the large energy amplification hump that peaks at $t = \tau = 50$ and the perturbation energy transfer process from the periphery into the core.

The present study underscores the significance of the optimal transient growth process of a single vortex over short time intervals, initially structured by the critical-layer eigenmodes. The initiation of transient growth via particle drag not only demonstrates the practicability of the transient growth process but also reaffirms the susceptibility of the vortex motion, even against physical interactions that have often been neglected either for simplicity or due to superficial insignificance. As Fontane *et al.* (2008) suggested in their vortex transient growth study with stochastic forcing, the transient growth process might be active regardless of the details or dynamics of the perturbations; particle drag could be one of those activators. Even though our motivation for considering particles was founded upon existing contrails, particles as a means of perturbing a vortex can be more useful if we attempt to actively control the wake vortex system to expedite its destabilisation, beyond understanding its nature, through, for example, deliberate injection of inertial particles.

Conclusion

Chapter 14

Summary and conclusions

In the first part of the research, a specialised numerical method was introduced for the linear stability analysis of wake vortices, with a particular focus on the q-vortex model, representing non-dimensional Lamb-Oseen or Batchelor vortices. Integral to this method were algebraically mapped associated Legendre functions, denoted as $P_{L_n}^{m}(r)$ (m is order and n is degree), chosen for their natural satisfaction of boundary conditions—analyticity at $r = 0$ and appropriate decay as r approaches infinity – essential for modeling vortex dynamics in a radially unbounded domain.

This numerical framework integrated a poloidal-toroidal decomposition technique aimed at reducing computational efforts while preserving the restrictions posed by the original governing equations, namely the incompressible Navier-Stokes or Euler equations. The framework effectively converted the original vortex stability problem into a standard matrix eigenvalue problem, significantly reducing the problem's complexity by reducing the number of state variables from four (i.e., the primitive variables of three velocity components and pressure scalar) to two and decreasing the matrices used for eigenvalue computations from two to one. This not only enhanced computational efficiency but also eliminated the need for additional adjustments related to boundary conditions in radially unbounded domains, thereby minimising unexpected numerical inaccuracies.

An important aspect of this method was its flexibility in the allocation of collocation points around the vortex core, not only with the number of spectral basis elements and collocation points, M and N, but also with the adjustable map parameter L. Half of the points were allocated within $0 \leq r < L$, ensuring precise capture of vortex dynamics near the core, while the remaining points extended into the outer domain of $r \geq L$. This versatile collocation point distribution enabled efficient and reliable computation of eigenmodes and eigenvalue spectra across various base flow conditions and perturbation parameters.

Numerical computations conducted using this method focused on analyzing eigenmodes and corresponding eigenvalue spectra for strong swirling q-vortices. Through the computations, eigenmodes were categorised into distinct families based on their physical characteristics and the arrangement of their corresponding spectrum on the complex eigenvalue plane. The discrete family, characterised by regular solutions to the linearised governing equations, exhibited localised oscillations ("wiggles") around the vortex core and demonstrated rapid decay in the radial direction. Importantly, these eigenmodes showed robust convergence under viscosity adjustments, reinforcing their physical relevance in vortex stability analysis.

In contrast, the inviscid critical-layer family emerged from inherent mathematical singularities in the linear vortex dynamics under consideration. This presented challenges related to under-resolution (in a discretised sense) due to the singular nature of their eigenmodes. Adjusting parameters, particularly the map parameter L, proved effective in rectifying numerical errors associated with under-resolved eigenmodes, thereby aligning computed spectra with expected analytical outcomes. Interestingly, the corrected inviscid critical-layer spectrum, through its numerically discretised proxy, revealed a characteristic eigenvalue pairing phenomenon. The phenonenon was believed to come from slight degeneracy breaking due to numerical approximations of originally singular degenerate eigen-solution pairs.

The potential family, previously identified as the viscous remnants of the inviscid critical-layer spectrum under the influence of viscosity, occupied a distinct segment in the complex eigenvalue plane characterised by scattered numerical values lacking clear convergence patterns. These eigenmodes, typified by localised rapid oscillations in the form of "wave packets," indicated a viscous regularisation effect on critical layers, albeit with uncertainties regarding their scaling behaviour with Re. Despite these concerns, their well-resolved spatial eigenmode structures hinted their physical relevance.

Highlighting a new discovery, attention was drawn to the viscous critical-layer family following the viscosity-induced alteration in the whole inviscid spectra. Although continuous together with the potential family, their spectrum was distinctive at the right end of the potential spectrum, exhibiting clear traces of two continuous curves. Despite structural similarities to the potential family around viscously regularised critical layers, their identification as the true remnants was rooted in their non-trivial behaviour outside the critical layer resembling inviscid counterparts and adherence to the $Re^{-1/3}$ scaling law for numerically resolving this family, leading to our affirmation regarding the "true" viscous remnants of the invsicid critical-layer spectrum.

In light of the findings demonstrated through the linear stability analysis part, the mapped Legendre spectral collocation method served as a conclusively useful tool for elucidating the linear stability of wake vortices for both the inviscid analysis and viscous analysis. Its methodological advantages encompassed computational efficiency, flexibility through optimal collocation point distributions, and fidelity in resolving singular or nearly singular eigenmodes across diverse vortex setups of varying perturbation wavenumbers. The systematic classification of eigenmodes made in the research not only deepened understanding of linear vortex dynamics but also informed further needs of studying the importance of critical layers and pertinent eigenmodes.

In the second part of the research, the developed spectral method, employing mapped Legendre functions as basis functions, was utilised for the computational analysis of the transient growth process of q-vortices under non-modal perturbations expressed as a sum of physical or spatially well-resolved eigenmodes. Unlike conventionally preferred spectral methods involving Chebyshev polynomials with domain truncation, this approach avoided problems such as the excessive spawning of contextually unnecessary (i.e., non-regular or spurious) eigenmode families and the less clear distinction between the viscous critical-layer spectrum and the potential spectrum. These issues are supposedly related to the incomplete implementation of unboundedness in a finitely truncated radial domain; in contrast, the presented method could avoid these issues as it was intended for unbounded vortical flows and allowed more tolerance in tuning numerical resolution using the map parameter L.

Following the typical transient growth formalism, perturbations were treated as a sum of eigenmodes to investigate which eigenmode family dominantly contributed to optimal perturbations that achieve the greatest transient growth. Short-term perturbation energy growth was found to be associated with continuously varying eigenmodes, grounded in the non-normality of the linearised Navier-Stokes operator, which leads to the continuous spectra. Previous studies demonstrated the predominance of continuous eigenmodes in the constitution of optimal perturbations for transient growth. However, with the further categorisation of these continuous eigenmodes, especially concerning the viscous critical-layer eigenmode family, it was corroborated that optimal transient growth was principally attributed to the viscous critical-layer eigenmodes, while the potential eigenmodes' contribution was not significant.

Energy growth curves and associated optimal perturbation structures calculated from the analysis of axisymmetric ($m = 0$) and helical ($m = 1$) cases with axial wavenumbers κ of order unity or less were found to be consistent with previous literature. Generic responses during the optimal transient growth process were revealed: for $m = 0$, the transition of azimuthal velocity to other components in consistent ring structures, and for $m = 1$, the transition of swirling velocity layers outside the vortex core to large transverse motion within the core. These findings were in agreement with earlier results concerning vortex transient growth studies.

Nonlinear simulations of the q-vortex with an initial optimal perturbation for $(m,\ \kappa) = (1,\ 0.1)$, given the optimal growth period $\tau = 50$, exhibited the prevalence of transient growth dynamics, particularly up to the expected time of maximum energy growth ($t \leq \tau = 50$). This was believed to support the robustness of these processes predicted by the linearised framework within the original nonlinear system over meaningful time intervals.

Next, the initiation process of transient growth was discussed, emphasising physical interactions rather than assuming the presence of perturbations at the beginning. Based on inspiration from contrails near real wake vortices, momentum effects of surrounding ice crystals in association with wake vortex motion were considered. Despite the tiny size of individual particles, their bulk inertial effect and high particle number density (compared to the fluid) might render their influence on the flow non-negligible. Vortex-particle simulations, with particles initially distributed at the vortex core periphery, demonstrated clear indications of optimal transient growth during continual and nonlinear vortex-particle interactions, including a significant energy amplification hump peaking at the expected optimal growth time and the transfer of perturbation energy from the periphery into the core.

In conclusion, the transient growth analysis part reviewed and affirmed the significance of optimal transient growth of a single vortex over short time intervals, anew highlighting that critical-layer eigenmodes are the crucial ingredients to structure optimal perturbations. The initiation of transient growth via particle drag not only demonstrated the practicability of the transient growth process but also reaffirmed the susceptibility of vortex motion to physical interactions often neglected due to perceived insignificance. Considering particles as a means of perturbing a vortex might be useful for actively controlling wake vortex systems to expedite destabilisation through deliberate injection of inertial particles.

Bibliography

Antkowiak, A., & Brancher, P. (2004). Transient energy growth for the Lamb–Oseen vortex. *Physics of Fluids*, *16*(1), L1–L4. https://doi.org/10.1063/1.1626123

Apkarian, P., & Noll, D. (2020). Optimizing the Kreiss constant. *SIAM Journal on Control and Optimization*, *58*(6), 3342–3362. https://doi.org/10.1137/19m1296215

Ash, R. L., & Khorrami, M. R. (1995). Vortex stability. In S. I. Green (Ed.), *Fluid vortices* (1995 ed., pp. 317–372). Dordrecht, NL: Springer Dordrecht. ISBN: 9780792333760.

Auton, T. R., Hunt, J. C. R., & Prud'Homme, M. (1988). The force exerted on a body in inviscid unsteady non-uniform rotational flow. *Journal of Fluid Mechanics*, *197*, 241–257. https://doi.org/10.1017/s0022112088003246

Batchelor, G. K. (1964). Axial flow in trailing line vortices. *Journal of Fluid Mechanics*, *20*(4), 645–658. https://doi.org/10.1017/s0022112064001446

Batchelor, G. K., & Gill, A. E. (1962). Analysis of the stability of axisymmetric jets. *Journal of Fluid Mechanics*, *14*(04), 529. https://doi.org/10.1017/s0022112062001421

Bölle, T. (2021). *Treatise on the meandering of vortices* [Thèse de doctorat]. Institut Polytechnique de Paris. Theses.fr: 2021IPPAX038.

Bölle, T., Brion, V., Couliou, M., & Molton, P. (2023). Experiment on jet-vortex interaction for variable mutual spacing. *Physics of Fluids*, *35*, 015117. https://doi.org/10.1063/5.0127634

Bölle, T., Brion, V., Robinet, J.-C., Sipp, D., & Jacquin, L. (2021). On the linear receptivity of trailing vortices. *Journal of Fluid Mechanics*, *908*, A8. https://doi.org/10.1017/jfm.2020.898

Bouaoudia, S., & Marcus, P. S. (1991). Fast and accurate spectral treatment of coordinate singularities. *Journal of Computational Physics*, *96*(1), 217–223. https://doi.org/10.1016/0021-9991(91)90272-m

Boyd, J. P. (2001). *Chebyshev and Fourier Spectral Methods* (2nd ed. rev.). Mineola, NY: Dover Publications. ISBN: 9780486411835.

Breitsamter, C. (2011). Wake vortex characteristics of transport aircraft. *Progress in Aerospace Sciences*, *47*(2), 89–134. https://doi.org/10.1016/j.paerosci.2010.09.002

Bristol, R. L., Ortega, J. M., Marcus, P. S., & Savaş, Ö. (2004). On cooperative instabilities of parallel vortex pairs. *Journal of Fluid Mechanics*, *517*, 331–358. https://doi.org/10.1017/s0022112004001016

Canuto, C., Hussaini, M. Y., Quarteroni, A., & Zang, T. A. (1988). *Spectral Methods in Fluid Dynamics* (1st ed.). Heidelberg, DE: Springer Berlin Heidelberg. ISBN: 9783540522058.

Case, K. M. (1960). Stability of inviscid plane Couette flow. *Physics of Fluids*, *3*(2), 143–148. https://doi.org/10.1063/1.1706010

Chandrasekhar, S. (1981). *Hydrodynamic and Hydromagnetic Stability* (Dover ed.). Mineola, NY: Dover Publications. ISBN: 9780486640716.

Crow, S. C. (1970). Stability theory for a pair of trailing vortices. *AIAA Journal*, *8*(12), 2172–2179. https://doi.org/10.2514/3.6083

Crow, S. C., & Bate, E. R. (1976). Lifespan of trailing vortices in a turbulent atmosphere. *Journal of Aircraft*, *13*(7), 476–482. https://doi.org/10.2514/3.44537

Devenport, W. J., Zsoldos, J. S., & Vogel, C. M. (1997). The structure and development of a counter-rotating wing-tip vortex pair. *Journal of Fluid Mechanics*, *332*(1997), 71–104. https://doi.org/10.1017/s0022112096003795

Drazin, P. G., & Reid, W. H. (2004). *Hydrodynamic Stability* (2nd ed.). Cambridge, UK: Cambridge University Press. ISBN: 9780521525411.

Dunham, R. E. (1977). Unsuccessful concepts for aircraft wake vortex minimization. In *Wake vortex minimization* (pp. 221–249). National Aeronautics and Space Administration. https://ntrs.nasa.gov/citations/19780004080 [Accessed: 24 June 2024].

Edstrand, A. M., Davis, T. B., Schmid, P. J., Taira, K., & Cattafesta, L. N. (2016). On the mechanism of trailing vortex wandering. *Journal of Fluid Mechanics*, *801*(2016), R1. https://doi.org/10.1017/jfm.2016.440

Eisen, H., Heinrichs, W., & Witsch, K. (1991). Spectral collocation methods and polar coordinate singularities. *Journal of Computational Physics*, *96*(2), 241–257. https://doi.org/10.1016/0021-9991(91)90235-d

El-Ramly, Z., & Rainbird, W. J. (1977). Effect of Simulated Jet Engines on the Flowfield behind a Swept-Back Wing. *Journal of Aircraft*, *14*(4), 343–349. https://doi.org/10.2514/3.58783

Fabre, D., & Jacquin, L. (2004). Viscous instabilities in trailing vortices at large swirl numbers. *Journal of Fluid Mechanics*, *500*, 239–262. https://doi.org/10.1017/s0022112003007353

Fabre, D., Sipp, D., & Jacquin, L. (2006). Kelvin waves and the singular modes of the Lamb-Oseen vortex. *Journal of Fluid Mechanics*, *551*, 235–274. https://doi.org/10.1017/s0022112005008463

Ferry, J., & Balachandar, S. (2001). A fast Eulerian method for disperse two-phase flow. *International Journal of Multiphase Flow*, *27*(7), 1199–1226. https://doi.org/10.1016/s0301-9322(00)00069-0

Feys, J., & Maslowe, S. A. (2014). Linear stability of the Moore-Saffman model for a trailing wingtip vortex. *Physics of Fluids*, *26*(2), 024108. https://doi.org/10.1063/1.4865838

Feys, J., & Maslowe, S. A. (2016). Elliptical instability of the Moore-Saffman model for a trailing wingtip vortex. *Journal of Fluid Mechanics*, *803*, 556–590. https://doi.org/10.1017/jfm.2016.512

Fontane, J., Brancher, P., & Fabre, D. (2008). Stochastic forcing of the Lamb-Oseen vortex. *Journal of Fluid Mechanics*, *613*, 233–254. https://doi.org/10.1017/s002211200800308x

Gallay, T., & Smets, D. (2020). Spectral stability of inviscid columnar vortices. *Analysis & PDE*, *13*(6), 1777–1832. https://doi.org/10.2140/apde.2020.13.1777

Gerz, T., Holzäpfel, F., & Darracq, D. (2002). Commercial aircraft wake vortices. *Progress in Aerospace Sciences*, *38*(3), 181–208. https://doi.org/10.1016/S0376-0421(02)00004-0

Gottlieb, D., & Orszag, S. A. (1977). *Numerical Analysis of Spectral Methods: Theory and Applications* (1st ed.). Philadelphia, PA: Society for Industrial and Applied Mathematics. ISBN: 9780898710236.

Grosch, C. E., & Salwen, H. (1978). The continuous spectrum of the Orr-Sommerfeld equation. Part 1. The spectrum and the eigenfunctions. *Journal of Fluid Mechanics*, *87*(1), 33–54. https://doi.org/10.1017/s0022112078002918

Hagan, J., & Priede, J. (2013). Capacitance matrix technique for avoiding spurious eigenmodes in the solution of hydrodynamic stability problems by Chebyshev collocation method. *Journal of Computational Physics*, *238*, 210–216. https://doi.org/10.1016/j.jcp.2012.12.012

Hallock, J. N., & Holzäpfel, F. (2018). A review of recent wake vortex research for increasing airport capacity. *Progress in Aerospace Sciences*, *98*, 27–36. https://doi.org/10.1016/j.paerosci.2018.03.003

Han, J., Lin, Y.-L., Schowalter, D. G., Arya, S. P., & Proctor, F. H. (2000). Within Homogeneous Turbulence: Crow Instability Large Eddy Simulation of Aircraft Wake Vortices. *AIAA Journal*, *38*(2), 292–300. https://doi.org/10.2514/2.956

Heaton, C. J. (2007a). Centre modes in inviscid swirling flows and their application to the stability of the Batchelor vortex. *Journal of Fluid Mechanics*, *576*, 325–348. https://doi.org/10.1017/s0022112006004447

Heaton, C. J. (2007b). Optimal growth of the Batchelor vortex viscous modes. *Journal of Fluid Mechanics*, *592*, 495–505. https://doi.org/10.1017/s0022112007008634

Heaton, C. J., & Peake, N. (2007). Transient growth in vortices with axial flow. *Journal of Fluid Mechanics*, *587*, 271–301. https://doi.org/10.1017/s0022112007007434

Howard, L. N., & Gupta, A. S. (1962). On the hydrodynamic and hydromagnetic stability of swirling flows. *Journal of Fluid Mechanics*, *14*(3), 463–476. https://doi.org/10.1017/s0022112062001366

Ivers, D. J. (1989). On generalised toroidal-poloidal solutions of vector field equations. *The Journal of the Australian Mathematical Society. Series B. Applied Mathematics*, *30*(4), 436–449. https://doi.org/10.1017/s0334270000006378

Jacobs, R. G., & Durbin, P. A. (1998). Shear sheltering and the continuous spectrum of the Orr-Sommerfeld equation. *Physics of Fluids*, *10*(8), 2006–2011. https://doi.org/10.1063/1.869716

Jeong, J., & Hussain, F. (1995). On the identification of a vortex. *Journal of Fluid Mechanics*, *285*, 69–94. https://doi.org/10.1017/s0022112095000462

Jones, C. A. (2008). Dynamo theory. In P. Cardin & L. G. Cugliandolo (Eds.), *Les Houches* (1st ed., pp. 45–135, Vol. 88). Amsterdam, NL: Elsevier. ISBN: 9780080548128.

Kärcher, B. (2018). Formation and radiative forcing of contrail cirrus. *Nature Communications*, *9*, 1824. https://doi.org/10.1038/s41467-018-04068-0

Kärcher, B., Peter, T., Biermann, U. M., & Schumann, U. (1996). The Initial Composition of Jet Condensation Trails. *Journal of the Atmospheric Sciences*, *53*(21), 3066–3083. https://doi.org/10.1175/1520-0469(1996)053⟨3066:ticojc⟩2.0.co;2

Kelvin, L. (1880). Vibrations of a columnar vortex. *The London, Edinburgh, and Dublin Philosophical Magazine and Journal of Science*, *10*(61), 155–168. https://doi.org/10.1080/14786448008626912

Khorrami, M. R. (1991). On the viscous modes of instability of a trailing line vortex. *Journal of Fluid Mechanics*, *225*, 197–212. https://doi.org/10.1017/s0022112091002021

Khorrami, M. R., Malik, M. R., & Ash, R. L. (1989). Application of spectral collocation techniques to the stability of swirling flows. *Journal of Computational Physics*, *81*(1), 206–229. https://doi.org/10.1016/0021-9991(89)90071-5

Lacaze, L., Ryan, K., & Le Dizès, S. (2007). Elliptic instability in a strained Batchelor vortex. *Journal of Fluid Mechanics*, *577*, 341–361. https://doi.org/10.1017/s0022112007004879

Le Dizès, S. (2004). Viscous critical-layer analysis of vortex normal modes. *Studies in Applied Mathematics*, *112*(4), 315–332. https://doi.org/10.1111/j.0022-2526.2004.01514.x

Le Dizès, S., & Lacaze, L. (2005). An asymptotic description of vortex kelvin modes. *Journal of Fluid Mechanics*, *542*, 69–96. https://doi.org/10.1017/s0022112005005185

Lee, D. S., Fahey, D. W., Skowron, A., Allen, M. R., Burkhardt, U., . . . Wilcox, L. J. (2021). The contribution of global aviation to anthropogenic climate forcing for 2000 to 2018. *Atmospheric Environment*, *244*, 117834. https://doi.org/10.1016/j.atmosenv.2020.117834

Lee, S., & Marcus, P. S. (2024). Transient growth of a wake vortex and its initiation via inertial particles. arXiv: 2402.07469.

Lee, S., & Marcus, P. S. (2023). Linear stability analysis of wake vortices by a spectral method using mapped Legendre functions. *Journal of Fluid Mechanics*, *967*, A2. https://doi.org/10.1017/jfm.2023.455

Leibovich, S. (1978). Structure of vortex breakdown. *Annual Review of Fluid Mechanics*, *10*(1), 221–246. https://doi.org/10.1146/annurev.fl.10.010178.001253

Leibovich, S., & Stewartson, K. (1983). A sufficient condition for the instability of columnar vortices. *Journal of Fluid Mechanics*, *126*, 335–356. https://doi.org/10.1017/s0022112083000191

Lessen, M., Singh, P. J., & Paillet, F. (1974). The stability of a trailing line vortex. Part 1. Inviscid theory. *Journal of Fluid Mechanics*, *63*(4), 753–763. https://doi.org/10.1017/s0022112074002175

Leweke, T., Le Dizès, S., & Williamson, C. H. K. (2016). Dynamics and instabilities of vortex pairs. *Annual Review of Fluid Mechanics*, *48*(1), 507–541. https://doi.org/10.1146/annurev-fluid-122414-034558

Lewellen, D. C., & Lewellen, W. S. (2001). The Effects of Aircraft Wake Dynamics on Contrail Development. *Journal of the Atmospheric Sciences*, *58*(4), 390–406. https://doi.org/10.1175/1520-0469(2001)058⟨0390:teoawd⟩2.0.co;2

Lin, C.-C. (1955). *The Theory of Hydrodynamic Stability* (1st ed.). Cambridge, UK: Cambridge University Press.

Lin, C.-C. (1961). Some mathematical problems in the theory of the stability of parallel flows. *Journal of Fluid Mechanics*, *10*(3), 430–438. https://doi.org/10.1017/s0022112061001025

Lopez, J. M., Marques, F., & Shen, J. (2002). An efficient spectral-projection method for the Navier–Stokes equations in cylindrical geometries. *Journal of Computational Physics*, *176*(2), 384–401. https://doi.org/10.1006/jcph.2002.6993

Mahalov, A. (1993). The instability of rotating fluid columns subjected to a weak external Coriolis force. *Physics of Fluids A: Fluid Dynamics*, *5*(4), 891–900. https://doi.org/10.1063/1.858635

Mao, X., & Sherwin, S. (2011). Continuous spectra of the Batchelor vortex. *Journal of Fluid Mechanics*, *681*, 1–23. https://doi.org/10.1017/jfm.2011.194

Mao, X., & Sherwin, S. J. (2012). Transient growth associated with continuous spectra of the Batchelor vortex. *Journal of Fluid Mechanics*, *697*, 35–59. https://doi.org/10.1017/jfm.2012.33

Marcus, P. S., Pei, S., Jiang, C.-H., Barranco, J. A., Hassanzadeh, P., & Lecoanet, D. (2015). Zombie vortex instability: I. A purely hydrodynamic instability to resurrect the dead zones of protoplanetary disks. *The Astrophysical Journal*, *808*(1), 87. https://doi.org/10.1088/0004-637x/808/1/87

Maslowe, S. A. (1986). Critical layers in shear flows. *Annual Review of Fluid Mechanics*, *1*, 405–432. https://doi.org/10.1146/annurev.fluid.18.1.405

Matalanis, C. G. (2007). *Wake vortex alleviation using rapidly actuated segmented gurney flaps* [PhD Dissertation]. Stanford University. ProQuest Dissertations & Theses: 304826793.

Matsunaga, R. (2024). *Air Traffic by The Numbers* (8th ed.) [Electronic]. Federal Aviation Administration. https://www.faa.gov/air_traffic/by_the_numbers [Accessed: 22 June 2024].

Matsushima, T., & Marcus, P. S. (1995). A spectral method for polar coordinates. *Journal of Computational Physics*, *120*(2), 365–374. https://doi.org/10.1006/jcph.1995.1171

Matsushima, T., & Marcus, P. S. (1997). A spectral method for unbounded domains. *Journal of Computational Physics*, *137*(2), 321–345. https://doi.org/10.1006/jcph.1997.5804

Maxey, M. R., & Riley, J. J. (1983). Equation of motion for a small rigid sphere in a nonuniform flow. *Physics of Fluids*, *26*(4), 883–889. https://doi.org/10.1063/1.864230

Maxworthy, T., Hopfinger, E. J., & Redekopp, L. G. (1985). Wave motions on vortex cores. *Journal of Fluid Mechanics*, *151*, 141. https://doi.org/10.1017/s0022112085000908

Mayer, E. W., & Powell, K. G. (1992). Viscous and inviscid instabilities of a trailing vortex. *Journal of Fluid Mechanics*, *245*, 91–114. https://doi.org/10.1017/s0022112092000363

McFadden, G. B., Murray, B. T., & Boisvert, R. F. (1990). Elimination of spurious eigenvalues in the Chebyshev tau spectral method. *Journal of Computational Physics*, *91*(1), 228–239. https://doi.org/10.1016/0021-9991(90)90012-p

Moore, D. W., & Saffman, P. G. (1973). Axial flow in laminar trailing vortices. *Proceedings of the Royal Society of London. A. Mathematical and Physical Sciences*, *333*(1595), 491–508. https://doi.org/10.1098/rspa.1973.0075

Moore, D. W., & Saffman, P. G. (1975). The instability of a straight vortex filament in a strain field. *Proceedings of the Royal Society of London. A. Mathematical and Physical Sciences*, *346*(1646), 413–425. https://doi.org/10.1098/rspa.1975.0183

Muthiah, G., & Samanta, A. (2018). Transient energy growth of a swirling jet with vortex breakdown. *Journal of Fluid Mechanics*, *856*, 288–322. https://doi.org/10.1017/jfm.2018.712

Naiman, A. D., Lele, S. K., & Jacobson, M. Z. (2011). Large eddy simulations of contrail development: Sensitivity to initial and ambient conditions over first twenty minutes. *Journal of Geophysical Research: Atmospheres*, *116*, D21208. https://doi.org/10.1029/2011jd015806

Navrose, Johnson, H. G., Brion, V., Jacquin, L., & Robinet, J. C. (2018). Optimal perturbation for two-dimensional vortex systems: route to non-axisymmetric state. *Journal of Fluid Mechanics*, *855*, 922–952. https://doi.org/10.1017/jfm.2018.689

Orszag, S. A. (1974). Fourier series on spheres. *Monthly Weather Review*, *102*(1), 56–75. https://doi.org/10.1175/1520-0493(1974)102⟨0056:fsos⟩2.0.co;2

Paoli, R., & Garnier, F. (2005). Interaction of exhaust jets and aircraft wake vortices: small-scale dynamics and potential microphysical-chemical transformations. *Comptes Rendus Physique*, *6*(4-5), 525–547. https://doi.org/10.1016/j.crhy.2005.05.003

Paoli, R., Hélie, J., & Poinsot, T. (2004). Contrail formation in aircraft wakes. *Journal of Fluid Mechanics*, *502*, 361–373. https://doi.org/10.1017/s0022112003007808

Pradeep, D. S., & Hussain, F. (2006). Transient growth of perturbations in a vortex column. *Journal of Fluid Mechanics*, *550*, 251. https://doi.org/10.1017/s0022112005008207

Press, W. H., Teukolsky, S. A., Vetterling, W. T., & Flannery, B. P. (2007). *Numerical Recipes: The Art of Scientific Computing* (3rd ed.). Cambridge, UK: Cambridge University Press. ISBN: 9780521880688.

Proctor, F. H., Hamilton, D. W., & Han, J. (2000). Wake vortex transport and decay in ground effect: Vortex linking with the ground. In *38th aerospace sciences meeting and exhibit* (AIAA-2000–0757). American Institute of Aeronautics and Astronautics. https://doi.org/10.2514/6.2000-757

Qiu, S., Cheng, Z., Xu, H., Xiang, Y., & Liu, H. (2021). On the characteristics and mechanism of perturbation modes with asymptotic growth in trailing vortices. *Journal of Fluid Mechanics*, *918*, A41. https://doi.org/10.1017/jfm.2021.353

Roy, A., & Subramanian, G. (2014). Linearized oscillations of a vortex column: The singular eigenfunctions. *Journal of Fluid Mechanics*, *741*, 404–460. https://doi.org/10.1017/jfm.2013.666

Saffman, P. G. (1993). *Vortex Dynamics* (1st ed.). New York, NY: Cambridge University Press. ISBN: 9780521477390.

Sakurai, J. J., & Napolitano, J. (2021). *Modern Quantum Mechanics* (3rd ed.). Cambridge, UK: Cambridge University Press. ISBN: 9781108473224.

Sarpkaya, T. (1983). Trailing vortices in homogeneous and density-stratified media. *Journal of Fluid Mechanics*, *136*, 85–109. https://doi.org/10.1017/s0022112083002074

Schmid, P. J., & Henningson, D. S. (1994). Optimal energy density growth in Hagen–Poiseuille flow. *Journal of Fluid Mechanics*, *277*, 197–225. https://doi.org/10.1017/s0022112094002739

Schmid, P. J., & Henningson, D. S. (2001). *Stability and Transition in Shear Flows* (2001 ed., Vol. 142). New York, NY: Springer New York. ISBN: 9781461265641.

Schumann, U. (2005). Formation, properties and climatic effects of contrails. *Comptes Rendus Physique*, *6*, 549–565. https://doi.org/10.1016/j.crhy.2005.05.002

Shirgaonkar, A. A. (2007). *Large eddy simulation of early stage aircraft contrails* [PhD Dissertation]. Stanford University. ProQuest Dissertations & Theses: 304826603.

Shuai, S., Jeswin Dhas, D., Roy, A., & Kasbaoui, M. H. (2022). Instability of a dusty vortex. *Journal of Fluid Mechanics*, *948*, A56. https://doi.org/10.1017/jfm.2022.687

Shuai, S., & Kasbaoui, M. H. (2022). Accelerated decay of a Lamb–Oseen vortex tube laden with inertial particles in Eulerian–Lagrangian simulations. *Journal of Fluid Mechanics*, *936*, A8. https://doi.org/10.1017/jfm.2022.50

Smith, D. M. (2003). Using multiple-precision arithmetic. *Computing in Science & Engineering*, *5*(4), 88–93. https://doi.org/10.1109/mcise.2003.1208649

Spalart, P. R. (1998). Airplane trailing vortices. *Annual Review of Fluid Mechanics*, *30*(1), 107–138. https://doi.org/10.1146/annurev.fluid.30.1.107

Stewartson, K., & Brown, S. N. (1985). Near-neutral centre-modes as inviscid perturbations to a trailing line vortex. *Journal of Fluid Mechanics*, *156*, 387. https://doi.org/10.1017/s0022112085002154

Trefethen, L. N., & Embree, M. (2005). *Spectra and Pseudospectra: The Behavior of Nonnormal Matrices and Operators* (1st ed.). Princeton, NJ: Princeton University Press. ISBN: 9780691119465.

Tsai, C. Y., & Widnall, S. E. (1976). The stability of short waves on a straight vortex filament in a weak externally imposed strain field. *Journal of Fluid Mechanics*, *73*(4), 721–733. https://doi.org/10.1017/s0022112076001584

Vasil, G. M., Burns, K. J., Lecoanet, D., Olver, S., Brown, B. P., & Oishi, J. S. (2016). Tensor calculus in polar coordinates using Jacobi polynomials. *Journal of Computational Physics*, *325*, 53–73. https://doi.org/10.1016/j.jcp.2016.08.013

Vasil, G. M., Lecoanet, D., Burns, K. J., Oishi, J. S., & Brown, B. P. (2019). Tensor calculus in spherical coordinates using Jacobi polynomials. Part-I: Mathematical analysis and derivations. *Journal of Computational Physics: X*, *3*, 100013. https://doi.org/10.1016/j.jcpx.2019.100013

Voigt, C., Schumann, U., Jessberger, P., Jurkat, T., Petzold, A., . . . Fahey, D. W. (2011). Extinction and optical depth of contrails. *Geophysical Research Letters*, *38*(11), L11806. https://doi.org/10.1029/2011gl047189

Wang, J., Lee, S., & Marcus, P. S. (2024). Triadic resonance in columnar vortices. arXiv: 2402.05287.

Widnall, S. E. (1975). The structure and dynamics of vortex filaments. *Annual Review of Fluid Mechanics*, *7*(1), 141–165. https://doi.org/10.1146/annurev.fl.07.010175.001041

Zebib, A. (1987). Removal of spurious modes encountered in solving stability problems by spectral methods. *Journal of Computational Physics*, *70*(2), 521–525. https://doi.org/10.1016/0021-9991(87)90193-8

Appendix A: Differential operators

For a $r-$dependent scalar function $f(r)$, the gradient and the Laplacian are

$$\boldsymbol{\nabla}_{m\kappa} f \equiv \frac{df}{dr}\hat{\boldsymbol{e}}_r + \frac{\mathrm{i}m}{r} f \hat{\boldsymbol{e}}_\phi + \mathrm{i}\kappa f \hat{\boldsymbol{e}}_z, \tag{A1}$$

$$\nabla^2_{m\kappa} f \equiv \frac{1}{r}\frac{d}{dr}\left(r\frac{df}{dr}\right) - \frac{m^2}{r^2} f - \kappa^2 f. \tag{A2}$$

For a $r-$dependent vector field $\boldsymbol{F}(r) \equiv F_r(r)\hat{\boldsymbol{e}}_r + F_\phi(r)\hat{\boldsymbol{e}}_\phi + F_z(r)\hat{\boldsymbol{e}}_z$, the divergence, the curl and the vector Laplacian are

$$\boldsymbol{\nabla}_{m\kappa} \cdot \boldsymbol{F} \equiv \frac{dF_r}{dr} + \frac{F_r}{r} + \frac{\mathrm{i}m}{r} F_\phi + \mathrm{i}\kappa F_z, \tag{A3}$$

$$\begin{aligned} \boldsymbol{\nabla}_{m\kappa} \times \boldsymbol{F} \equiv & \left(\frac{\mathrm{i}m}{r} F_z - \mathrm{i}\kappa F_\phi\right)\hat{\boldsymbol{e}}_r + \left(\mathrm{i}\kappa F_r - \frac{dF_z}{dr}\right)\hat{\boldsymbol{e}}_\phi \\ & + \left(\frac{dF_\phi}{dr} + \frac{F_\phi}{r} - \frac{\mathrm{i}m}{r} F_r\right)\hat{\boldsymbol{e}}_z, \end{aligned} \tag{A4}$$

$$\begin{aligned} \nabla^2_{m\kappa} \boldsymbol{F} \equiv & \left(\nabla^2_{m\kappa} F_r - \frac{F_r}{r^2} - \frac{2\mathrm{i}m}{r^2} F_\phi\right)\hat{\boldsymbol{e}}_r + \left(\nabla^2_{m\kappa} F_\phi - \frac{F_\phi}{r^2} + \frac{2\mathrm{i}m}{r^2} F_r\right)\hat{\boldsymbol{e}}_\phi \\ & + \left(\nabla^2_{m\kappa} F_z\right)\hat{\boldsymbol{e}}_z. \end{aligned} \tag{A5}$$

Appendix B: Analyticity at the origin

In literature studying swirling flows in a radially unbounded domain with respect to the perturbation with azimuthal wavenumber m and axial wavenumber κ, i.e., $\boldsymbol{u}' = \tilde{\boldsymbol{u}}(r; m, \kappa)e^{\mathrm{i}(m\phi+\kappa z)+\sigma t}$ and $p' = \tilde{p}(r; m, \kappa)e^{\mathrm{i}(m\phi+\kappa z)+\sigma t}$, the boundary conditions in terms of primitive variables $(\tilde{u}_r, \tilde{u}_\phi, \tilde{u}_z, \tilde{p})$ have been typically expressed as

$$\begin{cases} \tilde{u}_r = \tilde{u}_\phi = 0, \ \ \tilde{u}_z \text{ and } \tilde{p} \text{ finite} & \text{for } m = 0 \\ \dfrac{d\tilde{u}_r}{dr} = \tilde{u}_r + m\tilde{u}_\phi = \tilde{u}_z = \tilde{p} = 0 & \text{for } |m| = 1 \\ \tilde{u}_r = \tilde{u}_\phi = \tilde{u}_z = \tilde{p} = 0 & \text{for } |m| > 1 \end{cases} \text{at } r = 0, \ \ \tilde{\boldsymbol{u}}, \ \tilde{p} \to 0 \ \text{ as } r \to \infty. \tag{B1}$$

These conditions were first suggested by Batchelor and Gill (1962) and the detailed derivation can be found in Ash and Khorrami (1995, pp. 339-342). Our numerical method naturally complies with the far-field condition as all spectral basis elements, $P^m_{L_n}(r)$, are designed to vanish at radial infinity. Additionally, our method's handling of velocity functions at the origin not only meets the centerline condition given above, but also leads to a more accurate function behaviour. This is verified in the following.

The derivation of the centerline condition begins with

$$\lim_{r\to 0} \frac{\partial \boldsymbol{u}'}{\partial \phi} = 0, \tag{B2}$$

to remove the coordinate singularity at $r = 0$, ensuring smoothness. As the pressure term is implicit in our formulation, it is excluded from consideration. The term-by-term expression of (B2) is

$$-\mathrm{i}m\tilde{u}_r + \tilde{u}_\phi = -\mathrm{i}\tilde{u}_r + m\tilde{u}_\phi = m\tilde{u}_z = 0 \quad \text{as } r \to 0. \tag{B3}$$

With the additional condition $d\tilde{u}_r/dr = d\tilde{u}_\phi/dr = 0$ for $|m| = 1$ (Mayer & Powell, 1992; Ash & Khorrami, 1995; Bölle *et al.*, 2021), which is independent of (B2) and from the regularity of the governing equations around $r = 0$, the final formula is obtained.

In our numerical approach, the toroidal $\tilde{\psi}(r; m, \kappa)$ and poloidal $\tilde{\chi}(r; m, \kappa)$ streamfunctions are chosen as the state variables of the eigenvalue problem and are expanded by the mapped Legendre functions, both of which behave $O\left(r^{|m|+2s}\right)$ for a non-negative integer s as $r \to 0$ (see Matsushima & Marcus, 1995, 1997). That is, in our numerical method, it is guaranteed that as $r \to 0$, these streamfunctions are expressed in power series as

$$\tilde{\psi}(r; m, \kappa) = a_0 r^{|m|} + a_1 r^{|m|+2} + \cdots, \quad \tilde{\chi}(r; m, \kappa) = b_0 r^{|m|} + b_1 r^{|m|+2} + \cdots, \tag{B4}$$

where all coefficients are finite constants, as in (4.2.11). From the decomposition, it is known that

$$\tilde{u}_r = \frac{\mathrm{i}m}{r}\tilde{\psi} + \mathrm{i}\kappa\frac{\partial\tilde{\chi}}{\partial r}, \quad \tilde{u}_\phi = -\frac{\partial\tilde{\psi}}{\partial r} - \frac{\kappa m}{r}\tilde{\chi}, \quad \tilde{u}_z = -\frac{1}{r}\frac{\partial}{\partial r}\Big(r\frac{\partial\tilde{\psi}}{\partial r}\Big) + \frac{m^2}{r^2}\tilde{\psi}. \tag{B5}$$

Therefore, our method ensures that as $r \to 0$,

$$\begin{aligned} \tilde{u}_r &= \big(\mathrm{i}a_0 m + \mathrm{i}b_0\kappa|m|\big)r^{|m|-1} + \big(\mathrm{i}a_1 m + \mathrm{i}b_1\kappa(|m|+2)\big)r^{|m|+1} + \cdots, \\ \tilde{u}_\phi &= \big(-a_0|m| - b_0\kappa m\big)r^{|m|-1} + \big(-a_1(|m|+2) - b_1\kappa m\big)r^{|m|+1} + \cdots, \\ \tilde{u}_z &= a_1\big(-(|m|+2)^2 + m^2\big)r^{|m|} + \cdots. \end{aligned} \tag{B6}$$

These power series satisfy (B3) for all m, which can be shown by simply putting (B6) into (B3). This verifies that the mapped Legendre expansion of the poloidal and toroidal streamfunctions, as in (B4), meets the centerline condition of the primitive velocity components, as in (B1).

The power series expansion in (B6) ultimately stands for the analyticity at the origin, providing more accurate constraints for smoothness on the coordinate singularity. The typical centerline condition is not a sufficient condition for smoothness due to the lack of derivative constraints, as seen in (B2), even requiring an additional condition for some cases. Correctly removing coordinate singularities in spectral methods has been known to be crucial for the accuracy of the spectral representation, which can be done by choosing appropriate basis spectral elements with regards to what coordinate singularity is in consideration (Orszag, 1974; Bouaoudia & Marcus, 1991; Matsushima & Marcus, 1995, 1997). General Chebyshev or Legendre spectral methods that do not implicitly take into account such analyticity issue, thus necessitating an explicit boundary condition to mimic the analyticity, might not be the suitable choice for systems with coordinate singularities to achieve fast spectral convergence (see Gottlieb & Orszag, 1977; Boyd, 2001). We note two papers (Vasil *et al.*, 2016, 2019) that looked at a variety of spectral methods dealing with coordinate singularities and gave evidence to support the use of the mapped associated Legendre functions for the cylindrical coordinate singularity.

Appendix C: Numerical integration for energy calculation

Consider the following definite integral I of an arbitrary scalar f in terms of r:

$$I(f) \equiv \int_0^\infty f^*(r) f(r) r dr. \tag{C1}$$

It is assumed that f decays sufficiently fast as $r \to \infty$ so that $I(f)$ is well-defined. Using change of variables from $r \in [0, \infty)$ to a new variable $\zeta \in [-1, 1)$ via

$$\zeta \equiv \frac{r^2 - L^2}{r^2 + L^2}, \tag{C2}$$

where $L > 0$ is the map parameter, we alter (C1) into a new form as follows:

$$I(f) = \int_{-1}^{1} f^* \left(L\sqrt{\frac{1+\zeta}{1-\zeta}} \right) f \left(L\sqrt{\frac{1+\zeta}{1-\zeta}} \right) \frac{L^2}{(1-\zeta)^2} d\zeta. \tag{C3}$$

Applying the Gauss-Legendre quadrature rule as used by S. Lee and Marcus (2023, p. 13), we obtain the numerical form of (C3) as

$$I(f) \simeq \sum_{j=1}^{N} f^*(r_j) \frac{L^2 \varpi_j}{(1-\zeta_j)^2} f(r_j), \tag{C4}$$

where ζ_j and ϖ_j are the jth abscissa and the jth weight of the Gauss-Legendre quadrature rule for degree N ($j = 1,\ 2, \cdots,\ N$), and $r_j \equiv L\sqrt{(1+\zeta_j)/(1-\zeta_j)}$ is the jth radial collocation point. Note that (C4) can be expressed as $\boldsymbol{f}^* \mathbf{M}^\ddagger \boldsymbol{f}$ if we define $\boldsymbol{f}$ as the discretised version of f in physical space, i.e., $\boldsymbol{f} \equiv (f(r_1),\ \cdots,\ f(r_N))$ and $\mathbf{M}^\ddagger$ as

$$\mathbf{M}^\ddagger \equiv \mathrm{diag} \left(\frac{L^2 \varpi_1}{(1-\zeta_1)^2},\ \cdots,\ \frac{L^2 \varpi_N}{(1-\zeta_N)^2} \right). \tag{C5}$$

Finally, the energy in (10.1.7), which is equal to $I(\tilde{\boldsymbol{u}}_r)+I(\tilde{\boldsymbol{u}}_\phi)+I(\tilde{\boldsymbol{u}}_z)$, can be numerically calculated as follows:

$$E(\tilde{\boldsymbol{u}}) = \underbrace{\left(\begin{array}{c:c:c} \tilde{\boldsymbol{v}}_r^* & \tilde{\boldsymbol{v}}_\phi^* & \tilde{\boldsymbol{v}}_z^* \end{array}\right)}_{\tilde{\boldsymbol{v}}^*} \underbrace{\left(\begin{array}{c:c:c} \mathbf{M}^\ddagger & \mathbf{0} & \mathbf{0} \\ \hdashline \mathbf{0} & \mathbf{M}^\ddagger & \mathbf{0} \\ \hdashline \mathbf{0} & \mathbf{0} & \mathbf{M}^\ddagger \end{array}\right)}_{\mathbf{M}} \underbrace{\left(\begin{array}{c} \tilde{\boldsymbol{v}}_r \\ \hdashline \tilde{\boldsymbol{v}}_\phi \\ \hdashline \tilde{\boldsymbol{v}}_z \end{array}\right)}_{\tilde{\boldsymbol{v}}} . \tag{C6}$$

This constitutes the formation of $\mathbf{M}$ representing the matrix calculation for energy in (10.1.8).

Appendix D: Numerical setup for non-linear simulations

To discretise the radially unbounded domain considered in this study, especially in three dimensions for non-linear simulations, we employ a pseudo-spectral method based on the mapped Legendre spectral collocation method. The method assumes an arbitrary scalar field (or a component of an arbitrary vector field) that decays fast and harmonically in r, say, f, to be expanded as follows:

$$f(r, \phi, z, t) = \sum_{n=|m|}^{\infty} \sum_{m=-\infty}^{\infty} \sum_{k=-\infty}^{\infty} f_{nmk}(t) P_{L_n}^{m}(r) e^{im\phi} e^{ik\frac{2\pi}{Z}z}, \tag{D1}$$

where Z is the computational domain length in the z direction, corresponding to the longest axial wavelength under consideration. The expansion assumes periodicity with a period of Z in z and ensures analyticity at $r = 0$ and harmonic decay at radial infinity, thanks to the mapped Legendre basis functions $P_{L_n}^{m}(r)$. In this study, we chose $Z = 20\pi$, standing for the smallest axial wavenumber of 0.1 to be considered. On the other hand, L, the map parameter, defines the high-resolution region during pseudo-spectral calculations to be $0 \leq r < L$ (see S. Lee & Marcus, 2023, p. 13), and we chose $L = 4$ to secure resolution for the vortex motion of the core and the near periphery.

Although special logarithmic terms may be required to account for the $O(1/r)$ decay at large r (see Matsushima & Marcus, 1997, p. 331), we omit them here for simplicity in description. It is noted that the method was initially introduced by Matsushima and Marcus (1997) with several validation examples involving the vorticity equations, where one may look for additional details. Also, a more in-depth discussion of the implementation of the method in vortex stability research can be found in S. Lee and Marcus (2023).

The set of the coefficients f_{nmk} now represents f in a discrete manner. As practical computations demand the set to be finite, we chose $n \leq 400$, $|m| \leq 16$, and $|k| \leq 16$. The reason the radial elements make use of an extra degree (i.e., large n) compared to the others is to cope with the viscous critical layers of radially fine structures at high Re. Otherwise, for the purpose of our computations, a high degree for the other elements (i.e., large m and k) is not necessary, as our focus is principally on small wavenumbers.

In pure vortex simulations (without particles), we consider the toroidal and poloidal streamfunctions ψ and χ as the state variables to be discretised in space (by applying the toroidal-poloidal decomposition, $\mathbb{P}$, to the momentum equation) and then integrate them in time to solve the vortex motion. With particles, the particle volume fraction c is additionally considered, coupling the vortex and particle motions. When it comes to time integration, the fractional step method is employed, utilising the Adams-Bashforth method for non-linear terms (e.g., advection) and the Crank-Nicholson method for linear terms (e.g., dissipation) with Richardson extrapolation for the first time step (see Matsushima & Marcus, 1997, p. 343). Throughout preliminary simulations with the q-vortex ($q = 4$) perturbed with a small-amplitude eigenmode with a known frequency and decay rate, the time step was set to 10^{-3} as it yielded a tolerable error during the time integration between $t = 0$ and $t = 100$.